Toward a biofidelic and repeatable physical head-brain model for application in blunt impact

by

Yizhao Li

A thesis submitted in partial fulfillment of the requirements for the degree of

Doctor of Philosophy

Department of Mechanical Engineering
University of Alberta

Abstract

Headforms as a type of physical human head models are widely used in head injury research and for the design and assessment of safety gear. The mechanisms of head injury caused by blunt impact (a common loading scenario) are associated with global head kinematics and intracranial mechanics such as intracranial pressure (ICP). However, conventional headforms are limited to replicating only head kinematics. Although a few headforms have intracranial components to measure ICP including cerebrospinal fluid ICP (CSFP) and intraparenchymal ICP (IPP), such as the Blast Injury Protection Evaluation Device (BIPED) developed for blast scenarios, they lack the validation of biofidelity or cannot be used repeatedly in blunt impact. For modeling human mechanical responses, a headform should be biofidelic to provide realistic responses and repeatable to offer consistent measurements for the same loading conditions. This thesis aimed to characterize the impact responses and refine the design of the BIPED to contribute to the development of a biofidelic and repeatable headform capable of replicating both global head kinematics and ICP in blunt impact. Three studies were performed to achieve this aim.

First, drop impact experiments were conducted to characterize the BIPED kinematic biofidelity and the repeatability of the BIPED linear acceleration and IPP. Results showed that the linear acceleration and IPP measures were repeatable with coefficients of variation (COVs) generally being less than 10%. While the BIPED acceleration peaks had no statistically significant difference with cadaveric data, the acceleration pulse durations were approximately 50% longer. CORrelation and Analysis (CORA) ratings that quantify the closeness between time histories of the headform and cadaver measurements ranged from 0.50 to 0.61 for the

BIPED, compared to the range of 0.51–0.77 for the commonly used Hybrid III headform. The performed work quantitatively characterized the BIPED kinematic biofidelity and response repeatability, and the findings can inform the further improvement of the BIPED stiffness toward a biofidelic headform.

The first study could not fully characterize the ICP biofidelity and the response repeatability. Therefore, the second study conducted pendulum impact experiments to further characterize the BIPED ICP biofidelity and the repeatability of BIPED kinematics and ICP. Sensors were added to the BIPED for measuring linear and angular kinematics along three axes and CSFPs at three locations, in addition to the IPP measurements. The head kinematics, CSFP, and IPP demonstrated acceptable repeatability with COVs generally being less than 10%. The BIPED front CSFP peaks and back negative peaks were within the range of the scaled cadaveric data, while side CSFP peaks were 30.9–92.1% greater than the cadaveric data. CORA ratings for the front CSFP (0.68–0.72) aligned with the reported rating (0.7) for good biofidelity. This study indicates that the BIPED could replicate human front CSFP in the frontal blunt impact, but further refinement of the intracranial components is required to improve the biofidelity of ICP at other locations.

Based on the findings from the first two studies, one of the main limitations of the BIPED was its longer acceleration pulse durations compared to cadaveric data. Thus, the third study evaluated the refinement of the surrogate scalp material and thickness to improve the BIPED biofidelity. Drop impact tests were conducted with the BIPED skull and brain assembly attached to scalp pads of varied materials and thicknesses. While the selected materials exhibited a relatively minor effect on the linear acceleration and coup IPP, the scalp thickness showed a major effect. An optimal choice of scalp thickness and material was identified that

could increase the acceleration CORA ratings by approximately 30% to approach the threshold of 0.7 for good biofidelity.

In summary, the present thesis characterized the impact responses of the BIPED and improved its acceleration biofidelity to approach good biofidelity. This work is a significant step toward a validated comprehensive headform that can be a valuable tool to extend the depth of head injury research and advance the assessment methods of safety gear.

Preface

The thesis is an original work performed by Yizhao Li. The thesis was motivated by the collaborative work between Dr. Christopher Dennison and Simon Ouellet from Defense Research and Development Canada (DRDC) that aimed to refine the design of the BIPED for studying the mechanisms of head injuries caused by blast waves and blunt impacts on the battlefield. Considering that blunt impacts are also a common cause of head injuries in civilian life, I conducted this thesis work, focusing on extending the use of the BIPED to blunt impacts.

Dr. Christopher R. Dennison contributed to the conceptualization, experimental resources, supervision of the research, and review of the manuscripts. Dr. Albert H. Vette provided advice on the concepts, methodologies, and result interpretation, as well as assisted with manuscript revisions. Dr. Donald Raboud provided advice on the concepts and manuscript revisions. Simon Ouellet provided the BIPED components and advice on the concepts and manuscript revisions. Lab colleagues Ashton Martin, Kevin Adanty, and Paris Vakiel assisted with data collection and manuscript revisions. I was responsible for study conceptualization, design of experiments, setup of the data acquisition system (i.e., sensor installation, wiring, and LabVIEW coding), data collection, data curation, and manuscript writing. As detailed below, the content from some chapters of this thesis has been published as independent scientific articles.

The work presented in Chapters 3, 4, and 5 has been published in the Journal of Biomechanical Engineering, Annals of Biomedical Engineering, and Journal of the Mechanical Behavior of Biomedical Materials as original research articles, respectively.

(1) **Yizhao Li**, Simon Ouellet, Albert H. Vette, Donald Raboud, Ashton Martin, and Christopher R. Dennison. "Evaluation of the Kinematic Biofidelity and Inter-Test Repeatability of Global Accelerations and Brain Parenchyma Pressure for a Head–Brain Physical Model." Journal of Biomechanical Engineering. 2021 Sep 1; 143(9).

(2) **Yizhao Li**, Kevin Adanty, Paris Vakiel, Simon Ouellet, Albert H. Vette, Donald Raboud, and Christopher R. Dennison. " Evaluation of the Intracranial Pressure Biofidelity and Repeatability for a Head-brain Physical model in frontal impacts." Annals of Biomedical Engineering, 2023 Apr 24:1-8.

(3) **Yizhao Li**, Paris Vakiel, Kevin Adanty, Simon Ouellet, Albert H. Vette, Donald Raboud, and Christopher R. Dennison. " Influence of Surrogate Scalp Material and Thickness on Head Impact Responses: Toward a Biofidelic Head-Brain Physical Model." Journal of the Mechanical Behavior of Biomedical Materials. 2023 Apr 13:105859.

Part of the work presented in Chapter 5 was also submitted to a conference as a short communication article shown below.

Yizhao Li, Kevin Adanty, Paris Vakiel, Simon Ouellet, Albert H. Vette, Donald Raboud, Christopher R. Dennison. "The Effect of Surrogate Scalp Thickness on The Impact Response of a Physical Head-Brain Model." IRCOBI (2022). Porto, Portugal. 66-67.

Acknowledgments

I would like to first express my gratitude to my earlier supervisor (now the supervisory committee member) Dr. Christopher Dennison for his guidance and support. Without his continuous support of the research and advice on every aspect, I could not find the way to the success of this study. I would also like to thank my current supervisor, Dr. Albert Vette, for his unconditional support and advice, and rigorous help with my writing throughout my project. I am grateful for his patience, care, and always being there to help. I would like to thank the supervisory committee member Dr. Donald Raboud, for his great advice and insight to improve my research, as well as for help with reviewing the papers and thesis. I would like to thank Simon Ouellet for providing the resource regarding the BIPED and the advice on the research.

I am thankful to my colleagues who provided support, collaboration, and inspiration. My labmates not only aided with my experiments but also enriched my life in Canada. The time with them is a beautiful memory that I will always carry with gratitude.

I would like to acknowledge funding support from the Canada Research Chairs Program, the Natural Sciences and Engineering Research Council (Canada) Discovery and Alliance Grants, and the Canada Foundation for Innovation, as well as financial support from the China Scholarship Council.

Lastly, I would like to extend thanks to my family and friends who helped me pass through tough times. I'm particularly grateful to my supportive parents for helping with taking care of my baby to allow me more time on my thesis. I cannot find enough words to thank Yuejian Chen for his help, support, and encouragement. With his accompany and love, my life in Edmonton was extremely colorful and memorable.

Table of Contents

List of Tables

List of Figures

List of Acronyms

BIPED	Blast Injury Protection Evaluation Device
CSF	cerebrospinal fluid
CSFP	CSF intracranial pressure
COV	coefficient of variation
CORA	CORrelation and analysis
ICP	intracranial pressure
IPP	intraparenchymal intracranial pressure
MLR	multiple linear regression
NOCSAE	National Operating Committee on Standards for Athletic Equipment
TBI	traumatic brain injury

Chapter 1 Introduction

Chapter 1 provides an overview of this thesis research. This chapter contains three sections: Section 1.1 briefly introduces the research background and motivation, while Section 1.2 and Section 1.3 provide the objectives and outline of this thesis, respectively.

1.1 Background and Motivation

Head injuries commonly occur in civilian life and on the battlefield, and pose a high risk of resulting in functional disabilities and even fatalities [1]–[3]. Traumatic brain injuries (TBIs) are a major contributor to head injuries that can be severe and even cause fatalities or long-term disabilities. In Canada, head injury rates ranged from 77 out of 100,000 to 86 out of 100,000 between 2006 and 2018; 58.2% of those injuries were related to TBI [4]. TBI-related deaths accounted for 22.6% of all injury-related deaths in Canada [4]. From a telephone survey of Ontario residents between 2011 and 2013, more than 47% of the respondents with a TBI history reported having mild to severe long-term functional restrictions (e.g., difficulty with walking, standing, and learning) as well as mental health problems [5]. In the United States of America (USA), approximately 890 out of 100,000 of the population (i.e., 2.8 million individuals) suffered from TBI in 2013, resulting in TBI-related emergency room visits, hospitalizations, and deaths [6]. The number of TBI-related deaths (55,900) accounted for 2.2% of all deaths that year. The number of deaths in the USA increased to 61,100 in 2017 and to 64,400 in 2020 [7], [8]. The direct and indirect cost associated with TBI in the USA was over $60 billion based on an estimate in 2006 [9]. Globally, a study released in 2018 reported that an estimated 939 out of 100,000 of the worldwide population (i.e., 69 million individuals) suffered from TBI each year, and 8% of the injuries were categorized as severe TBI [10]. The

adverse impacts of TBI on the quality of life for affected individuals and on global economics highlight the need to reduce the frequency and severity of head injuries.

Falls and motor vehicle crashes are the major causes of TBI: 50.4% of TBI-related hospitalizations were caused by falls, and 21.5 % were caused by motor vehicle crashes in the USA in 2013 [6]. These causes generally involve blunt impacts to the head as opposed to penetrating impacts and blasts. Due to the burden of TBI caused by blunt impact, ongoing research goals include understanding the underlying mechanisms and improving prevention strategies for TBI.

Head surrogates, including human volunteers, post-mortem human subjects (PMHS), animal models, headforms, and numerical models, are the common tools for head injury research as well as the design of safety gear such as protective helmets [11]. Anthropometric Test Device (ATD) headforms or dummy heads are one of the most widely used head surrogates for laboratory studies and helmet certification tests. Compared to organic human heads and animal models, headforms have the advantages of being repeatable and easy to manipulate without posing ethical concerns [11]. Compared to numerical models that require either simulation of all the objects involved in the impact or laboratory reconstruction to obtain head kinematics as input, headforms can be directly used to test safety gear without the need for fully understanding their structure and material properties. Due to these advantages, headforms are valuable tools widely used to model human head responses in impact tests.

Commercially available headforms for blunt impact are limited to replicating only global head kinematics or skull mechanics. Commonly used headforms such as the Hybrid III and the National Operating Committee on Standards for Athletic Equipment (NOCSAE)

headform typically have no biofidelic intracranial components to simulate human intracranial responses [12]. These headforms are generally designed to mimic the external features, dimensions, mass, and moment of inertia of the human head, all of which determine the head kinematics but are insufficient to determine intracranial responses.

Both global kinematics and intracranial mechanics are important for understanding TBI; however, the lack of appropriate headforms contributes to the paucity of experimental studies on intracranial responses. Kinematics such as linear acceleration, angular acceleration, and angular velocity, as well as intracranial mechanics such as intracranial pressure (ICP) and brain strains, have been associated with TBI [13], [14]. However, none of the helmet assessment certifications adopt assessment criteria based on intracranial mechanics. This may be because methods for obtaining intracranial mechanical parameters are limited to using human cadavers and numerical models. Some researchers jointly use headforms and numerical models by inputting kinematics obtained from headforms into the numerical models to calculate intracranial mechanics [15]. This method is time-consuming and may be error-prone due to the uncertainty accumulated in the experiments and numerical simulations. To our knowledge, none of the commonly used headforms can provide intracranial measurements.

A few studies have attempted to develop comprehensive headforms that include internal structures to mimic intracranial mechanics; however, no such headforms have been widely used in current research and helmet certification tests [16]–[19]. The earliest physical head models for studying ICP simply filled a cranium with water [20]; thus, its biofidelity was poor. Among the limited headforms for measuring ICP, there are two headforms containing simulants for most of the intracranial components. One is the Instrumented Human Head Surrogate (IHHS-1) developed for evaluating modern ski helmets [19], [21]. The kinematic

biofidelity of this headform was not validated according to reported work [19], [21]. The other one is the Blast Injury Protection Evaluation Device (BIPED) headform designed by Defense Research and Development Canada [22]. This headform was developed for measuring ICP induced by shockwaves in blasts; thus, the physical properties related to impact responses such as the local stiffnesses and dynamic mechanical properties of the headform were not well considered during the design. Therefore, there is a lack of validated headforms capable of evaluating intracranial responses in addition to global head kinematics in blunt impact scenarios.

1.2 Thesis Objectives

The overall goal of this thesis was to characterize the impact responses and refine the design of the BIPED based on kinematics and ICP responses to contribute to the development of a biofidelic and repeatable headform for use in blunt impact. To achieve this goal, the research described in this thesis first characterized the biofidelity and repeatability of the BIPED kinematics and ICP responses for blunt impact, with the goal of identifying the feasibility and limitations of using the BIPED in blunt impact. This research then evaluated the design factors and identified a meaningful method of refinement to improve the BIPED biofidelity.

Specifically, the overall goal of this study was achieved through the following sub-objectives:

(1) To characterize the kinematic biofidelity and repeatability of the BIPED by comparing the BIPED with cadaver heads in blunt impact.

(2) To characterize the ICP biofidelity and repeatability of the BIPED by comparing the BIPED with cadaver heads in blunt impact.

(3) To evaluate the design factors that could improve the BIPED biofidelity or repeatability based on the findings from the first two sub-objectives.

To achieve the above sub-objectives, we conducted the following studies:

(1) Drop impact experiments were conducted to characterize the BIPED kinematic biofidelity and repeatability of the linear acceleration and intraparenchymal ICP (IPP) measurements.

(2) Translational impact experiments were conducted to characterize the BIPED ICP biofidelity and repeatability of the kinematics (including linear accelerations and angular rates along three axes) and ICP (including IPP and cerebrospinal fluid ICP (CSFP)).

(3) We evaluated the influence of surrogate scalp material and thickness on head impact responses and identified the method of scalp refinement to improve the BIPED biofidelity.

1.3 Thesis Outline

Chapter 2 introduces and summarizes the human head anatomy and the physical properties of head components as these provide the primary foundation for designing headforms. This chapter also briefly discusses the mechanisms and injury criteria of TBI, justifying the need for measuring both global head kinematics and intracranial mechanics. Headforms are a common tool used in helmet certification assessment. Therefore, current helmet assessment methods and metrics are briefly described, highlighting their limitations. Lastly, this chapter introduces the design requirements for headforms and describes widely used headforms as well as the BIPED used in this thesis work.

Chapters 3, 4, and 5 contain three studies published in or submitted to peer-reviewed journals. The first two studies presented in Chapters 3 and 4 rigorously characterized the BIPED biofidelity and repeatability, while the third study presented in Chapter 5 aimed at improving the BIPED based on observations from the first two studies.

Chapter 3 presents a study of characterizing the BIPED kinematic biofidelity and the repeatability of the acceleration and IPP measurements. Free-fall drop experiments were performed with the BIPED and the commonly used Hybrid III headform. The study captured the impact accelerations and IPP for impacts at the front, side, and vertex of the BIPED and Hybrid III headform. BIPED accelerations were compared to reported cadaveric data with respect to the peaks, durations, and time histories, and the repeatability of all the BIPED measurements was evaluated based on their coefficients of variation (COVs).

Chapter 4 presents a study of characterizing the BIPED ICP biofidelity and the repeatability of kinematics and ICP. Pendulum impact experiments were performed with the BIPED attached to the Hybrid III neck. A sensor package and three pressure sensors were added to the BIPED to measure the head linear accelerations, angular rates, and CSFP. The BIPED ICP was compared to reported cadaveric data, and the repeatability of all the kinematics and ICP measurements was evaluated based on the COVs of the measurements.

Chapter 5 presents a study aimed at evaluating the refinement of the surrogate scalp to improve the BIPED biofidelity, based on observations from the first two studies. Pads of various materials and thicknesses were molded to simulate the head scalp. In the experiments, the BIPED skull and brain assembly attached to each scalp pad was dropped onto an impact plate. The study evaluated the influence of the scalp pad modulus and thickness on the head

kinematics and IPP. Based on the results, an optimal choice of surrogate scalp was suggested that could effectively improve the acceleration biofidelity of the BIPED.

Chapter 6 summarizes the main results, discussion, and contributions of this thesis research, and provides recommendations for future studies.

Chapter 2 Literature Review

Chapter 2 first provides an introduction to the fundamentals of head structures, injury mechanisms, and injury criteria. Then, the chapter reviews the design requirements of headforms and discusses headforms that are currently used in biomechanical research and helmet certification tests. The presented knowledge is important for understanding why and how we conducted this research with the goal of contributing to the development of a comprehensive headform.

2.1 Head Anatomy and Physical Properties

Understanding the anatomy and physical properties of the human head is essential for designing human headforms because these fundamentals determine the head's mechanical responses. The head is a multi-layered structure with five components: scalp, skull, meninges, cerebrospinal fluid (CSF), and brain (Figure 2.1) [23]. The scalp is the outermost soft tissue that covers the cranial bone which is a major part of the skull. The meninges lie beneath the skull bone, serving as a protective layer of the innermost brain. This section discusses the anatomy and physical properties of the main components of the human head.

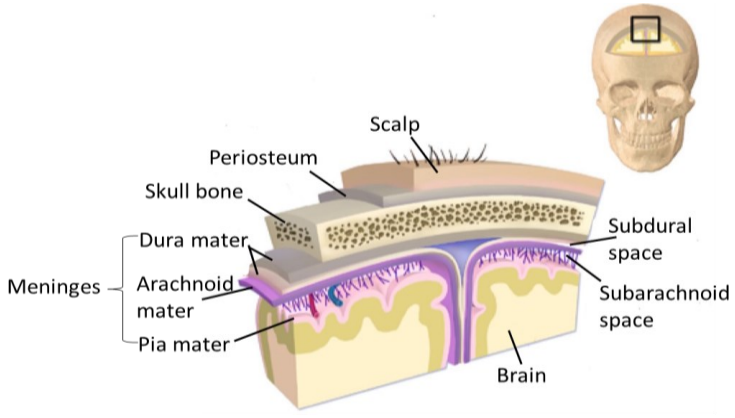

Figure 2.1. Head anatomy layers covering the brain (Image adapted from [24]).

2.1.1 Scalp

The scalp consists of five layers from outer to inner: the skin, connective tissue, epicranial aponeurosis, loose areolar tissue, and periosteum, as shown in Figure 2.2 [25]. The skin has numerous sebaceous glands and hair follicles through which hair grows. The connective tissue is a dense subcutaneous layer comprising fat and fibrous tissue. The epicranial aponeurosis is a tough layer of dense fibrous tissue. The first three layers function as a unit. The loose areolar tissue is located between this unit and the periosteum layer that connects to the cranial bone, allowing relative movement between the united upper layer and the skull [25].

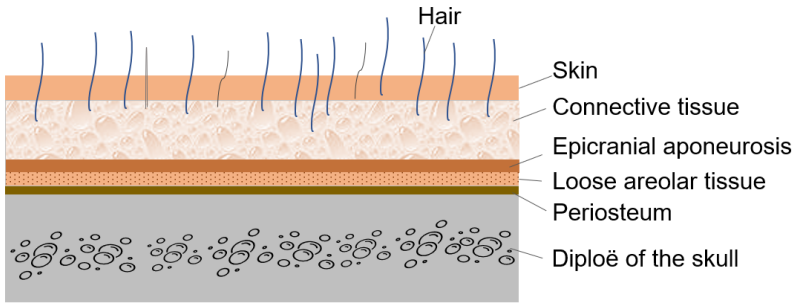

Figure 2.2. The layers of the scalp on top of the skull.

The thickness and material properties of the scalp vary with the age, sex, region of the head, and height and weight of the individuals. Reported scalp thickness ranges between 1 and 9 mm [26], [27]. The variation in the reported data may be due to the difference in the samples and measurement methods. Oltulu et al. measured 180 skin samples from 90 males and 9 females between the ages of 30 and 40 years [26]. The mean thickness for the scalp skin was 2.35 mm for females and 3.25 mm for males. The samples from this study included only the skin layer of the scalp [26]. Lupin et al. measured the thickness in the temporal region of the

human scalp. The total thickness of the scalp was 7±1.9 mm and 5.2±1.2 mm at two points in that region [27]. Using samples from cadavers with a mean age of 82 years, Chopra et al. measured a 0.97 to 1.48 mm thickness of the skin on the human head [28].

The scalp exhibits viscoelastic properties and is nearly incompressible with a density of approximately 1,000 kg/m^3 [29]. As shown in Table 2.1, the reported moduli of human skin on the entire body range from 1 to 87 MPa, depending on the loading rate, stretch ratio, and region of the skin samples [30]–[32]. Annaidh et al. used the digital image correlation method to evaluate the stretch ratio of skin samples from human back regions [33]. The skin samples were subjected to quasi-static tensions in different orientations [33]. They reported a modulus of 1.2 MPa for the initial stretch (infinitesimal strains) and an elastic modulus of 83.3 MPa for a higher strain of 1.35–1.48 [33]. The stretch orientations and locations of the skin sample were found to significantly affect the elastic modulus and ultimate tensile strength. The elastic modulus measured by Annaidh et al. is close to the maximum value (87.1 MPa) reported by Jacquemoud et al., but more than twice as large as those measured in studies by Melvin et al., Falland et al., and Trotta et al. [30], [31], [34]. This discrepancy may be due to the differences in the sample regions and strain rates as shown in Table 2.1. Considering studies on only the scalp, the reported elastic modulus was 15–38 MPa. In finite element models, the elastic modulus of 16.7 MPa has been used in several studies based on the data initially reported by Melvin et al. [35]–[37].

Table 2.1. Mechanical properties such as elastic modulus (EM), initial modulus (IM), and ultimate tensile strength (UTS) of human skin.

Reference	Sample region	Strain rate	Age	Parameters
Melvin et al. (1970) [30]	Scalp	0.2/s	–	EM=16.7 MPa
Jacquemoud et al. (2007) [38]	Forehead & arm	55/s	62–98	EM=19.5–87.1 MPa UTS=5.7–12.6 MPa
Annaidh et al. (2012) [33]	Back	0.012/s	81–97	EM=83.3±34.9 MPa IM=1.2±0.9 MPa UTS=21.6±8.4 MPa
Falland-Cheung et al. (2018) [31]	Temporal, front-parietal, occipital scalp	0.042/s	6–94	EM=19.1–25.2 MPa, UTS=2.8–3.4 MPa,
Trotta et al. (2019) [34]	Scalp	15–100/s	73–89	EM=15.4–37.7 MPa UTS=4.0–8.3 MPa

2.1.2 Skull

The skull also referred to as the cranium contains 22 bones including 14 facial bones and 8 cranial bones [25]. The cranial bones consist of a frontal bone, two temporal bones, two parietal bones, an occipital bone, a sphenoid bone, and an ethmoid bone, as shown in Figure 2.3. These bones are jointed together by cranial suture lines at their boundaries, forming a thin-walled shell to protect the brain. The occipital bone at the posterior part of the cranium has an oval hole called the foramen magnum, which is used for the passage of the spinal cord [25].

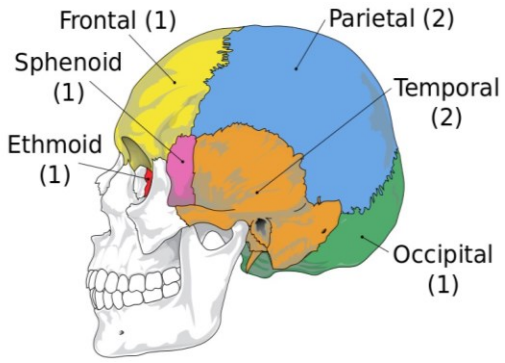

Figure 2.3. The eight bones of the human cranium (copyright released from Wikipedia).

The cranial bone is a sandwich structure consisting of the relatively stiff and compact outer and inner cortical bone with a middle layer of less stiff sponge bone (i.e., the diploë). The thickness of the cranial bone ranges between 4 and 10 mm and differs between regions of the skull and individuals [39]. The average thickness of the frontal bone is 6.5 mm [39]. The thickest part occurs at the occipitalis protuberance, while the thinnest part occurs in the temporal region [25]. The cranial bone is generally described as linear elastic with an elastic modulus of 1.2–10.5 GPa and a Poisson's ratio of 0.19–0.21 [40], [41]. Table 2.2 summarizes the basic material properties of the human cranial bones found in previous studies. McElhaney et al. used compression, tension, and torsion loadings to test different regions of the fresh and embalmed cranial bones [40]. They estimated the elastic moduli of these bones lying between 1.2 and 5.6 GPa, with a mean of 2.4 ±1.5 GPa [40]. This range of modulus is close to that (1.6–6 GPa) estimated from quasi-static three-point bending tests [42], [43]. The moduli measured from quasi-static tests are slightly lower than those (7.5–10.5 GPa) from dynamic three-point bending tests [41].

Table 2.2. Elastic modulus (EM), tensile strength (UTS), and Poisson's ratio (υ) of cranial bone found in literature studies.

Reference	Sample region	Loading type	Age	Parameters
McElhaney et al. (1970) [40]	Frontal, parietal, occipital	Compression Tension Torsion	56–73	EM=2.4–5.6 GPa, υ=0.19, EM=1.2–5.4 GPa, UTS=79 MPa EM=1.2 GPa
Verschueren1et al. (2006) [42]	Parietal	Flexure	20–30	EM=1.6–5.4 GPa
Motherway et al. (2009) [41]	Frontal, parietal	Flexure	81±11	EM=7.5–10.5 GPa
Rahmoun et al. (2014) [43]	Whole crania	Flexure	88	EM=2.0–6.0 GPa, υ=0.21

2.1.3 Meninges

As a layer that supports and protects the brain and spinal cord, the meninges lie beneath the cranial bone and consists of the dura, arachnoid, and pia mater (Figure 2.1) [25]. The dura mater is a tough fibrous membrane comprising two layers. While the outer layer (endosteal layer) is firmly attached to the skull's inner surface, some regions of the inner layer (meningeal layer) extend inward to form the falx cerebri, falx cerebelli, and tentorium cerebelli. The dura mater membrane constrains brain movement and separates the different parts of the brain. The falx cerebri is the largest dura mater membrane that separates the left and right cerebral hemispheres. The arachnoid mater lies beneath the dura mater and is separated from the dura mater by the subdural space. Similarly, the pia mater adhered to the brain surface is separated from the arachnoid mater by a narrow space referred to as the subarachnoid space. The subarachnoid space contains the CSF, a colorless fluid surrounding the brain that circulates in the ventricles of the brain.

The falx and tentorium have a thickness of 0.35–1.11 mm and exhibit viscoelastic properties [44]. The falx and tentorium serve to maintain the position of the brain and, thus, can affect the brain's mechanics. The existence of the falx and tentorium was found to decrease the strain in the peripheral regions and increase the strain in the central region compared to head models without these membranes [45]. The tensile strength and modulus of these dura mater membranes were found to range from 3.3 to 7.9 MPa and 21.3 to 75.0 MPa, respectively [44], [46]. Unlike the scalp, the modulus and tensile strength of the dura mater showed no dramatic change with age [46].

2.1.4 CSF

CSF plays a crucial role in maintaining the brain's function and can cushion the brain from mechanical shock during head impacts. The volume of CSF in adults is 135–150 ml, with approximately 35 ml in the ventricles and 100–125 ml in the subarachnoid space [25]. CSF is normally composed of 99% of water and 1% of lipids and proteins. Thus, the density of CSF is close to that of water (1,000 kg/m^3) [47]. The CSFP is normally 10–15 mm Hg (i.e., 1,333–2,000 Pa) [48].

CSF is a Newtonian fluid with a viscosity of 0.7–1 mPa-s at 37°C [49]. It has been found that the protein and cell concentrations in the CSF have no significant influence on its viscosity [49]. The bulk modulus of 2.1–2.2 GPa has been used for the CSF in several numerical simulation studies, which is similar to the modulus of pure water [50], [51]. Numerical studies have shown that the presence of CSF remarkably reduces the brain strains caused by head impacts [52], [53]. Therefore, properly modeling the CSF of a headform is necessary to accurately replicate head intracranial responses.

2.1.5 Brain

The brain consists of three parts: the cerebrum, cerebellum, and brain stem (Figure 2.4), which enfold four ventricles [25]. The cerebrum is the main part of the brain separated into two hemispheres by the falx membrane. The outer layer of the cerebrum is the grey matter with the cortex and nuclei, and the inner layer is the white matter mostly consisting of nerve fibers (i.e., axons). The cerebrum can be functionally divided into four main lobes: the frontal, temporal, occipital, and parietal lobes. The frontal lobe manages decision-making and motor functions. The parietal lobe affects sensation and body position. The temporal lobe is responsible for memory and language skills, and the occipital lobe controls visual functions. Damage to any part of the cerebrum can destroy the functional ability of these lobes and, as a result, affect an individual's well-being.

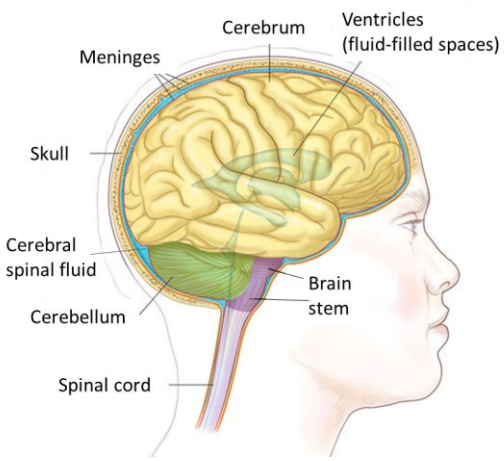

Figure 2.4. Anatomy of the brain (copyright permission from Terese Winslow LLC).

The typical physical and mechanical properties of the brain are critical to brain mechanical responses and are important in the design of head-brain models. The mass of the brain is 1290–1350 g and the volume is 1297–1338 cm^3 from a study with volunteers aged 21–

65 years old [54]. The brain's volume decreases with age, and males (mean of 1.3 kg) have slightly larger brains than females (mean of 1.2 kg) [54], [55].

The brain is nearly incompressible with a Poisson ratio of approximately 0.5 [56], [57]. Due to the nonlinear viscoelastic behavior of the brain, the stress-strain relation has no linear behavior from which a meaningful elastic modulus could be determined [56]. Therefore, the bulk and shear moduli are of interest in studies characterizing the material properties of the brain. The reported bulk modulus of the brain ranges from 2.3 to 2.7 GPa whereas the shear modulus is on the order of kilopascals [58], [59]. Therefore, the brain is resistant to compression while vulnerable to shear loading. In addition, the brain's mechanical behavior is highly sensitive to its strain and strain rate, with increasing stiffness at higher strain and loading rates [23]. Some studies also suggest that the brain exhibits mechanical anisotropy and regional variations due to the structural anisotropy of its white and grey matter [60], [61]. Nevertheless, there is no agreement on the constitutive model that best describes the material behavior of the brain due to the complexity of its material properties.

2.2 Brain Injuries and Injury Mechanisms

Blunt impact on the head can lead to skull deformations and create abrupt relative motion between the skull and brain. If the loading energy exceeds the tolerance of the skull and brain, impacts can cause skull fractures and TBIs. TBIs are generally classified as either focal or diffuse injuries [62]. Focal injuries, such as brain contusion and hematoma, refer to localized tissue damage. A contusion is the bruising of the brain tissue and occurs under the impact site or at the distal site of the impact. A hematoma involves bleeding due to the rupture of veins in the brain or dura mater space [62]. Commonly associated with damage to neuronal

tissue, diffuse brain injury is usually widespread within the brain and characterized by a loss of consciousness [62]. Both focal and diffuse injuries can be fatal or cause long-term sequelae.

Numerous research associates the theories of TBI mechanisms with head kinematics. Most theories assume that a measurable mechanical quantity that scales the severity of a head impact can infer the likelihood of injury. Kinematics such as linear acceleration, angular acceleration, and angular velocity have been correlated to TBI [63]. Rapid linear or rotational acceleration can cause relative motion between the skull and brain, since the skull moves due to acceleration while the brain remains stationary due to inertia [63]. This relative motion can cause the inner contours of the skull to collide with the brain, leading to focal brain injuries [64]. For diffuse injury, some researchers believe that rotational motion leads to shear stresses in the brain tissue where adjacent parts experience different inertial movements due to local variations in density [65]–[67]. Additionally, translational acceleration can also cause a concentration of shear stresses on the corpus callosum and the brainstem, resulting in diffuse axonal injuries (DAIs) [68]–[70].

Another theory associates the TBI mechanisms with ICP. Both skull deformation and head acceleration can result in ICP changes [18]. In contact impacts to the head, the stress wave generated at the impact site of the skull propagates to the distal site, leading to ICP change throughout the CSF and brain. The inward-bending deformation caused by the impact can lead to a positive ICP, and the rebound of the deformation can cause a negative ICP [72]. Meanwhile, due to linear acceleration, the skull pushing toward the brain can increase the ICP at the impact site, decrease the ICP at the distal site, and create pressure gradients throughout the brain between the two sites [73]. The increased pressure, decreased pressure, and pressure gradients are associated with compression, stretch, and shear of brain tissue, respectively [72].

Since brain tissue is sensitive to shear, pressure gradients can be detrimental. Numerous studies have demonstrated the connection between ICP and TBI [71], [74], [75]; however, an in-depth understanding of ICP mechanisms requires additional research. Developing a headform to measure ICP is valuable for better understanding TBI mechanisms.

2.3 Head Injury Criteria and Helmet Certifications

Some of the mechanics discussed above have been correlated with injury likelihood in the form of functions, referred to as injury criteria. These injury criteria are typically mathematical expressions, sometimes represented graphically, that allow researchers to infer injury risk based on the magnitude and duration of measured mechanics. While most injury risk functions are acknowledged to be limited in application, some have proved useful in assessing safety devices, serving as helmet assessment certifications, for example.

Both head kinematics and intracranial mechanics have been associated with the risk of TBIs. Sections 2.3.1 and 2.3.2 introduce the injury criteria based on head kinematics and tissue-level parameters (i.e., intracranial mechanics), respectively. Section 2.3.3 summarizes the criteria used in helmet certification tests.

2.3.1 Kinematics-Based Criteria

Various injury criteria have been developed based on pure head kinematics, summarized in Table 2.3. A group at Wayne State University created the Wayne State Cerebral Concussion Tolerance Curve (WSTC), the earliest tolerance model based on human cadavers [76]. Distinguished by a decreasing curve of the acceleration magnitude versus duration (Figure 2.5), this model indicates that lower acceleration magnitudes require longer pulse durations to result in a severe injury. Acceleration data points above the curve represent unsafe

impacts that can cause irreversible brain injuries. Data points below the curve represent non-fatal impacts that may cause reversible brain injuries. This curve was based on linear skull fracture tolerance, assuming that skull fractures were concomitant with concussions according to the observed prevalence relation between these two injuries [76]. However, this assumption may be not valid, as brain injuries, even without a skull fracture, can prove debilitating or fatal.

Inspired by the WSTC, the Severity Index (SI) was developed as the time integral of the linear acceleration [77]. The SI criterion is not valid for impacts with long durations. Thus, the Head Injury Criterion (HIC) chooses a time window of the acceleration for the integration to exclude the concern of long durations (Table 2.3). HIC is one of the most commonly used criteria in injury research and has been adopted in helmet and motor vehicle tests [78]. Nevertheless, the HIC does not consider the effect of rotational motion.

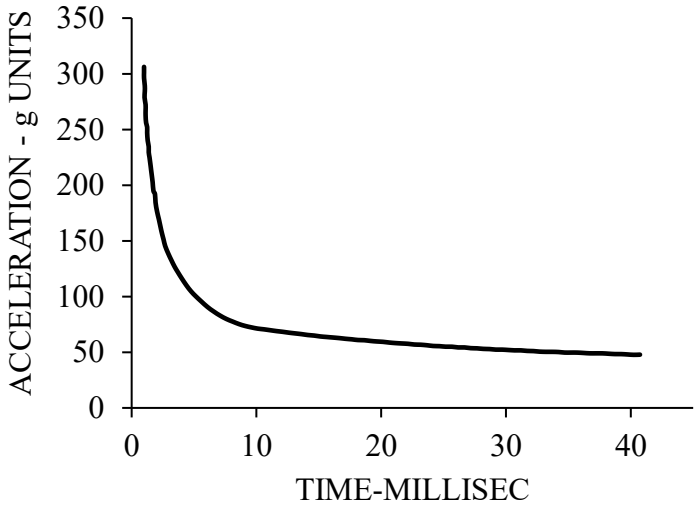

Figure 2.5. The Wayne State Tolerance Curve (acceleration vs. duration of acceleration pulse) [76]. Figure is reproduced with permission from the publisher of [76].

Table 2.3. A summary of the typical injury criteria based on kinematics.

Injury Criterion	Equation	Measurement
Severity Index (SI) [77]	$SI = \int a(t)^{2.5}\, dt$	Linear acceleration
Head Injury Criteria (HIC) [78]	$HIC = \left\{ (t_2 - t_1) \left[\frac{1}{t_2 - t_1} \int_{t_1}^{t_2} a(t)dt \right]^{2.5} \right\}_{max}$	Linear acceleration
Rotational Injury Criterion (RIC) [79]	$RIC = \left\{ (t_2 - t_1) \left[\frac{1}{t_2 - t_1} \int_{t_1}^{t_2} \alpha(t)dt \right]^{2.5} \right\}_{max}$	Angular acceleration
Brain Injury Criteria (BrIC) [80]	$BrIC = \left\{ \sum_{i=x,y,z} \left(\frac{\omega_i}{\omega_{i,c}} \right)^2 \right\}^{1/2}$	Angular velocity
Rotational Brain Injury Criterion (BRIC) [81]	$BRIC = \frac{\omega_{max}}{\omega_c} + \frac{\alpha_{max}}{\alpha_c}$	Angular velocity and acceleration
A Generalized Model for Brain Injury Threshold GAMBIT [82]	$GAMBIT = \max_t \sqrt{\left[\left(\frac{a_{max}}{a_c} \right)^2 + \left(\frac{\alpha_{max}}{\alpha_c} \right)^2 \right]}$	Linear and angular acceleration
Head Injury Power (HIP) [83]	$HIP = m \sum_{i=x,y,z} a_i \int a_i dt + \sum_{i=x,y,z} I_{ii} \alpha_i \int \alpha_i dt$	Linear and angular acceleration

Due to the association of angular kinematics with brain injuries, a few criteria have incorporated angular acceleration or velocity. A study introduced the Brain Injury Criterion (BrIC) based on pure angular velocity, since numerical simulations found that angular velocity is strongly correlated with brain strains [80]. However, this finding contradicts results from real-world field studies that suggest brain injury is related to both linear and angular motions.

Rowson et al. correlated kinematics from laboratory reconstructions of head impacts in football games with athletes' concussion levels [84]. The research found that a combination of linear and angular head accelerations is better than pure linear or angular accelerations in predicting concussions. Historically, Newman et al. proposed a generalized acceleration model for brain injury, which combines peak linear accelerations and peak angular accelerations [82]. Later, Newman et al. introduced a more detailed approach, the Head Impact Power (HIP), which takes into account head mass, impact time, and three-dimensional linear and angular accelerations [83].

Although some injury criteria include both linear and angular kinematics, the kinematics-based criteria fail to account for injury factors such as skull deformation, impactor shape, and the head mass and size of injured individuals. For example, the HIC is inapplicable to crushing situations (where head movement is constrained during impact), because skull deformations may lead to brain injury when the head accelerations are constrained [85], [86]. The HIC also underestimates the injury risk for impacts with a large impactor mass and a low impact velocity, where the skull deformation has a greater effect than the head acceleration on brain responses [87]. Moreover, these criteria based on head kinematics cannot provide detailed information on brain responses to distinguish between diffuse and focal injuries. Therefore, some studies suggest using brain tissue-level parameters to complement the kinematics-based criteria, since these tissue-level parameters directly involve the responses of the brain [88], [89].

2.3.2 Tissue-Level Injury Criteria

Injury criteria based on tissue-level parameters, such as ICP as well as brain strain and stress, have been evaluated in numerical simulations. Table 2.4 summarizes the tissue-level injury criteria proposed for TBIs. The earliest tolerance model based on ICP is the Intracranial Pressure Time Tolerance Curve [76]. This curve shows the relationship between ICP peak and duration that represent concussion boundaries, but the curve does not apply to humans as it was obtained from animal studies. Correlating ICP estimated from numerical simulations with brain injury severity, Ward et al. and Kleiven et al. proposed injury criteria based on the maximum and minimum ICP [90], [91]. Takhounts et al. proposed the cumulative strain damage measure (CSDM) and maximum principal strain (MPS) as injury metrics of DAIs [75], [88]. Other proposed injury metrics are based on shear stresses and brain motions [75], [88].

The tissue-level injury criteria are limited to studies using the finite element (FE) method, since measuring these intracranial mechanics in human or animal heads is technically challenging. Additionally, there is a lack of adequate headforms that can measure tissue-level parameters. FE modeling relies on the appropriate selection of material models, mesh elements, and boundary conditions, and errors in this process can result in simulation results that significantly deviate from those of realistic outcomes. Moreover, since FE models do not allow for direct tests of helmets and current headforms cannot measure intracranial parameters, tissue-level criteria have not been directly applied to the assessment of safety devices. Headforms that can measure tissue-level parameters such as ICP and strains may be a valuable tool to extend the depth of TBI research and improve the assessment method of safety devices in sports and motor vehicles.

Table 2.4. A summary of injury criteria based on brain tissue-level parameters.

Injury criterion	Reference	Parameters	Threshold	Injury
ICP	Ward et al. [90]	CSFP	Max ICP> 234.4 kPa	Severe brain injury
	Ward et al. [90]	CSFP	Max ICP>172.4 kPa	Moderate brain injury
	Kleiven et al. [92]	ICP in grey matter	Max ICP=65.8 kPa	50% risk of concussion
	Kleiven et al. Kleiven et al. [92]	ICP in white matter	Min ICP =-55.1 kPa	50% risk of concussion
Dilatational damage measure (DDM)	Takhounts et al. [14]	Volume fraction of the brain tissue that exceeds predefined ICP	DDM-100kPa=7.2% (7.2% brain tissue volume exceeds negative 100 kPa)	50% risk of contusion
Maximum principal stress (σ_{max})	Shreiber et al. [93]	σ_{max}	σ_{max} =7.8 kPa	50% risk of contusion
Maximum principal strain (ε_{max})	Shreiber et al. [93]	ε_{max}	ε_{max}=0.188	50% risk of contusion
Relative Motion Damage Measure (RMDM)	Takhounts et al. [14]	Brain displacement relative to the skull's inner surface	RMDM=1mm	50% risk of acute subdural hematoma
Cumulative Strain Damage Measure (CSDM)	Marjoux et al. [94] Marjoux et al. [94] Kleiven et al. [92]	Volume fraction of the brain part that exceeds predefined strain levels	CSDM0.15 = 25%* CSDM0.15 = 44% CSDM0.1= 47%	50% risk of moderate DAI 50% risk of severe DAI 50% risk of concussion

*: The portion of brain tissue with tensile strain greater than 0.15 is 25%

2.3.3 Helmet Certifications

Headforms are a valuable tool in helmet certification tests. With the primary function of protecting the head, helmets are required to undergo certification tests to validate their protective performance. Common standard tests involve a series of controlled impacts where the helmet, worn on a standard headform, is dropped onto an anvil from a predetermined height, as shown in Figure 2.6. The value of the assessment criterion is calculated using the parameters measured from the headform. If the assessment criterion exceeds the standard

threshold, then the helmet is determined to fail in protecting the head; otherwise, the helmet is certified safe and can be sold commercially.

Currently, all helmet certifications adopt assessment criteria based on kinematics, such as the HIC, linear acceleration, and angular velocity. Table 2.5 summarizes the typical criteria used in standard tests for various helmet types. The most widely used criteria are the HIC and linear acceleration peaks. Although various tissue-level injury criteria may be applied to helmet tests, no helmet certifications use intracranial measurements. A primary reason is likely the lack of headforms providing intracranial measurements. According to current research, the headforms used for helmet tests can only measure head kinematics [95].

Figure 2.6. An illustration of helmet certification tests where a headform dons the testing helmet before being dropped to an anvil on the ground.

Table 2.5. Typical helmet certification standards and criteria for drop tests.

Standard	Helmet	Impact velocity	Pass Criterion
ASTM F1045-16	Ice Hockey	4.5 m/s	a<275 g
CSA Z262.1-09	Ice-Hockey	4.5 m/s	a<275 g
NOCSAE ND002-13m15	Football	5.46 m/s	SI<1200
NOCSAE ND002-17m17a	Football	6 m/s	SI<1200, α<6000 rad/s^2
ECE Reg 22	Motorcycle	7.5 m/s	a<275 g, HIC<2400
Snell M2020R	Motorcycle	7.75 m/s	a<275 g, HIC<2880
CPSC	Cycling	6.2 m/s (flat anvil) 4.57 m/s (curbstone anvil)	a<300g

ASTM: American Society for Testing and Materials; CSA: Canadian Standards Association. NOCSAE: National Operating Committee on Standards for Athletic Equipment; ECE: Economic Commission for Europe. CPSC: Consumer Products Safety Commission required by US law.

2.4 Headforms

Headforms are useful tools in laboratory tests where organic human and animal models are not adequate. Human volunteers and PMHS are best in terms of providing realistic mechanical and physiological responses, but human volunteers are restricted to noninjury impacts while PMHS are rare and difficult to obtain. Ethical concerns also limit the use of organic human models. Animal models are more accessible than PMHS, but they are not suitable for helmet tests due to their great morphological difference from human heads. The use of animal models is limited by ethical restrictions as well. Furthermore, PMHS and animal models generally cannot be reused as the mechanical properties of biological tissue can vary with temperature, humidity, and degradation of the tissue in the long term. Headforms cannot provide physiological responses; other than this limitation, headforms are easy to manipulate

with no need for chemical methods to treat and store them. Headforms are efficient in experiments since they are reusable and ready for use once they have been set up. Thus, a single headform can provide a large sample size with minimal cost. Moreover, headforms can precisely mimic the geometry of the human head, which allows for the simulation of head interactions with the surrounding environment, in contrast to animal models. Compared to numerical models, headforms are more efficient for safety device tests without the need to model helmets or motor vehicles. Thus, research questions that use mechanics-based measures of head responses to find solutions widely prefer headforms to other models.

2.4.1 Design Requirements of Headforms

To replace human heads in experiments, the basic requirement is that headforms must be biofidelic and repeatable so that they can produce responses similar to humans under comparable conditions and offer reliable measurements during repeated tests [11].

(1) Biofidelity

Human surrogate headforms are designed to match living humans in anthropometry, articulations, and structure responses, and to exhibit the same level of typical responses (e.g., skull deformations and head accelerations) depending on the experimental objectives [11]. Headforms for biomechanical tests must exhibit both external biofidelity (i.e., realistic external geometry to replicate interactions between the head and its surrounding safety gear) and internal biofidelity (i.e., realistic mechanics). External biofidelity is generally not a concern as human geometry is easy to replicate with modern measurement and manufacturing techniques. Conversely, the internal biofidelity of each newly developed headform is a critical concern that

requires validation, as internal biofidelity depends on a range of complex factors such as structures and materials of the headform components.

There are several methods for quantitatively assessing the internal biofidelity based on a comparison of headform responses and human cadaveric data. The ISO/TR 9790 defines the biofidelity ratings of a dummy human model for side impact based on the differences between the surrogate and cadaveric data [96]. Experts contributing to the standard assume the rating is "10" if the response meets the specified requirement, "5" if the response is outside the requirement but within a corridor width of the response, and "0" if the response is outside the defined corridor width. For example, the ISO/TR 9790 defines the biofidelity rating of the dummy head based on the resultant linear acceleration at the center of gravity for a lateral drop from 20 cm to a rigid plate. The standard specifies that a rating is "10" if the peak acceleration is within 110 ± 11 g (g: acceleration due to gravity, 9.8 m/sec^2) and "5" if the peak acceleration is beyond 110 ± 11 g but within 110 ± 22 g. Otherwise, the rating is "0". Based on the ratings, the ISO/TR 9790 classifies the biofidelity levels into five categories: unacceptable (<2.6), marginal (2.6~4.4), fair (4.4~6.5), good (6.5~8.6), and excellent (8.6~10) [96].

In addition to the aforementioned biofidelity assessment standard for side impact responses, the ISO/WD 15830-2 document defines a requirement for the front impact responses [97]. Based on the ISO/TR 9790, the ISO/WD 15830-2 standard technical document specifies that the biofidelity rating is "10" if the peak acceleration for a 37.7 cm forehead drop is within 250 ± 25 g, and the rating is "5" if the peak acceleration is beyond 250 ± 25 g range but within 250 ± 50 g. As can be seen from the two requirements, the corridors defined between the rating "10" and "0" is peak ± 10% and peak ± 20% of the peak.

The biofidelity standards specified in the ISO/TR 9790 and ISO/WD 15830-2 documents cannot fully describe the closeness between the surrogate's and human's data. These standards evaluate only the peaks, although the response over time is also important as demonstrated by the WSTC, SI, and HIC injury criteria. To describe the time histories of responses, Rhule et al. developed the Biofidelity Ranking System (BioRank) to compare the surrogate responses to the mean cadaver responses over time [98]. The BioRank calculates the ratio (R) of the cumulative variance between the surrogate response and the mean cadaver response (DVC) over the cumulative variance between the mean human response and the mean plus one standard deviation (CCV): R = DVC/CCV [98]. The lower R indicates the lower difference between the surrogate response and the human mean response. A square root of R ($\sqrt{R}$) lower than "1" means that the surrogate response is within one standard deviation from the mean human response; $\sqrt{R}$ between 2 and 3 means the surrogate response is between 2 and 3 standard deviations from the mean human responses. Parent et al. classified the biofidelity levels into four groups: excellent ($\sqrt{R} \leq 1$), good ($1<\sqrt{R}\leq 2$), marginal ($2<\sqrt{R}\leq 3$), and poor ($3<\sqrt{R}$) [99]. The measure R captures the combined effects of the shape and magnitude of the responses, but it cannot distinguish these effects individually.

Among methods of calculating biofidelity ratings, CORrelation and Analysis (CORA) considers the various aspects of information of the time histories. CORA is a rating method that calculates the level of closeness between time series. It includes a set of algorithms that quantify the level of correlations based on the signal corridor fit, shape, size, and phase shift as shown in Figure 2.7 [100]. The result for each factor is a rating value ranging from "0" to "1", and the total rating is the sum of the weighted ratings. A rating of "0" indicates that the

testing measurement matches poorly with the reference measurement, and a rating of "1" corresponds to a perfect match. Therefore, the CORA ratings can determine the level of biofidelity based on multiple features of the measurement [43]. Weights of considering factors are defaulted in the software CORA (Total rating = 50% corridor rating + 25% shape rating + 12.5% size rating + 12.5% phase rating) [100].

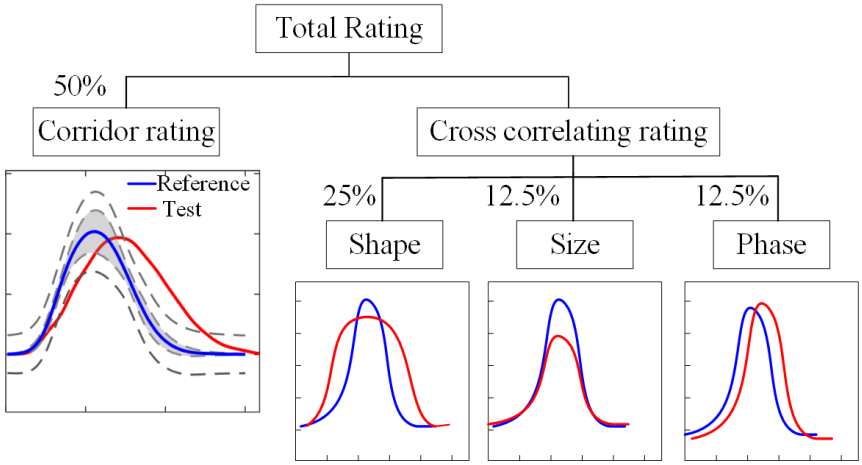

Figure 2.7. CORA method structure. The total rating is a summation of 50% of the corridor rating, 25% of the shape rating, 12.5% of the size rating, and 12.5% of the phase rating.

The algorithms of CORA include two independent sub-methods, the corridor metric and the cross-correlation metric, and the results rely on the parameters that control tolerances. For example, the corridor rating C is the average of time-step ratings C_i calculated through the following algorithm [100]:

$$C_i = \begin{cases} 1 & if\ |y(t_i) - x(t_i)| < d_{in}(t_i) \\ \left(\frac{d_{out}(t_i) - |y(t_i) - x(t_i)|}{d_{out}(t_i) - d_{in}(t_i)}\right)^k & d_{in}(t_i) \le |y(t_i) - x(t_i)|) \le d_{out}(t_i) \\ 0 & if\ |y(t_i) - x(t_i)| > d_{out}(t_i) \end{cases} \quad \textbf{Equation 2.1}$$

$$C = \frac{\sum_{i=1}^{n} C_i}{n} \; with \; 0 \leq C_i \leq 1 \qquad \textbf{Equation 2.2}$$

where d_{out} is the outer corridor width (distance between the corridor and the reference signal), d_{in} is the inner corridor width, and $y(t_i)$ and $x(t_i)$ are the test and reference signals, respectively. The equation indicates that the rating is "0" if a data point lies outside the outer corridor and the rating is "1" if it lies within the inner corridor (Figure 2.8).

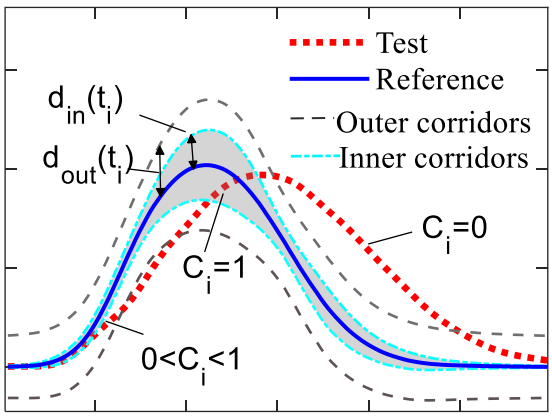

Figure 2.8. Illustration of the corridor method.

Ratings for the shape, phase, and size of the measurement are calculated based on the cross-correlation of the two signals. The shape rating depends on the maximum normalized cross-correlation. A rating of "1" means the shapes of the two signals are the same. The phase rating is calculated using the time shift at the maximum cross-correlation and controlled by the time intervals. The size rating depends on the ratio of the areas under the curves at the maximum cross-correlation. The different ratings interact but emphasize different aspects of the measurement [100]. Therefore, the CORA method provides a comprehensive evaluation of the similarity of the time histories.

There is currently no standard biofidelity interpretation and classification based on the absolute CORA ratings, and the ratings depend on user default parameters such as d_{in} and d_{out}. However, CORA provides a relative comparison between different head surrogates. Using the software defaulted parameters, some researchers agreed that a total CORA rating of 0.7 can indicate good biofidelity of the surrogate [101].

Repeatability: As headforms are subjected to repeated regulatory tests, their responses should be repeatable to provide reliable results. The ISO/WD 15830-2 suggests using the coefficient of variation (COV) to determine the repeatability of a dummy human model [97]. The COV is the division of the standard deviation (σ) by the mean (μ) of the repeated tests (i.e., COV = σ/μ). The repeatability of a surrogate is classified into four groups: unacceptable (>10%), marginal (7%~10%), good (3%~7%), and excellent (≤3%).

2.4.2 Current Headforms

Currently, headforms available for biomechanical research and helmet assessments focus on replicating global head responses or skull responses, such as head kinematics, impact force, and pressure on the skull. Figure 2.9 shows the headforms commonly used in head injury research and helmet tests. The Hybrid III consists of an aluminum skull cap and a removable vinyl skin [12]. It is normally equipped with nine uniaxial accelerometers at the mass center of the headform to measure head kinematics. The kinematic biofidelity of the Hybrid III headform was validated for front impacts via comparison with the peak accelerations of cadaver heads [102]. Since it has no simulants for intracranial soft tissue, the Hybrid III headform can only reconstruct the global kinematics of human heads. Another typical headform, the FOCUS, matches the head dimensions, facial features, and skull structures of the human head. It can be

instrumented with load cells on the skull to measure the impact force [103]. Some standard headforms for helmet certification tests, such as the EN960 and ISO/DIS6220 standards, comprise only a headlike skull shell [104]. These headforms have no morphological internal components such as the meninges, CSF, and brain, all of which are crucial for determining intracranial responses.

Based on literature research on commercially available headforms, only the standard headform used by the NOCSAE includes a silicon brain simulant in a polyethylene skull [105]. The simulant brain only serves as a mass representative of the human brain and its material properties are not considered to accurately simulate the brain responses. This headform is instrumented with accelerometers to evaluate the performance of football helmets during certification tests [106].

Hybrid III EN960 ISO/DIS 6220

Figure 2.9. Commercially available headforms commonly used in head injury research and helmet tests. Images of headforms based on EN960 and ISO/DIS 6220 standards were from cadexinc.com, and used with permission.

A limited number of studies have sought to develop headforms that can replicate the ICP of the human head. Freitas et al. presented a surrogate made with a human cranium and surrogate brain to investigate the mechanics of ballistic strikes on helmeted heads [17]. Four

pressure transducers were installed on the brain surface to measure CSFP [17]. However, the measurements from this headform lack validation against human cadaveric data, and the headform is not reusable since the biological human cranium cannot maintain its material properties and tends to fracture during impact. Merkle et al. developed a physical surrogate of the human head for measuring ICP in blasts [107]. This headform consists of a skull made with the glass and epoxy mixture, a brain and brain stem made with silicone, and facial structures made with syntactic foams. The headform is instrumented with sensors in the brain to measure the IPP and brain displacement. To our knowledge, no research has investigated the suitability of using this headform in blunt impact. Recently, Petrone et al. introduced an instrumented headform that integrated a 3D-printed skull, brain surrogate, CSF surrogate, and rubber skin [19], [21]. Linear accelerometers and angular rate sensors installed on the skull and in the brain captured linear and angular kinematics of the skull as well as those of the brain. In addition, ten pressure sensors on the inner surface of the skull measured the CSFP at various locations. The mechanical properties of the surrogate materials and CSFP have been validated through comparisons with cadaver heads. The frontal and parietal CSFP peaks were within the range of pressure peaks in Nahum et al.'s cadaveric study for the same linear acceleration peaks [108]. However, the biofidelity of kinematics to blunt impacts has not been evaluated from published research.

2.4.3 Headform Used in This Research: BIPED

The first well-developed BIPED mark 1 (mk1) was fully designed by Ouellet et al. at Defense Research and Development Canada Valcartier. The device was initially developed to study ICP induced by blast overpressure. With further modifications, the next generation of

the BIPED (BIPED mk2) is expected to be applicable to blunt impact loadings as well. The BIPED throughout this paper refers to the BIPED mk1.

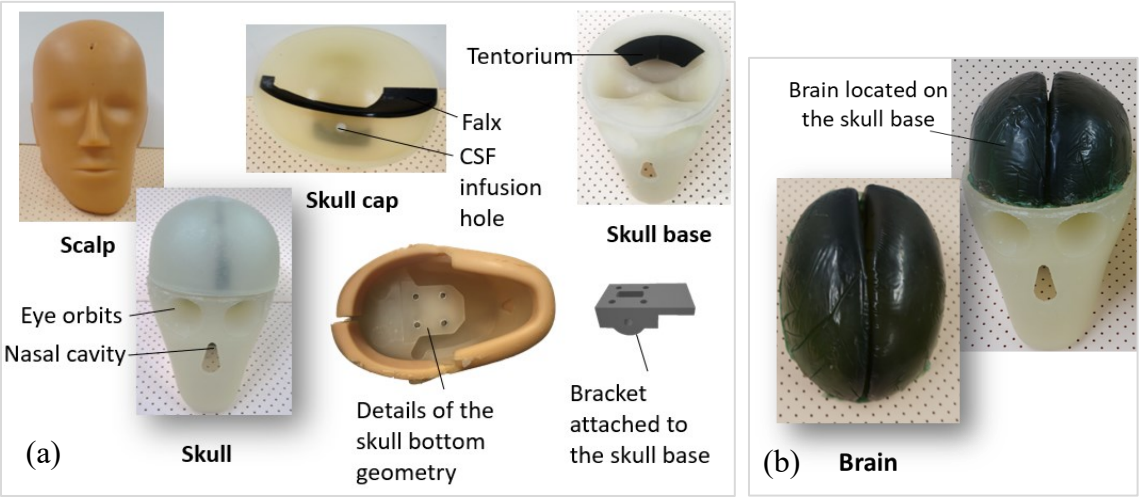

Figure 2.10. BIPED components: scalp, skull cap, skull base, falx, and tentorium membranes attached to the skull (a), and the brain simulant on the basilar skull. The bottom of the skull base has a flat area with four blind holes, allowing for connecting the headform to a surrogate neck with the bracket attached to the skull base.

The development of the BIPED targeted achieving biofidelic external geometry, internal geometry, and headform materials that replicate the stress transmission within the human head. The BIPED consists of a surrogate skin, two halved surrogate skull structures, a falx membrane, a tentorium, CSF, and a brain simulant (Figure 2.10). As shown in Figure 2.10 (a), the skin and skull have simplified facial features, including eyes, nose, mouth, and ears, allowing for modeling the interaction between the human head and the surrounding objects such as a helmet. The rubber falx and tentorium membranes are attached to the skull cap and base, respectively. A threaded hole (1/8-inch diameter) on the skull vertex allows the infusion of the surrogate CSF (i.e., saline) into the cranium. After filling the cranial space with saline,

the hole can be plugged with a plastic screw and sealed with silicone. The bottom of the skull base has a flat area with four blind holes, allowing for connecting the headform to other surrogate necks. In this research, a custom-designed bracket was attached to the BIPED at the flat area (Figure 2.10 (a)). The bracket served as a medium to connect the headform with the Hybrid III neck or to add other equipment such as a security rope to the headform. The brain surrogate made with silicone gel (Sylgard 527, Dow Corning) simulates the two-hemisphere brain cerebrum and incorporates the brain cerebellum and brain stem as a single unit (Figure 2.10 (b)).

The top half geometry of the head was based on the ISO J headform, and the internal cranial features were based on a commercially available three-dimensional model of the human skeleton [109]. The external facial features were inspired by the Canada Standards Association CAN/CSA headform and published anthropometric surveys [110]. The skull dimensions approximate the 50^{th} percentile male, and the brain surrogate volume (1491 cm^3) fits the cranial cavity with an average gap of 5 mm relative to the inner surface of the skull. The surrogate scalp of 6 mm nominal thickness tightly fits the skull [111].

Materials of the head components were selected mainly based on their density, mechanical properties, robustness, manufacture, and manipulation [22]. The density and elastic modulus, which determine the head mass and elastic wave speed in the materials, were the basic properties taken into consideration since the BIPED was initially developed for studying the ICP induced by low-intensity blast waves. The durability and resistance of the surrogate materials are also important as the headform is expected to be reusable in multiple experiments. Based on these factors, the TC-854 A/B Polyurethane (BJB Enterprise Inc., CA United States),

Sylgard 527 (Dow Corning Corporation, MI United States), and saline water were used as the surrogate materials for the skull, brain, and CSF, respectively [22], [111].

The thickness (6.35 mm), density (1200 kg/m^3), and Young's modulus (2.275 GPa) of the surrogate skull are in the range of reported cadaveric skull properties [40], [112]. The density (970 kg/m^3) and bulk modulus (1.065 GPa) of the surrogate brain are close to those of the human brain (1040 kg/m^3 and 2.07 GPa) [113], [114]. The Sylgard 527 silicone gel is nearly incompressible with a Poisson's ratio approaching 0.5 [115], similar to that of the human brain tissue (0.49–0.5) [60]. While brain tissue exhibits non-linear viscoelastic behavior with shear softening above 5% strain [116], the Sylgard 527 behaves as a linear viscoelastic solid for strain up to 50%. Since the bulk modulus of the Sylgard 527 has a magnitude in the order of 1 GPa while the shear modulus magnitude is in the order of 1 kPa [117], [118], the brain pressure measured with a pressure sensor depends mainly on the bulk property of the material. As a result, the effect of non-linear shear behavior on intracranial pressure is negligible since shear softening properties only apply to deviatoric behavior. The surrogate scalp was molded with urethane Vytaflex 20 (Smooth-On Inc., CA United States) since it has a similar density as the human scalp, and it is durable while flexible for the installation of the scalp [22].

The BIPED was the main headform used in the thesis due to its realism in terms of internal structures and materials as well as its robustness for repetitive impacts. Compared to the commonly used headforms, such as the Hybrid III, FOCUS, and EN960 headforms described in Section 2.4.2, the BIPED is a more realistic representation of the human head. The BIPED includes many more anatomy details, and the material properties of the BIPED deformable skull are closer to the human skull in comparison to the commonly used headforms

made with a hollow medal skull. The structure and the material of the headform components determine the capability of providing realistic intracranial mechanical measurements. A few headforms, such as the one developed by Freitas et al., included head internal components to measure ICP. However, the one from Freitas et al. was not intended for multiple uses since it used a human cranium that might degrade in the long term and tend to fracture with intensive impacts [17]. Despite the advantages of the BIPED over many other headforms, the BIPED was originally designed for measuring ICP in blast where the wave propagation speed was a key property for consideration. Therefore, some critical properties relevant to impact responses such as head stiffness were not well considered. Whether the BIPED can provide biofidelic and repeatable kinematic and ICP responses in blunt impacts is unknown.

Chapters 3 and 4 describe the studies of characterizing the biofidelity and repeatability of the BIPED based on kinematics and ICP to understand the design and responses of the BIPED, and Chapter 5 describes the study of refining the BIPED design to improve its biofidelity for application to blunt impacts.

Chapter 3 Characterization of the Kinematic Biofidelity and Inter-test Repeatability of Acceleration and Intraparenchymal Pressure of the BIPED

This chapter focuses on characterizing the BIPED kinematic biofidelity and the inter-test repeatability of the measurements including impact accelerations and IPP. To evaluate the kinematic biofidelity, the work described in this chapter mainly compared the BIPED accelerations with cadaveric data from a previous study [119]. Since this cadaveric study did not measure ICP and no other studies have reported ICP data from the same impact condition, the study was unable to quantitatively evaluate the ICP biofidelity. The present study characterized the kinematics biofidelity and repeatability of the BIPED model and analyzed the main design factors of these characteristics. This is a crucial step toward a biofidelic headform measuring both global kinematics and ICP in blunt impact. The materials of this chapter have been published in an original research paper [120].

3.1 Introduction

Head injury classifications range in severity from mild to severe, with injury outcomes including functional disabilities and, in the worst cases, death [2], [3]. Hospital admissions for head injury account for 9% of all trauma admissions in Canada, and 91% of these involve traumatic brain injuries (TBIs) [3]. The cost of acquired brain injuries and follow-up treatment is over $12.7 billion annually in Canada alone [121]. Understanding injury mechanisms and improving protective headgear performance are ongoing objectives to reduce the risk of injury.

Biomechanical research correlating impact mechanics with injury types and severities typically reports that impact acceleration positively correlates with the pressure in the brain and the disruption to brain tissue [122]. This observation leads researchers studying protective headgear to associate reductions in global head kinematics with a reduction in the likelihood of injury relative to an unprotected head, intending to infer the protective performance of headgear. Indeed, numerous studies have focused on quantifying injury severity through global head linear accelerations or angular kinematics [65], [123]. There is relatively less research work investigating intracranial variables in the context of quantifying the effect of head protection; however, some intracranial variables such as intracranial pressure (ICP) and brain stresses have shown great potential in assessing the risk of brain injury [124], [125]. A headform capable of measuring ICP, the pressure in the cerebrospinal fluid (CSF) or the brain, in addition to global head kinematics, may allow for the assessment of headgear based on global kinematics (that indicate global motion of the head and severity of impact sustained by the head) and ICP (that could arguably indicate disruptive effects to brain tissue).

A primary requirement for headforms is to offer biofidelic and repeatable measurements of mechanical parameters that are relevant for injury research questions or that allow for the quantification of impact attenuation. Biofidelity in this study focuses on the ability of the surrogate to measure mechanical parameters comparable to the human head responses in an impact event. A perfect head model would experience identical mechanics to the human head and would be referred to as biofidelic. Since no head model can perfectly match the human head, the dimension and physical properties of which also vary between individuals, assessments of biofidelity typically report the degree to which a model agrees with a specific dataset. The scale of biofidelity can be obtained through metrics such as the

cumulative variance of a response peak, and CORrelation and Analysis (CORA) ratings [126], [127].

As headforms are subjected to regulatory tests, their measures should also be repeatable to provide robust results. For example, the ISO/WD 15830, a document that provides specifications for the WorldSID 50th percentile male side impact dummy, uses the coefficient of variation (COV) to assess repeatability [97]. COV is the ratio of the standard deviation over the average of repeated tests [97]. Although the ISO/WD 15830 was designed for anthropomorphic test devices subjected to side impacts, the methods used to define the repeatability levels were also used for other head models and impact locations [128], [129].

Commercially available headforms for impact assessments measure only global head kinematics and there are very few headforms that measure both intracranial responses and global kinematics. The Hybrid III headform has been validated against cadaver skull acceleration magnitudes for direct front impacts [130], but it does not contain brain components. Another common headform used by the National Operating Committee on Standards for Athletic Equipment (NOCSAE) includes a polyethylene skull filled with glycerin brain simulant, but again, it solely measures global kinematics [12]. A recent study by Freitas et al. focused on the mechanics of ballistic strikes to helmeted heads, presenting a surrogate made with a human cranium and a surrogate brain [17]. Four transducers were installed at the brain surface to measure the ICP in the CSF. However, the measurements of this headform lack validation against human cadaveric data, and the headform is not re-usable since the human crania tend to fracture during impacts and their material properties are sensitive to the environment. Recently, Petrone et al. introduced an instrumented headform that integrated a 3D-printed skull, brain surrogate, CSF surrogate, and rubber skin [19], [21]. Accelerometers

and angular rate sensors were installed in the brain and on the skull to capture brain linear and angular kinematics and global head accelerations. In addition, ten pressure sensors were installed on the inner surface of the skull to measure the ICP in the CSF. The mechanical properties of the surrogate materials and ICP were validated against cadaveric data. The frontal and parietal pressures were demonstrated as being within the range of pressure peaks in Nahum et al.'s cadaveric study when matching their acceleration peaks [108]. However, the biofidelity of kinematic responses is unknown for this head model.

The first objective of the present study was to characterize the global kinematic biofidelity of a headform that was originally developed for research in blast scenarios, but that is now also considered for use under blunt impact scenarios. This model, named the Blast Injury Protection Evaluation Device (BIPED), comprises simulants for the skin, skull, and intracranial components. Drop impact tests were conducted with the BIPED and the commonly used Hybrid III head models, and measures from these experiments were compared to available literature data of cadaver heads subjected to similar impact conditions. The biofidelity of the acceleration response was assessed using statistical approaches including CORA. The second objective was to assess the repeatability of the global head kinematics and the ICP in the brain parenchyma, i.e., the intraparenchymal pressure (IPP). Biofidelity ratings of the IPP were not obtained due to a lack of cadaveric pressure data, specifically in drop impacts.

3.2 Method

3.2.1 Head Surrogate and Instrumentation

The BIPED comprises a surrogate scalp, two halved skulls, a fluid layer serving as the cerebrospinal fluid, tentorium and falx membranes, and a brain surrogate (Figure 3.1(a)).

Details on the development of this head surrogate, including the head geometry, material selection, and instrumentation can be found in previous literature [16], [22]. Briefly, the top half geometry of the head was based on the ISO J headform, and the internal cranial features were based on a commercially available three-dimensional model of the human skeleton [109]. The external facial features were inspired by the Canada Standards Association CAN/CSA headform and published anthropometric surveys [110]. The skull dimensions approximate the average male, and the brain surrogate volume (1491 cm^3) fits the cranial cavity with an average gap of 5 mm relative to the inner surface of the skull. Meninges except for the tentorium and falx membranes were excluded to simplify the structure. The surrogate scalp of 6 mm nominal thickness tightly fits the skull [111].

Materials of the head components were selected mainly based on their density, mechanical properties, and robustness [22]. The density and elastic modulus, which determine the elastic wave speed in the materials, were the basic properties considered since the BIPED was initially developed to study the effect of low intensity blast waves on the brain, where only very small deformations occur. Headforms are expected to be reusable for multiple experiments. Therefore, the durability and resistance of the surrogate materials are important. Based on these factors, the TC-854 A/B Polyurethane (BJB Enterprise Inc., CA United States), Sylgard 527 (Dow Corning Corporation, MI United States), and saline water were used as the surrogate materials for the skull, brain, and CSF, respectively [22], [111]. The thickness (6.35 mm), density (1200 kg/m^3), and Young's modulus (2.275 GPa) of the surrogate skull are in the range of reported cadaveric skull properties [40], [112]. The density (970 kg/m^3) and bulk modulus (1.065 GPa) of the surrogate brain are close to those of the human brain (1040 kg/m^3 and 2.07 GPa) [113], [114]. Urethane rubber made with Vytaflex 20 (Smooth-On Inc., CA

United States) was used as the surrogate scalp based on similar considerations [22]. Note that other material properties such as the shear modulus and viscosity of the brain also affect its strain states, but these properties are not yet considered in this model. The effects of complex properties such as nonlinear viscoelasticity and properties varying with strain rates were also ignored in this study; however, they could be explored in future work.

As shown in Figure 3.1(b) and (c), three pressure sensors (XCL-072, Kulite Semiconductor Products, NJ United States) were cast at the front, back, and right side within the brain parenchyma. The sensing tip coordinates (units: mm) were referenced with respect to the center of the BIPED neck mounting surface (Figure 3.1(b)) and were (62.3, -21.6, 70.8), (0, -58.4, 70.8), and (-73, -21.6, 70.8) for the front, side, and back IPP sensor, respectively (Table 3.1). The front and back sensor diaphragms were oriented toward the outside of the head along the x-axis and the side sensor diaphragm was oriented along the y axis toward the head surface. The back and front sensors were not in the midsagittal plane because the falx membrane was in this plane of the brain.

The brain pressure response of the BIPED has been compared to that of cadaver specimens for blast conditions [131]. The analysis focused on back IPP since the position of the back sensor in the BIPED was closest to that in the cadaver head [131]. The back IPP magnitude was found to be in good agreement with the cadaver response for three tested shock severities and two loading directions [131]. The IPP measures have also demonstrated repeatability for forehead drops onto a sports-field turf surface [111]. Nevertheless, the BIPED requires an in-depth assessment of both biofidelity and repeatability under blunt impacts at multiple heights and locations.

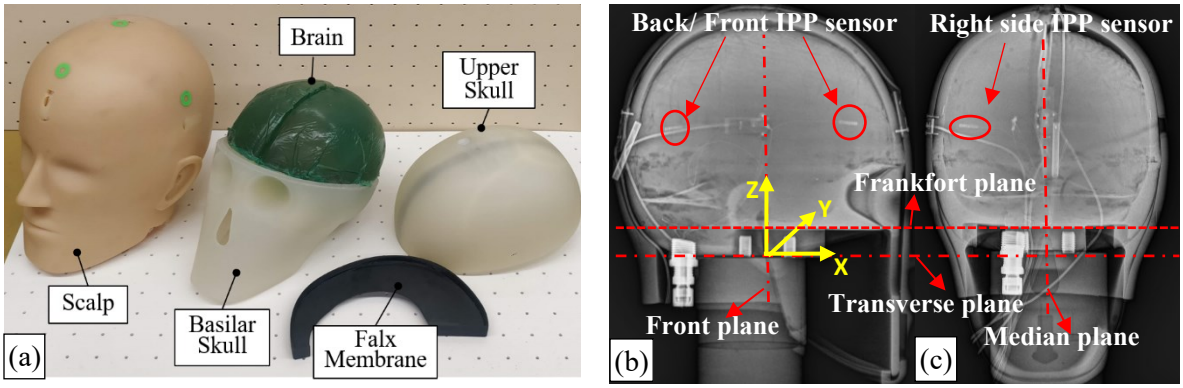

Figure 3.1. (a) View of the BIPED components showing the scalp, brain, basilar skull, upper skull cap, and falx membrane. (b) Right to left view of X-ray image showing back and front IPP sensors. (c) Front to back view of X-ray image showing the right side IPP sensor. The sensor and impact locations can be referred to the coordinate system originating at the center of the bottom neck mounting surface which is 12.6 mm to the Frankfort plane (shown in (b)).

Table 3.1. Location coordinates and depths of the IPP sensor sensing tips. The coordinate system has its origin at the center of the BIPED neck mounting surface, shown in Figure 3.1(b) and (c). The depths were the distance of the sensor tips from the brain surface in the transversal plane of the three sensors. The front and back IPP sensors were oriented along the x axis, with the front one following the positive direction and the back one following the negative direction. The side IPP sensor was oriented along the y axis in the positive direction.

Sensor	Front	Side	Back
Location (mm)	(62.3, -21.6, 70.8)	(0, -58.4, 70.8)	(-73, -21.6, 70.8)
Depth (mm)	18.7	8.5	14.8

3.2.2 Experimental Setup and Validation

To offer comparable impact conditions, we built a drop impact setup similar to the one used in a previous cadaver experiment [119]. The global linear accelerations were estimated by normalizing the impact force by the head mass, which agrees with the method used in the cadaver experiment [119]. Specifically, our setup (Figure 3.2) consisted of a monorail drop tower, a gimbal assembly, an impact plate, a load cell, an anvil, a cushion foam, and data acquisition hardware and software. The thickness of the aluminum plate (3/4 inch) was the same as that used in the cadaver experiment. The headform was held by the gimbal before the test. After releasing the gimbal, the headform dropped with the gimbal until the surrogate impacted the plate. The gimbal was then dropped onto the 15 cm thick polyurethane cushion foam on the ground. The foam thickness was selected to mitigate the impact force on the gimbal to avoid damage to the gimbal.

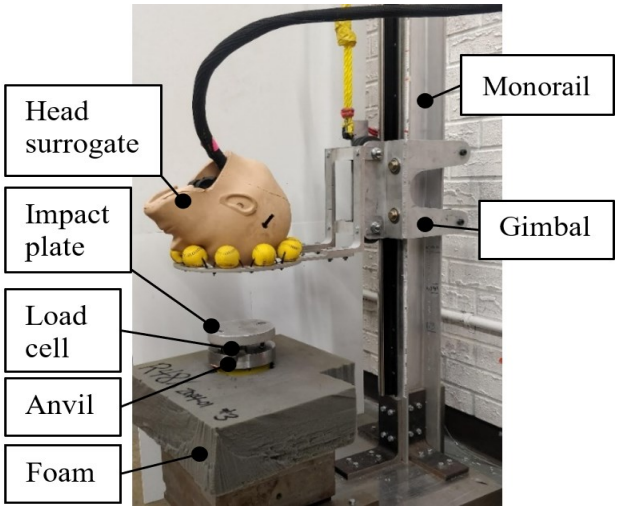

Figure 3.2. Headform positioned within the experimental setup that consisted of the drop tower, gimbal assembly, impact plate, load cell, anvil, and cushion foam.

A load cell (PCB 208C05, PCB Piezotronics Inc., NY United States) which can measure forces up to 22.24 kN, was installed at the center of the cylindrical anvil to quantify the impact force. The impact plate was placed on top of the load cell. Two bearings on the plate were aligned with two shafts that were vertically fixed to the anvil to constrain the linear motion of the plate. Additionally, a laser sensor was mounted on the monorail to measure the impact velocity. IPP signals were filtered with a hardware anti-aliasing filter with a cut-off frequency of 4 kHz. The impact velocity, impact force, and IPP measurements were acquired synchronously at a rate of 25 kHz and saved via LabVIEW (National Instruments, TX United States).

A 5 kg spherical impactor was used to verify the accuracy and repeatability of the force measurements. A polyurethane film of 3 mm thickness and 70 Shore A hardness was attached to the contact surface of the metal impactor to simulate the friction effect of the head scalp. A single-axis linear piezoresistive accelerometer (Xiamen Niell, Model CAYZ147V-2-2KA, China) installed at the center of the impactor measured the linear acceleration along the impact direction. Ten drops from a 7 cm height were performed. The accelerations (160 ± 3.35 g) calculated from the load cell force were within the range that the human head would experience during the drop experiment [119]. The acceleration magnitudes calculated from the load cell were within 1% of those measured by the accelerometer. Additionally, the low COV of the force peaks (2.1%) further indicated the instrumentation repeatability.

3.2.3 Drop Test Configuration

In the first series of tests, the BIPED and Hybrid III were impacted by adjusting the impact velocities and positions to the same as those in the reference cadaver experiment [119].

Each headform was impacted at four locations in the following order: front, left parietal, right parietal, and vertex (Figure 3.3). Referring to the coordinate system at the center of the neck mounting surface (12.5 mm to the Frankfort plane), the impact location coordinates (units: mm) for the front, left, right, and vertex were (68.8, 0, 132), (-13, 72.4, 132), (-13, -72.4, 132), and (0, 0, 157), respectively (Figure 3.3).

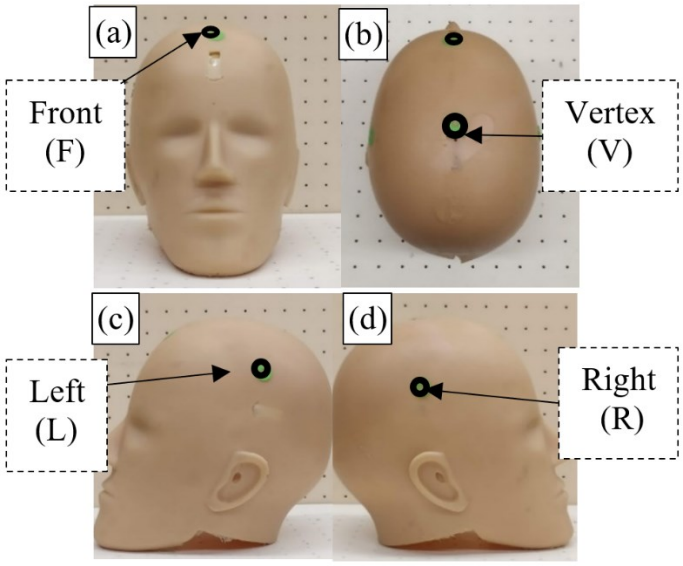

Figure 3.3. locations at the front (a), vertex (b), left parietal (c), and right parietal (d) regions, with the black markers representing the contact sites. Referring to the coordinate system shown in Figure 3.1, the impact location coordinates (unit: mm) for the front, left, right, and vertex were (68.8, 0, 132), (-13, 72.4, 132), (-13, -72.4, 132), and (0, 0, 157), respectively.

The reference cadaver experiment performed free fall drops from 15 and 30 cm, which are equivalent to impact velocities of approximately 1.72 and 2.43 m/s, respectively [119]. In our setup, friction occurred between the gimbal rollers and the rail. To account for the friction, the headform drops were set to generate impact velocities consistent with the impact velocities

in cadaver head drops. As a result, the headform was dropped from a low height of 18.5 cm and a high height of 39 cm for each impact location [119]. All the low height tests were performed first, and five drops were repeated for each impact scenario.

In the second series of tests, the BIPED and Hybrid III were dropped on the front at five different heights with five repetitions for each height. The first height was 10 cm while the subsequent heights increased with 5 cm increments until 30 cm. The data from the previous front drops with 18.5 cm and 39 cm heights were pooled in the data in these series of tests for data analysis. Higher levels of height were not adopted to maintain the integrity of the head for future investigations. This series allowed for a comparison of accelerations between the two headforms as drop height increased, considering that the Hybrid III acceleration peaks have been validated for frontal impacts [130]. To address the friction, all impact heights were transformed to equivalent free fall (EFF) height h_e using the impact velocity v ($h_e = \frac{v^2}{2g}$) for data analysis.

3.2.4 Data Processing and Analysis

3.2.4.1 Data Pre-Processing

Data were processed and analyzed using MATLAB R2019b (MathWorks, MA United States) and CORA release 3.6.1 (pdh, Gaimersheim, Germany). The raw data were filtered using a 4th order low-pass Butterworth filter based on the SAE J211b Class 1000 filter specifications [132]. The peaks and pulse durations of the linear accelerations and IPP were obtained from the time series data. Pulse durations of the accelerations were defined as the period for which the acceleration was above 0.1% of its peak [133]. The duration of the IPP was defined as the period above 20% of its peak based on a previous ICP study [134]. This

was done since some IPP signals failed to drop to 0.1% of their peaks during the first major impulse.

This work mainly compared the BIPED data to the cadaveric data from Loyd and colleagues' drop experiments with six adult cadaver heads [133]. Since the masses of the cadaver heads (3.08–3.45 kg), BIPED (3.85 kg), and Hybrid III headform (4.65 kg) were not consistent, the acceleration data were mass-scaled to the equivalent responses of the 50th percentile male (4.5 kg) for the biofidelity evaluation, based on a previously documented scaling law [135], [136]. Data for repeatability evaluation were not mass-scaled to preserve the original measurement.

3.2.4.2 Acceleration Biofidelity

Statistical tests and analyses were performed to compare the BIPED global accelerations with those of the cadaver subjects and Hybrid III headform. For the first series of tests, the student's *t*-test and Welch's *t*-test were selected when the assumption of normal distributions was validated; otherwise, the Mann-Whitney *U* test was used [137]. The normality of the samples was verified by the Shapiro-Wilk test, and the equality of variances was assessed by Levene's test [137]. For the second series of impacts, an analysis of covariance (ANCOVA) was used to compare the global head accelerations of the BIPED with those of the Hybrid III for front impact [138].

CORA was used to quantitatively assess the level of biofidelity for the time series since the CORA method evaluates signals in comprehensive aspects. Developed by Gehre et al., CORA is a rating method that calculates the level of agreement between time series [100]. It characterizes the time series from two perspectives: the cross-correlation and the corridor.

Cross-correlation considers the signal shape, size, and phase. The cross-correlation (CC) rating is defined as the weighted sum of the shape rating (50%), size rating (25%), and phase rating (25%), as default by CORA [100]. The corridor evaluates the agreement of the time series with corridors, which is a range of the data points along with the time series. It specifies two corridors of the reference signal: an inner corridor and an outer corridor. Its rating is calculated based on the corridor width and the distance between the testing and reference signals. For example, the corridor rating is "0" when the testing signal is beyond the outer corridor, and the rating is "1" when the testing signal is within the inner corridor [100]. The total rating is defined as 50% of the corridor rating plus 50% of the CC [100]. A rating of "0" indicates that the testing signal matches poorly with the reference signal, and a rating of "1" represents a perfect match. Biofidelity classification via the CORA numerical ratings refers to several international standards as possible alternatives [96], [97]. Gehre and colleagues suggest CORA meeting or exceeding 0.7 for good biofidelity [101], but acknowledge that other definitions are possible.

The average time series of repeated tests from the BIPED and Hybrid III were compared to the average cadaver time series. All parameters in the CORA method were set at their defaults, except the corridor widths and phase intervals, which were selected based on the assumption that a poor headform (rating = "0") can distinguish an injury risk of 40% from 60%. For example, the global linear accelerations required for 40% and 60% risk of concussion are about 74 and 88 g from Pellman et al. with a difference of 16% (14 g) of the 88 g. Thus, the acceleration difference between a poor headform and a cadaveric head should be less than 16% of the cadaveric data [139]. Based on this assumption, the inner corridor width was set at one standard deviation of the cadaver time series, and the outer corridor width was one standard

deviation plus 15% of acceleration peaks instead of the default 50% of the peaks. Similarly, conservative boundaries of 2% and 20% were chosen as the low and high phase intervals.

3.2.4.3 Impact Stiffness

Head impact stiffness during the loading period was estimated to explore the mechanical properties that may affect impact responses. Head displacement was obtained through the double time integral of the average acceleration time series. Impact stiffness was then calculated by linearly fitting the force-displacement curves for each impact scenario. The region of the curve chosen to perform the linear fitting was based on previous work [119].

3.2.4.4 Pressure Analysis and Comparison

Similar to a cadaveric study, the BIPED IPP measures were associated with the accelerations via linear regression to evaluate the relationship between them [108]. The pressure was only qualitatively compared to that of cadaveric data from Nahum et al. and Hardy et al. [108], [134], due to the differences in the impact conditions considered in their respective experiments.

3.2.4.5 Repeatability of Acceleration and IPP Measurements

The average (Ave.), standard deviation (Std.), and COV of the peaks and pulse durations of the measurements were calculated for the first test series to evaluate their repeatability. Based on the ISO/WD 15830 document, the repeatability is regarded as excellent when the COV is $\leq 3\%$, whereas a COV $> 10\%$ is considered to be poor or unacceptable [97].

3.3 Results

3.3.1 Comparison of Accelerations

Typical acceleration time histories for the cadaver, BIPED, and Hybrid III for the different impact locations are displayed in Figure 3.4 The acceleration peaks and pulse durations for the three head types, and the relative differences and p-values for the statistic tests between head types are tabulated in Table 3.2 and Table 3.3. Figure 3.5 and Figure 3.6 show the averages and standard deviations for the acceleration peaks and pulse durations for the three head types. Additionally, Figure 3.7 compares the association of acceleration peaks and pulse durations with EFF height for the BIPED and Hybrid III, and Table 3.4 reports the mean and standard deviations for each impact height.

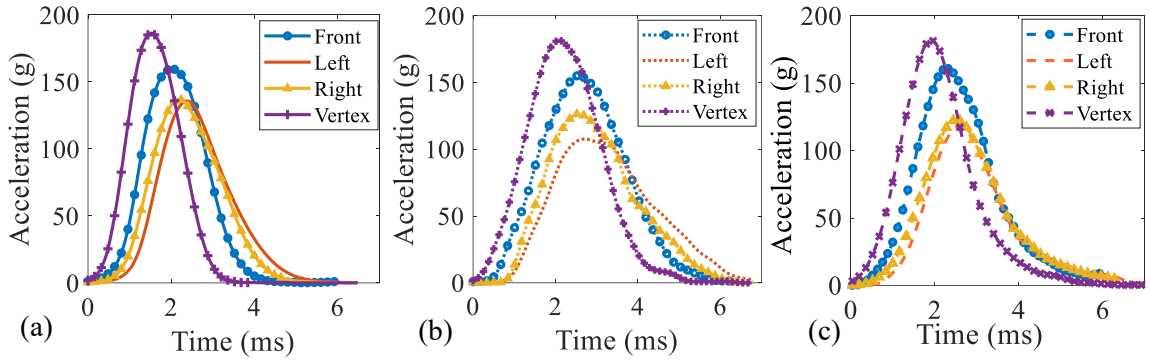

Figure 3.4. Average acceleration plots of the cadaver heads (a), BIPED (b), and Hybrid III (c) for the four different impact locations from high height drops. Plots in (a) were created by mass scaling and then taking the average of all cadaveric data from a doctoral dissertation [133], with the author's permission.

Peak accelerations were greatest for vertex head impacts followed by front, right parietal, and then left parietal for the three head types (Figure 3.4). Vertex impacts were

characterized by higher and narrower acceleration profiles than the front impacts, while the side impacts exhibited the lowest peaks and greatest pulse durations. The acceleration magnitudes for the right impact were 3.5 to 6.9% greater than for the left impact, possibly due to the variation of head positions upon impact.

The majority of BIPED acceleration peaks were not significantly different from cadaver accelerations ($p>0.05$) except for a few low height drops, whereas the BIPED pulse durations were generally greater than the cadaver durations ($p<0.01$). Although the average acceleration peaks of the BIPED were 4.9 to 31.6% lower than for cadaver heads, the difference was not statistically significant for most impacts (Table 3.2). The front impact resulted in the lowest acceleration peak difference from cadaveric data (4.9 and 9.6%) compared to impacts at other locations for the low and high height impacts. Significant differences were only observed in low height impacts at the left, right, and vertex locations, for which the acceleration peaks were respectively 23.4%, 20.6%, and 31.6% lower than in the cadaver experiments. This difference may be attributed to the difference in local material response or improper fit of the scalp on the skull of the BIPED. Similarly, the Hybrid III acceleration peaks were also lower (3.5 to 25.3%) than for the cadaveric data, but the difference was generally not statistically significant. However, the pulse durations of the two headforms were all significantly greater than the cadaveric data ($p<0.01$). Compared to cadaveric data, the relative duration differences for the BIPED and Hybrid III were 23.5 to 107.7% and 19 to 61.2%, respectively (Table 3.3). The BIPED pulse durations were 48.5 % greater than the cadaveric data on average.

Table 3.2. Mass-scaled acceleration peaks (unit: g or 9.8 m/s^2) of cadaver heads, Hybrid III, and BIPED, with averages (Ave.), standard deviations (Std.), and relative difference of the averages between the head types. Diff B&C ((*B*-*C*)/*C*), Diff H&C ((*H*-*C*)/*H*), and Diff B&H ((*B*-*H*)/*H*) represent the relative difference between the BIPED (*B*) and cadaver heads (*C*), Hybrid III (*H*) and cadaver heads, and BIPED and Hybrid III, respectively. F_low, and F_high columns represent low and high height impacts at the front, and L, R, and V represent impacts at the left, right, and vertex. Cadaveric data were mass-scaled to account for differences in cadaver head mass, relative to the BIPED and Hybrid III and were created with the author's permission from a doctoral dissertation [133].

Cadaver	F_low	F_high	L_low	L_high	R_low	R_high	V_low	V_high
Ave.	102.4	161.6	98.1	139.5	98.0	137.5	128.5	191.3
Std.	17.5	25.9	13.6	32.3	15.2	11.7	8.9	21.4
BIPED								
Trial 1	93.9	153.6	81.2	111.7	80.7	121.8	80.1	189.8
Trial 2	94.2	150.9	76.2	108.8	78.8	111.0	87.9	173.7
Trial 3	90.6	157.4	68.6	131.6	78.5	122.0	86.1	-
Trial 4	90.8	155.0	75.5	114.2	77.1	136.2	97.5	-
Trial 5	93.6	152.0	74.4	116.4	74.4	135.2	88.1	-
Ave.	92.6	153.8	75.2	116.5	77.9	125.2	87.9	181.7
Std.	1.8	2.5	4.5	8.9	2.3	10.6	6.2	11.4
Hybrid III								
Trial 1	94.3	151.9	75.4	100.1	69.9	114.7	112.9	192.4
Trial 2	106.2	144.2	81.2	126.0	73.1	121.8	128.5	195.5
Trial 3	92.6	166.7	78.7	119.6	81.4	124.2	100.9	189.9
Trial 4	102.8	152.6	64.0	113.0	74.0	123.7	125.6	179.0
Trial 5	98.3	166.9	67.1	115.9	76.5	112.7	120.5	189.9
Ave.	98.9	156.5	73.3	114.9	75.0	119.4	117.7	189.3
Std.	5.7	10.0	7.4	9.6	4.3	5.4	11.1	6.2
Diff B&C	-9.6%	-4.9%	-23.4%	-16.5%	-20.6%	-8.9%	-31.6%	-5.0%
***p* value**	0.230	0.493	0.006	0.147	0.014	0.104	0.000[a]	0.400
Diff H&C	-3.5%	-3.2%	-25.3%	-17.7%	-23.5%	-13.2%	-8.5%	-1.0%
***p* value**	0.676	0.687	0.005	0.126	0.006	0.011	0.103	0.833
Diff B&H	-6.3%	-1.7%	2.6%	1.4%	3.9%	4.9%	-25.3%	-4.0%
***p* value**	0.069	0.586	0.637	0.787	0.220	0.302	0.001	0.140

Note: a. 0.000 represents $p<0.0005$

Table 3.3. Mass-scaled acceleration durations (unit: ms) of the cadaver heads, Hybrid III, and BIPED, with averages (Ave.), standard deviations (Std.), relative difference, *p* values between the BIPED and cadaver heads (B&C), Hybrid III and cadaver heads (H&C), and BIPED and Hybrid III (B&H) for each scenario. Cadaveric data were mass-scaled to account for differences in cadaver head mass, relative to the BIPED and Hybrid III and were created with author permission from a doctoral dissertation [133].

Cadaver	F_low	F_high	L_low	L_high	R_low	R_high	V_low	V_high
Ave.	4.7	4.5	5.4	5.3	4.6	4.9	4.0	3.9
Std.	0.9	1.1	1.2	0.7	0.8	0.5	0.4	0.3
BIPED								
Trial 1	7.1	6.4	7.8	7.0	7.2	6.0	8.6	6.3
Trial 2	7.2	6.8	7.5	6.3	6.5	6.4	8.6	5.8
Trial 3	7.1	6.4	7.5	6.7	6.2	6.1	8.6	-
Trial 4	7.0	6.1	7.9	6.3	6.4	6.0	8.3	-
Trial 5	7.1	6.0	7.0	6.6	7.0	5.9	8.0	-
Ave.	7.1	6.4	7.5	6.6	6.7	6.1	8.4	6.1
Std.	0.0	0.3	0.4	0.3	0.4	0.2	0.3	0.4
Hybrid III								
Trial 1	7.6	6.4	7.0	7.1	7.3	6.8	6.7	5.7
Trial 2	6.9	6.2	7.2	6.2	7.7	6.8	6.0	5.5
Trial 3	7.7	6.2	7.7	6.4	7.1	6.7	7.5	5.5
Trial 4	7.7	6.6	7.5	6.5	7.7	7.6	5.0	5.6
Trial 5	7.9	6.4	8.0	6.0	7.3	6.8	6.2	5.5
Ave.	7.4	6.3	7.4	6.4	7.3	6.9	6.2	5.5
Std.	0.4	0.2	0.4	0.4	0.3	0.4	0.9	0.1
Diff B&C	51.1%	40.2%	39.8%	23.7%	46.2%	23.5%	107.7%	56.0%
***p* value**	0.000[a]	0.005	0.005	0.004	0.000	0.001	0.000	0.000
Diff H&C	58.5%	38.2%	36.9%	19.5%	61.2%	39.6%	53.4%	40.5%
***p* value**	0.000	0.004	0.006	0.011	0.000	0.000	0.000	0.000
Diff B&H	-4.7%	1.4%	2.1%	3.5%	-9.3%	-11.5%	35.4%	11.0%
***p* value**	0.034	0.751	0.788	0.577	0.008	0.002	0.001	0.001

Note: a. 0.000 represents $p<0.0005$

When comparing the BIPED with the Hybrid III, acceleration peaks had no significant difference for most impacts ($p>0.05$), except for the vertex impact ($p=0.001$) from the low height (Figure 3.5). The acceleration duration for the BIPED was generally lower than for the Hybrid III ($p<0.05$), but the relative difference between the BIPED and Hybrid III

(-3.5 ± 14.8%) was smaller than that between the BIPED and cadavers (48.5 ± 26.6%). When comparing the accelerations from the series of front impacts, results showed differences for both the acceleration peaks and durations (p<0.05) (Figure 3.7 and Table 3.4). Nevertheless, no significant difference was found for the effect of impact height on the peaks (p=0.37) and durations (p=0.89) between the two headforms.

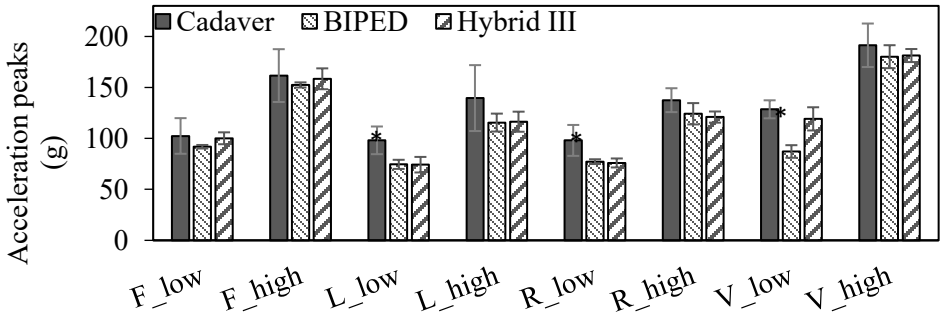

Figure 3.5. Average acceleration peaks with one standard deviation of the cadaver heads, BIPED, and Hybrid III from impacts at four locations (front, left, right, and vertex) and two heights. * Indicates a significant difference between the BIPED and cadaveric data. Cadaveric data were mass-scaled to account for differences in cadaver head mass relative to the BIPED and Hybrid III and were created with author permission from a doctoral dissertation [133].

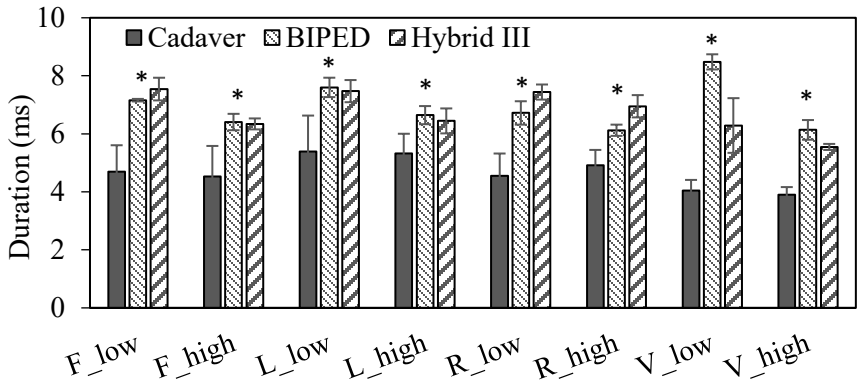

Figure 3.6. Average acceleration durations with one standard deviation of the cadaver heads, BIPED, and Hybrid III from impacts at four locations (front, left, right, and vertex) and two heights. * Indicates a significant difference between the BIPED and cadaveric data. Cadaveric data were mass-scaled to account for differences in cadaver head mass relative to the BIPED and Hybrid III and were created with author permission from a doctoral dissertation [133].

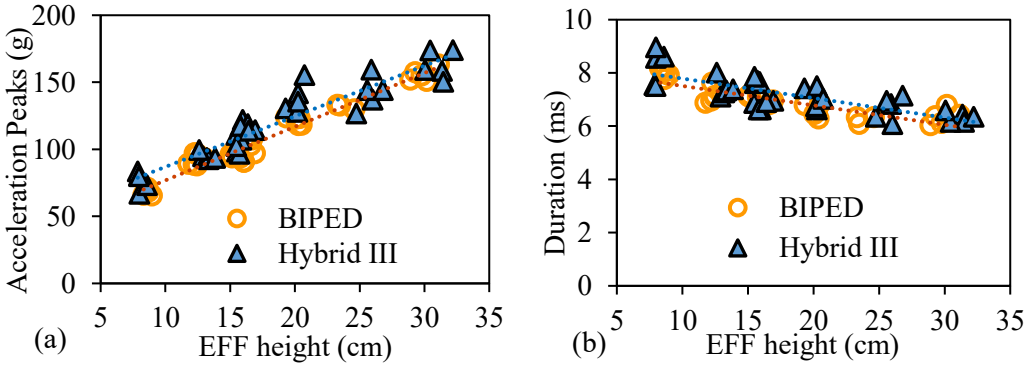

Figure 3.7. The acceleration peaks (a) and pulse durations (b) in dependence of equivalent free fall (EFF) height for the BIPED and Hybrid III during front impacts.

Table 3.4. Acceleration peaks and durations for the BIPED and Hybrid III front impact. The averages and standard deviations (in brackets) of the peaks, durations, and equivalent free fall (EFF) height are tabulated for drops from 10 to 30 cm plus the 18.5 cm and 39 cm heights.

Nominal drop height (cm)	10	15	18.5	20	25	30	39
BIPED EFF height (cm)	8.1 (0.3)	13.2 (0.3)	15.6 (0.2)	16.3 (0.4)	20.1 (0.5)	25.8 (0.7)	30.8 (0.7)
BIPED acceleration peaks (g)	68.3 (2.5)	91.2 (3.9)	92.6 (1.8)	101.5 (6.0)	115.7 (11.2)	136.5 (15.3)	153.8 (2.5)
BIPED acceleration durations (ms)	8.0 (0.2)	7.2 (0.3)	7.1 (0.0)	6.9 (0.1)	6.7 (0.3)	6.4 (0.3)	6.4 (0.3)
Hybrid III EFF height (cm)	8.6 (0.2)	12.3 (0.4)	15.0 (1.5)	16.4 (0.5)	19.3 (2.4)	24.4 (4.3)	29.5 (0.5)
Hybrid III acceleration peaks (g)	76.7 (6.7)	94.7 (2.7)	98.9 (5.7)	117.3 (3.4)	136.2 (10.9)	142.3 (12.0)	156.5 (10)
Hybrid III acceleration durations (ms)	8.2 (0.7)	7.4 (0.3)	7.4 (0.4)	6.8 (0.2)	7.1 (0.4)	6.7 (0.4)	6.3 (0.2)

3.3.2 Acceleration CORA Ratings

Table 3.5 presents the CORA sub-ratings and total ratings of the BIPED and Hybrid III, and Figure 3.8 illustrates the ratings of the BIPED for each impact scenario. The total ratings of the BIPED (0.50 to 0.61) were generally close to those of the Hybrid III (0.51 to 0.77). The CC ratings for the BIPED were relatively high (0.74 to 0.85), and over twice as high as the corridor ratings (0.26 to 0.47) for all impact scenarios. Like the BIPED, the CC ratings of the Hybrid III (0.80 to 0.91) were greater than the corridor ratings (0.24 to 0.76). Note that the total ratings varied with impact location. Except for the left impact, the total ratings for the Hybrid III and BIPED all exceeded or met 0.50 but were below 0.7.

Table 3.5. CORA ratings of BIPED and Hybrid III accelerations relative to cadaver heads for each impact scenario. Cross-correlation rating (CC) is a sum of weighted shape, size, and phase ratings. The total rating is a sum of 25.0% shape rating, 12.5% size rating, 12.5% phase rating, and 50% corridor rating. Impact scenarios include front, left, right, and vertex impacts at the low and high heights.

Scenario	Subject	Shape	Size	Phase	CC	Corridor	Total
		25.0%	12.5%	12.5%	--	50.0%	
F_low	BIPED	0.84	0.90	0.49	0.77	0.30	0.54
	Hybrid III	0.88	0.87	0.49	0.78	0.25	0.51
F_high	BIPED	0.84	0.82	0.56	0.77	0.38	0.58
	Hybrid III	0.96	0.92	0.68	0.88	0.47	0.68
L_low	BIPED	0.80	0.98	0.76	0.84	0.38	0.61
	Hybrid III	0.95	0.82	0.91	0.91	0.64	0.77
L_high	BIPED	0.85	0.98	0.60	0.82	0.41	0.61
	Hybrid III	0.99	0.79	0.94	0.93	0.59	0.76
R_low	BIPED	0.75	0.89	0.94	0.83	0.31	0.57
	Hybrid III	0.73	0.87	0.94	0.82	0.31	0.56
R_high	BIPED	0.93	0.93	0.62	0.85	0.31	0.58
	Hybrid III	0.98	0.84	0.78	0.90	0.49	0.69
V_low	BIPED	0.68	0.74	0.91	0.75	0.26	0.50
	Hybrid III	0.78	0.98	0.90	0.86	0.24	0.55
V_high	BIPED	0.67	0.80	0.81	0.74	0.30	0.53
	Hybrid III	0.91	0.94	0.81	0.89	0.34	0.62

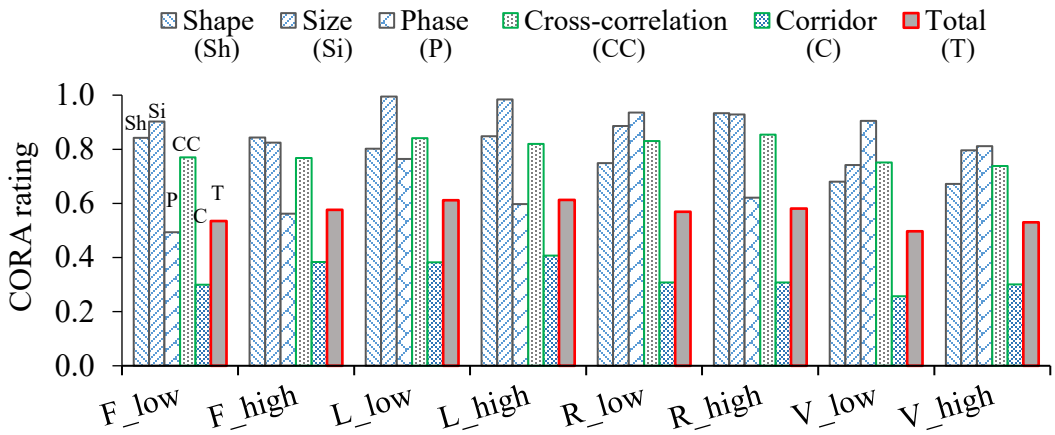

Figure 3.8. CORA ratings of average BIPED acceleration time series relative to the average of cadaveric data for each impact scenario.

3.3.3 Impact Stiffness

Sample plots of the accelerations, force-displacement, and fitting lines for calculating the impact stiffness are displayed in Figure 3.9. Table 3.6 tabulates the impact stiffness of the three head types and the relative difference between head types for each impact scenario. The impact stiffness of the BIPED ranged from 1185 to 2997 N/mm among the different impact scenarios, which was 24 to 53% lower than for the cadaver heads (1973 to 3947 N/mm). The Hybrid III also presented lower stiffness (1476 to 3419 N/mm) compared to the cadaver heads, whereas their relative difference (7 to 35%) was generally lower than the difference between the BIPED and cadaver heads.

Despite the differences, an interesting finding was that the three head types shared similar stiffness variations with impact height and location. As shown in Table 3.6, the impact stiffness increased with impact height for all impact locations. For the same impact location, the acceleration difference between the cadaver and BIPED decreased as the difference in the impact stiffness decreased. Moreover, the vertex impact stiffness was greater than that of the

front and side impacts for the three types of head subjects. These similarities in the stiffness variation with impact location can be attributed to the similar shape and dimensions of the skull and scalp.

Table 3.6. Impact stiffness (units: N/mm) and relative stiffness difference between the head types during the loading period of each impact scenario. Diff B&C ((*SB*-*SC*)/*SC*) represents the stiffness difference between the BIPED (*SB*) and cadaver (*SC*) relative to the cadaver stiffness. Similarly, Diff H&C and Diff B&H represent the relative stiffness differences between the Hybrid III and cadaver heads, and between the BIPED and the Hybrid III. All the stiffnesses were calculated based on the average force and accelerations for each impact scenario. Cadaver stiffnesses were calculated based on the mass-scaled cadaveric data and were created with author permission from a doctoral dissertation [32].

	F_low	F_high	L_low	L_high	R_low	R_high	V_low	V_high
Cadaver	2297	2984	1973	2301	2291	2342	3365	3947
BIPED	1596	2094	1185	1431	1261	1736	1590	2997
Hybrid III	1997	2761	1476	1841	1496	1866	2905	3419
Diff B&C	-31%	-30%	-40%	-38%	-45%	-26%	-53%	-24%
Diff H&C	-13%	-7%	-25%	-20%	-35%	-20%	-14%	-13%
Diff B&H	-20%	-24%	-20%	-22%	-16%	-7%	-45%	-12%

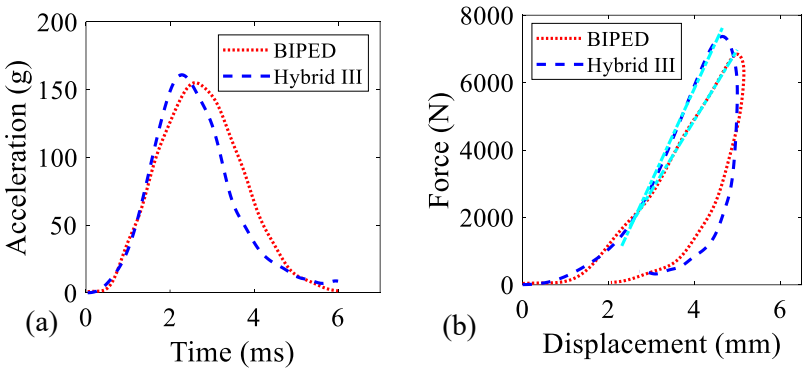

Figure 3.9. Representative plots of the BIPED and Hybrid III showing the average acceleration, force-displacement, and impact stiffness. Displayed is the change of the acceleration with time (a) and the force-displacement relation along with linear fitting lines (cyan color) (b) for front impact from the high height.

3.3.4 Comparison of Pressure

The front, side, and back IPP magnitudes show linear correlations with the head acceleration for the front impact scenario with coefficients of determination, R^2, being 0.88 to 0.99 (Figure 3.10). These highly linear relationships were similar to those in the Nahum et al. cadaveric study that measured the ICP in the CSF, although the linear slopes of the regressions for the BIPED front (1.2 kPa/g), side (0.90 kPa/g), and back (0.39 kPa/g) were higher than those reported by Nahum et al. (0.94, 0.58, 0.23 kPa/g) [108]. In addition, the BIPED front IPP in the brain (82 to 199 kPa) was greater than the side IPP (59 to 150 kPa) while the back IPP (17 to 59 kPa) was the lowest, which was similar to the cadaveric ICP measured in the CSF. However, the back IPP in the BIPED did not experience obvious negative pressures as that in Nahum's experiment with cadaver tests #37, #48, and #49, possibly due to the difference in internal structure, impact mode, and sensor location [108]. Note that The BIPED sensors measured the pressure in the brain while Nahum's cadaveric study measured the pressure in

the CSF, and the range of impact energy in Nahum's study was significantly higher than that of the present study.

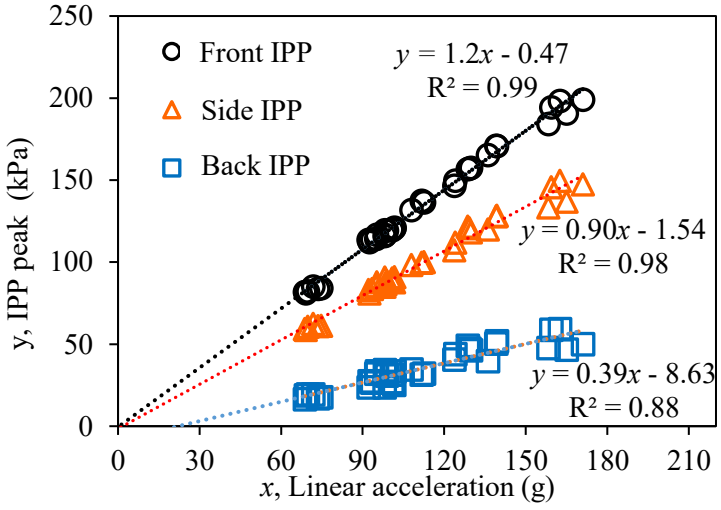

Figure 3.10. BIPED IPP magnitude plotted against global head linear accelerations for front impacts.

3.3.5 Repeatability of Acceleration and IPP Measurements

Representative acceleration and IPP measurements for each impact location are displayed in Figure 3.11 by showing the average and the ±1 standard deviation band of the repeated tests. Maximal standard deviations generally occurred at the peaks. The narrow standard deviation band throughout the time series suggests good repeatability of the measurements.

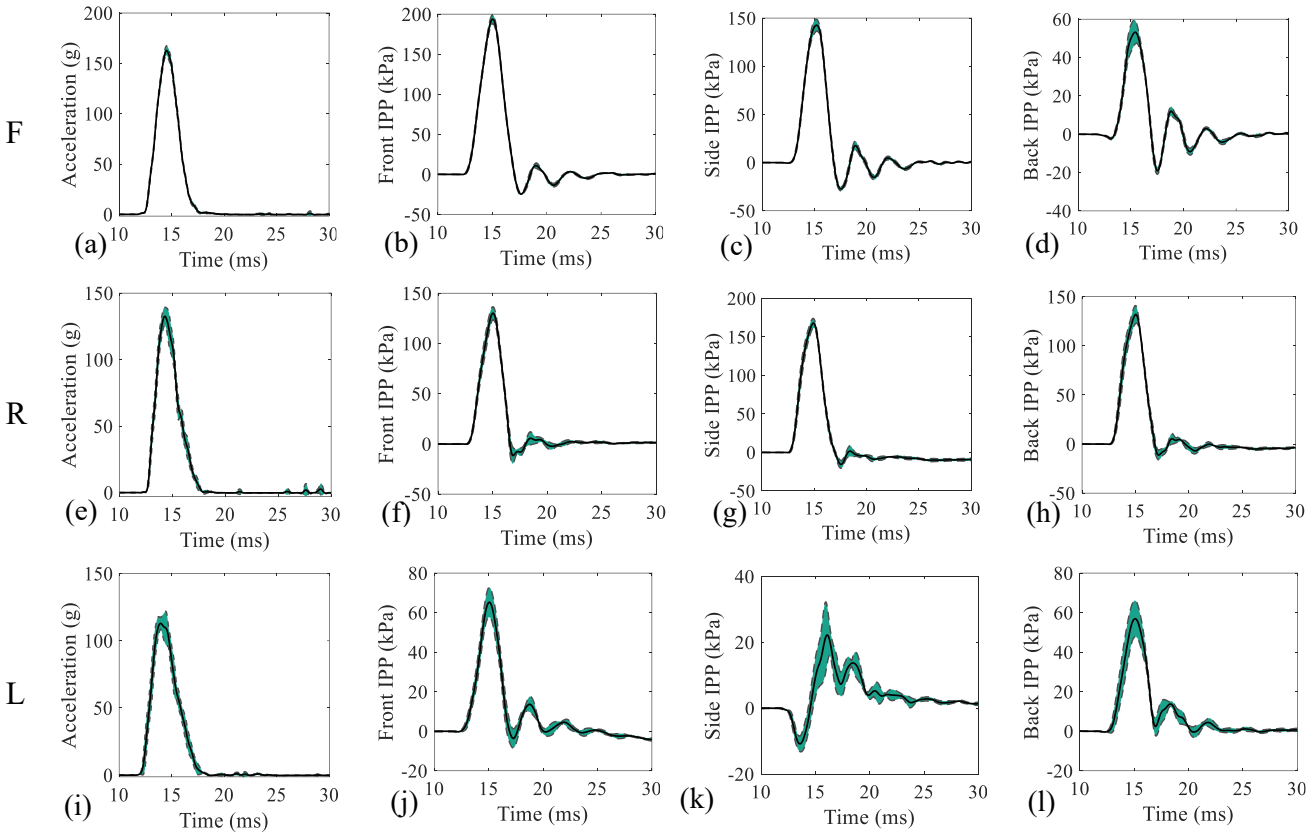

Figure 3.11. Representative plots showing the average measurements of repeated tests with one standard deviation. Linear acceleration, front IPP, side IPP, and back IPP measurements for impact at the front (F), right (R), and left (L) from the high height are displayed.

For the acceleration and IPP peaks and durations, Table 3.7 tabulates their averages (Ave.), standard deviations (Std.), and COV for each impact scenario. The average COV of these measures over different impact scenarios ranged from 2.39 to 9.66%. For the accelerations, the COV of the peaks and durations ranged from 0.65 to 7.61%, except for the peak acceleration (11.24%) of the right, low-height impact. The front impact exhibited the highest level of repeatability with quite low COVs for the acceleration peaks (1.90 and 3.12%), which were categorized as excellent repeatability according to the ISO/WD 15830 standard

[97]. For the IPP, the COV was generally within the level of acceptable repeatability (10%). For some impact scenarios, such as the left impact, the COV was as high as 19.41%, but its standard deviation (5.41 kPa) was in the range of other impacts (1.29 to 18.49 kPa).

Table 3.7. The average (Ave.), standard deviation (Std.), and coefficient of variation (COV) of peak values and durations of the BIPED IPP and accelerations (unscaled). The peaks for the IPP represent the greatest absolute values.

Impact scenario		Velocity	Front IPP		Side IPP		Back IPP		Acceleration	
			Peak	Duration	Peak	Duration	Peak	Duration	Peak	Duration
		[m/s]	[kPa]	[ms]	[kPa]	[ms]	[kPa]	[ms]	[g]	[ms]
F_low	Ave.	1.75	117.35	3.58	87.85	3.28	32.72	2.95	97.15	6.77
	Std.	0.03	2.15	0.02	1.94	0.01	1.29	0.02	1.85	0.04
	COV	**1.49%**	**1.83%**	**0.61%**	**2.21%**	**0.15%**	**3.95%**	**0.61%**	**1.90%**	**0.65%**
F_high	Ave.	2.42	193.40	3.44	142.66	3.17	52.64	2.94	163.28	6.06
	Std.	0.03	6.05	0.08	7.04	0.09	6.08	0.05	5.10	0.28
	COV	**1.43%**	**3.13%**	**2.47%**	**4.94%**	**2.88%**	**11.56%**	**1.55%**	**3.12%**	**4.66%**
L_low	Ave.	1.72	47.68	3.48	15.01	3.21	38.03	3.56	78.86	7.38
	Std.	0.02	4.51	0.12	1.70	0.25	5.11	0.27	4.73	0.53
	COV	**1.30%**	**9.46%**	**3.35%**	**11.33%**	**7.86%**	**13.44%**	**7.68%**	**6.00%**	**7.16%**
L_high	Ave.	2.44	66.95	3.24	27.89	2.58	61.42	3.34	122.24	6.28
	Std.	0.02	6.40	0.12	5.41	0.38	7.92	0.11	9.30	0.31
	COV	**0.77%**	**9.56%**	**3.60%**	**19.41%**	**14.80%**	**12.89%**	**3.34%**	**7.61%**	**4.97%**
R_low	Ave.	1.74	75.55	3.52	97.01	3.79	74.88	3.55	81.68	6.46
	Std.	0.02	4.29	0.09	3.00	0.19	4.07	0.11	2.46	0.40
	COV	**1.40%**	**5.68%**	**2.67%**	**3.09%**	**5.14%**	**5.43%**	**3.12%**	**3.01%**	**6.20%**
R_high	Ave.	2.43	130.34	3.09	168.67	3.27	134.09	3.23	135.09	5.63
	Std.	0.02	7.36	0.04	6.93	0.09	9.20	0.12	8.38	0.19
	COV	**1.00%**	**5.65%**	**1.24%**	**4.11%**	**2.71%**	**6.86%**	**3.83%**	**6.20%**	**3.35%**
V_low	Ave.	1.73	71.61	3.46	67.85	3.48	68.03	4.28	92.38	8.02
	Std.	0.02	5.41	0.06	4.30	0.12	8.91	0.40	6.30	0.26
	COV	**0.95%**	**7.56%**	**1.76%**	**6.34%**	**3.35%**	**13.10%**	**9.42%**	**6.82%**	**3.26%**
V_high	Ave.	2.38	165.88	2.74	146.46	2.68	134.36	2.76	190.59	5.80
	Std.	0.01	13.68	0.08	18.49	0.11	13.67	0.06	11.91	0.34
	COV	**0.55%**	**8.25%**	**3.10%**	**12.63%**	**4.22%**	**10.18%**	**2.05%**	**6.25%**	**5.85%**
Average COV		**1.11%**	**6.39%**	**2.35%**	**8.01%**	**5.14%**	**9.68%**	**3.95%**	**6.14%**	**4.51%**

3.4 Discussion

Instrumented headforms are useful devices in laboratory studies of head injuries compared to human cadaver head subjects and numerical simulations. Human cadavers are good anatomical representations of living humans, but obtaining cadaver specimens is difficult and carries ethical considerations [140]. Installing sensors into cadaver heads is complicated and time-consuming as well. In contrast, numerical simulations are efficient in calculating brain biomechanics and are currently the only method to estimate stress distributions in the brain, but they may have different results depending on the implemented material constitutive models and anatomical assumptions. Researchers may also be forced to model helmets or vehicles to simulate the cases of helmeted head impacts or head impacts in vehicle crashes [141]. Because instrumented headforms allow for physical interactions with the surrounding environment, they are essential for helmet and vehicle crash tests.

Using a novel head-brain model BIPED with built-in instrumentation, this work documents the biofidelity and repeatability of the global head accelerations and the repeatability of the IPP, under direct blunt impact conditions. The overarching findings are that the BIPED yields similar peak kinematics to both historic cadaveric and the Hybrid III blunt impact data and achieves CORA ratings of 0.50 to 0.61. The IPP measures show some trend similarities to selected cadaveric ICP data. In addition, the COV is generally below 10%.

3.4.1 Acceleration Biofidelity

The variation of BIPED global accelerations with impact location demonstrates similar characteristics as the cadaver and Hybrid III data. For all three head types, the vertex impacts exhibit the highest peak accelerations, followed by the front impact and then the side impact

(Table 3.2). Similarly, the signal profiles became broader, and the pulse durations increased with a decrease in the peaks. A possible reason is that the variation of BIPED local stiffness is close to that of cadaver subjects. Indeed, the sequence of impact locations, when ordered from greatest to lowest impact stiffness, is the same as above; Table 3.6 shows that the vertex impact stiffness is the greatest, followed by the front impact and then the side impact stiffness. These similarities in the stiffness variation for the three head types may be due to the similar shapes and dimensions of the skull and scalp. The shape and dimensions of the BIPED and Hybrid III were based on the 50^{th} percentile male head, and the cadaver head subjects were all male. Thus, similar structures result in similar stiffness variations along the surface of the head.

The BIPED exhibited acceleration magnitudes that are comparable to those of the cadaver heads for the same impact scenario. The BIPED peak accelerations had no significant differences (p>0.05) with the cadaveric data for most impact scenarios. Although BIPED average peak accelerations were generally lower than the cadaver peaks (Table 3.2), the statistical analyses showed no significant differences (p>0.05) because the cadaveric data had fairly large variances (COV ranges from 7 to 23%). Some of the low height impacts exhibited greater differences, but the difference decreased with increasing impact height. This result may be due to the different loading rate sensitivities between the biological materials and the simulants. When the impact velocity increased, the relative stiffness difference decreased (Table 3.6), resulting in a lower difference in acceleration magnitudes. The greatest difference was observed for the vertex low height impact, with the average of peak accelerations 31.6% lower than for the cadaver head. This difference may be due to an improper fit of the scalp on the skull at the vertex. This influence on the magnitude becomes negligible in impacts with

higher energy. Future work could evaluate the effect of the quality of fit between the BIPED scalp and skull simulants on the impact responses.

BIPED had CORA ratings of 0.50 to 0.61 compared to 0.51 to 0.77 for Hybrid III, and it had a significant pulse duration difference with the cadaver head. Table 3.5 shows that the size and shape contribute greatly to the total ratings. In contrast, the relatively low corridor ratings are likely due to a tendency of significantly longer acceleration durations for the BIPED data compared to the cadaveric data. The Hybrid III data showed similar patterns with low corridor ratings and longer pulse durations than cadaveric data. The longer pulse duration was possibly the result of lower impact stiffness (Table 3.6). Both the BIPED and Hybrid III had lower stiffnesses than the cadaver heads, with the BIPED being the least stiff for most impact scenarios. This finding suggests that increasing the stiffness of the BIPED could lead to improved biofidelity under blunt impact loading conditions.

Various factors, including the shape, dimensions, structure, and material of the skull and scalp, can affect the impact stiffness. The shape and dimensions of the three head types are similar, whereas the structure and material are different. The two halves of the BIPED skull are jointed using silicone glue, and the Hybrid III is an aluminum hollow structure mounted with an occipital cap. In contrast, human skulls contain eight cranial bones that are jointed by sutures. These different connections of structures can affect the deflection of skull shells and result in stiffness variations. The Young's modulus of the Hybrid III aluminum skull is much greater than that of the human cadaver skull (~5.2 GPa) [142]; however, the vinyl scalp of the Hybrid III is much softer than the human scalp. The skull elastic modulus (2.27 GPa) of the BIPED is close to that of the human skull, but the modulus (~1 MPa) of the BIPED scalp is much lower than that of the human scalp (~22.74 MPa) [31]. Thus, the combined scalp and

skull stiffness leads to a lower impact stiffness of the BIPED than that of the cadaver head. Modifying the BIPED scalp and skull simulants to improve the head stiffness in future work may improve the biofidelity of acceleration responses.

3.4.2 Comparison of Pressure

Although the BIPED and cadavers in Nahum's study experience different impact mechanics and use different instrumentation, interesting trends can be noted when comparing BIPED measures to those documented by Nahum as well as other numerical studies. Nahum et al. horizontally impacted the forehead of seated cadaver subjects with an impactor; the head was inclined with the Frankfort plane oriented 45° from the horizontal. The impactor mass ranged from 5.23 to 23.09 kg, and the impact velocity varied from 4.36 to 12.95 m/s, which generated impact energy much greater than in the present study [108]. For both the BIPED and Nahum's cadaver study, the ICP at the front, side, and back had a linear relationship with the global head linear acceleration and the pressure peaks decreased from the impact side to the contrecoup side. Note that Nahum's study measured the ICP in the CSF, but the BIPED measured the pressure in the brain at a distance of about 1 to 2 cm from the brain surface. The depths of the sensing tips relative to the brain surface in the transversal plane for the front, side, and back sensors were 18.7, 8.5, and 14.8 mm, respectively.

Nevertheless, finite element modeling studies demonstrated that pressure decreases from the CSF at the coup side throughout the brain to the CSF at the contrecoup side [143], [144]. For instance, Pearce et al. used numerical models to simulate blunt impacts and to calculate the pressure throughout the CSF and brain. Their study demonstrated that pressure decreased from positive to negative pressure from the impact side to the countercoup side

[144]. Pressure gradients due to the pressure transition have long been assumed to generate injurious shear stresses in the brain, but the mechanism and its application in helmet assessment need further exploration. The BIPED might be capable of further investigating the pressure distributions and gradients generated during direct blunt impacts provided that a correlation between the pressure at a certain brain depth and in the CSF can be established.

A complete assessment of biofidelity would require comparisons with cadaveric data from comparable impact conditions. BIPED pressure magnitudes were greater than the cadaveric ICP in Nahum et al. for the same global head acceleration peaks [108]. Taking the acceleration of 170 g as an example, the frontal IPP measured by the BIPED was 193.4 ± 6.1 kPa compared to 136.3 kPa from the cadaveric ICP-acceleration linear interpolation [108]. For the same acceleration of 170 g, the side IPP from the BIPED was 142.7 ± 7.0 kPa, which was near twice the cadaver side ICP of 79.2 kPa [108]. The different impact modes, which were a vertical impact for the BIPED and a horizontal impact for the cadaver heads, may be responsible for the differences. Hardy et al. launched a human head assembly horizontally toward a block at a velocity of 3.5 ± 0.3 m/s [134]. The impact assembly comprised a human head and a neck assembly; thus, the equivalent impact mass was greater than in the BIPED experiments. They measured coup pressures of 68.1 ± 47.6 kPa and contrecoup pressures of -30.0 ± 41.7 kPa in the brain [134]. These coup measures were lower than the BIPED coup pressure from both the front impact (193.4 ± 6.1 kPa) and right impact (168.7 ± 6.9 kPa) at a velocity of 1.72 m/s [134]. Due to the differences in the impact surfaces between the BIPED experiment (aluminum) and Hardy's cadaveric experiment (acrylic) and the impact modes, it is uncertain whether the BIPED would exhibit higher pressure under the same impact conditions.

The BIPED contrecoup pressure for front impacts did not show obvious negative pressure phases that have been documented in select cadaveric data [108], [134]. This may be because the BIPED back pressure sensor was located in the brain, as opposed to in the CSF as in the cadaveric experiment [108], where the positive pressure propagated from the impact site may have dominated the negative pressure from the contrecoup site. Hardy et al. also inserted pressure sensors into the brain, but the depth of the sensor locations may be different [134]. The surrogate materials of the brain and CSF may also behave differently from the human head. The homogenous and isotropic BIPED brain can contribute to response differences relative to the biological human brain, and the less viscous saline water of BIPED CSF compared to the cadaver CSF may cause less pressure attenuation during the pressure propagation. Moreover, the BIPED brain simulant probably moved to the front before the drop as a result of gravity, since the surrogate head had no brain stem and meninges to maintain its location in the skull. Therefore, the relative motion between the skull and the brain may not have been realistic and this could be a significant limitation to generating negative pressures at the back of the head. Note that, during the left impacts from the low and high heights, the BIPED exhibited a negative contrecoup pressure pulse. For the left impacts, the contrecoup pressure decreased to -4.58 and -11.03 kPa at the beginning and then increased to 15.01 and 27.89 kPa, respectively. This is likely because the tentorium membrane in the sagittal plane of the BIPED brain reduced the brain displacement before the side impact.

In terms of pulse durations, cadaveric data in Hardy et al. varied significantly from 2 to 31 ms for unhelmeted impacts [134], whereas the BIPED IPP duration ranged from 2.8 to 3.8 ms. The impact mode (vertical and horizontal impacts), impact surface material, and the use of a neck may all contribute to the differences. As a result, a complete assessment of the

BIPED pressure biofidelity is impossible with the present study. To further evaluate pressure biofidelity, our next step will be to reproduce impact experiments similar to other cadaver studies that offer the ICP measurements and relocate the pressure sensors to be the same as those in the cadaver experiments.

3.4.3 Repeatability of Acceleration and IPP Measurements

The BIPED demonstrates excellent to marginal repeatability for measuring global accelerations and IPP under different impact scenarios. Figure 3.11 shows that the repeat tests match well with a negligible deviation area. The COVs and standard deviations in Table 3.7 also indicate low variances of the repeated tests. Notably, most of the COV values for the front impacts were below 5%, which is similar to previous research that dropped the BIPED onto a soft surface [111]. The COVs of acceleration and IPP peaks were mostly lower than the COV of durations, indicating that the magnitude is more sensitive to impact variations than the duration components. Results also show that the IPP measures close to the impact site were generally more repeatable than measures at the opposite site (Table 3.7). For example, the COV of the right side IPP was above 10% for the left impact, whereas the same pressure sensor presents a COV of less than 5% for the right impact.

The side IPP magnitude was quite low for left impacts, resulting in a higher COV of the pressure measures than other measures. Note that the side pressure was measured by the sensor at the right. Another possible reason contributing to the variance of the IPP is the head positions. The head leaned against the gimbal to form an angle of approximately 60° to the impact surface during the side impact, which was consistent with the cadaver experiment [119]. Since the head's center of gravity did not vertically align with the point of impact, a slight

variation of head position could lead to great head angular motion, contributing to the pressure variation. Moreover, the lack of attachment points between the brain and the skull may have caused variation in the brain position in the skull. Since the brain simulant was only held in place by the membranes and fluid, it could move relative to the skull after multiple impacts and result in the variation of IPP measures. Recovering the skull-brain position before each test may reduce the pressure measurement inter-test variation. Future development of the BIPED may need to include the brain stem and meninges to reduce the dislocation and reorientation of the brain in the cranial cavity.

3.4.4 Limitations

There are limitations to this investigation of the biofidelity and repeatability of the BIPED. Firstly, we only evaluated the drop impact mode; however, there are many other modes, such as translational impacts, that are relevant to injury incidents. Considering the differences between the human and artificial neck, we chose to compare the neckless head drop experiments. Another limitation is that we only estimated the linear acceleration along the direction of the impact force. We used this method to maintain consistency with the cadaveric study that we mainly compared to [119]. In future work, we may measure more detailed three-dimensional kinematics when comparable cadaveric data become available. Moreover, we only focused on two impact heights and four impact locations. These impacts typically represent moderate and severe head impacts, with the latter potentially causing skull fractures. Therefore, impact conditions that are worth studying fall between these two levels of impact severity. Due to the lack of cadaveric data for other locations such as regions between the front and side, we only evaluated four typical locations. We did not perform the back impact, although there exist cadaveric data for it. A cut at the back of the BIPED scalp, which is needed

for donning the scalp to the head, may result in a direct impact on the skull and cause skull fractures. Finally, for the pressure comparison, the pressure sensor locations, and impact modes were different from the cadaver experiment that provided ICP measurements [108]. The BIPED measured the brain IPP, whereas the compared cadaveric experiment measured the pressure in the CSF [108]. Furthermore, the cadaveric ICP was obtained from a horizontal blow to a seated cadaver body's head in the anterior-posterior direction, whereas the IPP in this study was obtained from vertical drops of the head to a plate on the ground.

3.5 Conclusion

This study evaluated the response characteristics of BIPED focused on the kinematic biofidelity and measurement repeatability, in an attempt to contribute to the development of a comprehensive headform to support research on blunt impact head injuries and protective headwear. The kinematics and IPP measures were repeatable under multiple locations of drop impacts. The BIPED offered global kinematic peaks with no significant difference from the cadaver head, whereas the pulse durations of the BIPED were approximately 50% longer than the cadaveric data on average. The longer acceleration durations may be associated with the lower stiffness of the BIPED. This study is the first that rigorously validated the biofidelity and repeatability when considering multiple aspects of measurements including peaks, durations, and time histories, which can be a reference for the future validation of human surrogates. This study demonstrated that the BIPED has the potential to replicate global head kinematics in blunt impacts. Future work is required to validate the biofidelity of the ICP responses and improve the kinematic biofidelity of the BIPED, particularly considering the longer pulse durations of the linear accelerations.

Chapter 4 Characterization of the ICP Biofidelity and Kinematic and ICP Inter-test Repeatability of the BIPED

Chapter 3 characterized the biofidelity of the kinematics and the repeatability of the IPP and acceleration responses, but the ICP biofidelity requires further investigation. Therefore, Chapter 4 further characterizes the ICP biofidelity, as well as the inter-test repeatability of more comprehensive responses including the linear kinematics, angular kinematics, CSF pressure (CSFP), and IPP. The materials of this chapter have been submitted to the Annals of Biomedical Engineering as an original research article.

4.1 Introduction

Human headforms are important devices used in the study of head injury mechanisms and the development and assessment of protective headwear and vehicle safety devices [11], [103]. Human cadavers and volunteers are the most suitable analogs of living humans in terms of anatomical structures, whereas they have significant limitations related to ethics, limited sample sizes, experimental complexities, low repeatability, and low durability under injurious loads [11], [145]. As a result, various dummy head surrogates, referred to as headforms or Anthropometric Test Device (ATD) heads, have been developed to replicate the human head responses under impact loads [103]. In comparison to organic human heads, headforms have the advantages of being durable, repeatable, and easy to use, and allow for extensive testing and cross-laboratory comparison [11]. With an appropriate storage process, human cadaver heads can be adequate surrogates in the context where the injury outcomes of the head are required for analysis [11]. For questions that can be answered with analysis of the mechanics

or kinematics of the head, headforms are more favorable than cadaver heads due to the aforementioned advantages.

Headforms are generally required to meet minimum levels of biofidelity and have repeatable responses [11], [97]. Biofidelity means that the headform exhibits human-like mechanical responses when subjected to the loading of interest and present human-like external features in order to provide realistic interactions with safety devices such as headgear [11]. As headforms are subjected to regulatory tests, their responses are required to be repeatable in order to provide reliable results [11].

Commercially available headforms are mostly limited to measuring global kinematics or mechanical loads on the skull [103]. These headforms generally attempt to replicate the external dimensions, mass, moment of inertia, and sometimes skull features (e.g., the facial features and cranial structures) of the head to obtain a close representation of the head kinematics or skull mechanics during impact [103]. However, these surrogates are not suitable for measuring or predicting the head intracranial response. Generally, the head dimensions and external features are easier to replicate compared to the complex head features that determine the head intracranial responses. For instance, one of the most widely used headforms, the Hybrid III, consists of a vinyl scalp and a hollow aluminum skull [146]. It is instrumented with accelerometers in the skull to measure the head kinematics. The commonly used FOCUS headform mimics head dimensions, facial features, and skull bone patterns [103]. It has load cells on the skull to measure the impact force. Some headforms for standard helmet tests, such as the EN960 and ISO/DIS 6220 headform, comprise a one-piece human-like skull without a scalp [104]. These headforms have no biofidelic internal components such as the meninges, membranes, cerebrospinal fluid (CSF), or the brain, which are essential to replicating

intracranial responses. Moreover, the materials and thicknesses of the skull shells are not representative of the human skull. To investigate intracranial responses related to brain injuries, studies commonly reconstruct impact accidents with traditional headforms such as the Hybrid III headform to acquire head kinematics [92], [147]. Then, the kinematics serve as input to computational head models to estimate intracranial mechanics [92], [147].

Headforms measuring intracranial responses may improve our understanding of brain injuries as well as the development and application of brain injury criteria. Numerous studies use intracranial responses such as intracranial pressure (ICP), brain strain, and brain stress to indicate the severity of brain injuries, as these parameters are directly related to brain tissue response [13], [65]. Furthermore, injury criteria based on intracranial parameters such as shear strains and stresses are better correlated to traumatic brain injuries, such as diffuse axonal injuries and concussions, than kinematic-based criteria [88], [148]. However, studies of intracranial parameters are mostly limited to the use of computational models and human cadavers because of the lack of physical head models capable of replicating intracranial responses. To our knowledge, among commercially available headforms, only the NOCSAE headform has a brain simulant in the skull hollow to adjust the headform mass [103], [149]. However, the NOCSAE headform is not designed to measure intracranial responses as it has no other basic intracranial components. The development of advanced headforms that can replicate intracranial responses may encourage research on brain injury mechanisms and tissue-level injury criteria.

Only a few headforms have attempted to replicate intracranial responses and their level of biofidelity and repeatability have not been fully validated. Freitas et al. developed a head surrogate using a human cranium and a surrogate brain to study mechanics caused by ballistic

impacts on helmets [17]. Sensors were cast in the brain to measure pressure responses, but the biofidelity and repeatability of the head were not validated against cadaveric data. Additionally, this head surrogate was not aimed for use in multiple experiments as it cannot be reused once the human cranium fractures [150]. A recent study presented an instrumented headform comprised of a deformable skull, silicone brain, CSF surrogate, and rubber skin with frontal and parietal CSFP peaks that were in agreement with cadaveric CSFP peaks reported by Nahum et al., but the kinematic biofidelity and repeatability of the surrogate were not documented [19], [21].

The Blast Injury Protection Evaluation Device (BIPED) is a headform that attempts to replicate the material properties and dimensions of the external and internal components of the human head [16], [22]. The biofidelity of its intra-parenchymal pressure (IPP) has been demonstrated under blast loading conditions, the regime for which the headform was originally developed [131]. Considering its construction, this headform may be of use in blunt impact scenarios after further validation and improvement. Our previous study aiming at evaluating the kinematic biofidelity dropped the headform onto an aluminum plate on the ground at the front, side, and vertex of the head, simulating the cadaveric drop experiment by Loyd et al.[120], [133]. The impact linear acceleration and IPP measurements were deemed to have acceptable repeatability, with coefficients of variation (COVs, i.e., standard deviation divided by the mean) being lower than 10%. The acceleration peaks were not significantly difference from the cadaver data from Loyd et al., whereas the IPP biofidelity lacked evaluation as Loyd et al. did not provide ICP measurements for comparison [120], [133]. Nahum et al. conducted translational impacts on cadaver heads and provided ICP measured in the CSF, which was commonly used to validate numerical and physical head models [108], [151], [19]. However,

the impact angle relative to the head, impact surface, and ICP measurement locations in the BIPED drop experiment were not in line with Nahum's experiment. Since the impact angle and impact surface can affect head impact responses and the ICP varies with locations in the cranium [144], [152], [153], the BIPED ICP biofidelity was not validated in the previous study [120]. Another study conducting blast and drop impact tests with the BIPED found that the IPP responses from the drop tests exhibited similar pulse durations and peaks to reported cadaveric data [111]. However, the study did not quantitatively evaluate the ICP biofidelity due to the lack of cadaveric ICP data from the same loading conditions [111]. Therefore, the biofidelity of BIPED ICP in blunt impact remains unclear, and further investigation of the ICP biofidelity requires matching the loading condition and ICP measurement locations with the compared cadaveric experiments.

Based on the above considerations, the overall objective of this study was to (1) characterize ICP biofidelity by comparing the BIPED CSFP to Nahum's cadaveric CSFP [108], and (2) assess the repeatability of the BIPED CSFP and IPP as well as kinematic responses in the test conditions completed in the current work. This study only adopted frontal impacts of the BIPED with a pendulum impactor due to the lack of cadaveric ICP data from other impact locations for comparison. In this study, CSFP responses from the BIPED were compared to cadaveric CSFP data mainly presented in a previous study by Nahum et al.[108]. The repeatability of the head kinematics and ICP responses was characterized using measurements from repeated tests.

4.2 Materials and Methods

4.2.1 Head Surrogate and Instrumentation

The BIPED comprises a surrogate scalp, two halved skull surrogates, a brain surrogate, a saline water layer serving as the CSF, and tentorium and falx surrogates [22]. The structures of the skull and the brain can be seen in Figure 4.1(a). This study used the original version BIPED mark 1 (mk1) developed for use in blast loading regimes. A BIPED mk2 is currently in development and intends to extend the application of BIPED mk1 to blunt impact scenarios. The BIPED has biofidelic external geometry and facial features based on the ISO size J and Canada standard Association CAN/CSA headforms, respectively [110]. The internal features were based on three-dimensional models of the human skeleton [22]. Three pressure sensors (XCL-072, Kulite Semiconductor Products Inc., NJ United States) were cast in the front, right side, and back of the brain surrogate with an approximate distance of 1 cm to the brain surface. Thus, these sensors measure the IPP at the three locations. Details of the head geometry, materials, and instrumentation location can be found in previous publications [22], [120].

Nahum et al. measured ICP in the CSF, which corresponds with CSFP in the present study [108]. To compare with Nahum's cadaveric data, the present study installed four miniature pressure sensors (MS5407, TE Connectivity Ltd, CA United States) at the front, right side, left side, and back of the upper skull inner surface to measure the CSFP (Figure 4.1(b)). Note that the left CSFP sensor was not used in this experiment due to the lack of a hardware sampling channel. Each pressure sensor was glued to a blind hole on the skull using waterproof epoxy adhesive (J-B weld, TX United States). The miniature sensor cables (diameter = 2 mm) were symmetrically glued to the skull surface and passed out of the skull

at the back (Figure 4.1(b) and (c)) to minimize their interference with the brain and the scalp. The sensing surfaces were flush with the skull's inner surface. The sensor was waterproof and had dimensions of 6.2 by 6.4 by 2.9 mm, thus minimizing its influence on the skull's properties. Aligned to face each other, the CSFP and IPP sensors were in the same horizontal plane 58.2 mm above the Frankfort plane, as shown in Figure 4.1(e) and (f).

Additionally, a kinematic sensor (DTS 6DX PRO, DTS Inc, CA United States) was added to the BIPED to measure linear accelerations (range of the sensor: ±2000 g) and angular rates (range of the sensor: ±8000 degree/second) along all three axes. The sensor was mounted to a custom-designed 3D-printed fixture with mounting screws, and the fixture was tightly mounted to the back surface of the BIPED jaw using a steel bolt of 0.25-inch diameter at the nasal cavity (Figure 4.1(d)). The kinematics coordinate system at the sensor location is shown in Figure 4.1(e). The attaching surface of the fixture was designed to closely fit the curved surface of the jaw to maintain the stability of the sensor position during the impact. A rigid polymer filament acrylonitrile butadiene styrene (hardness: Shore D 100) was selected to print the fixture to minimize the vibration of the fixture that may affect the sensor measurements. The kinematic sensor (mass: 12 grams) and customized fixture (mass: 20 grams) had a negligible effect on the head mass and impact responses due to their relatively small mass.

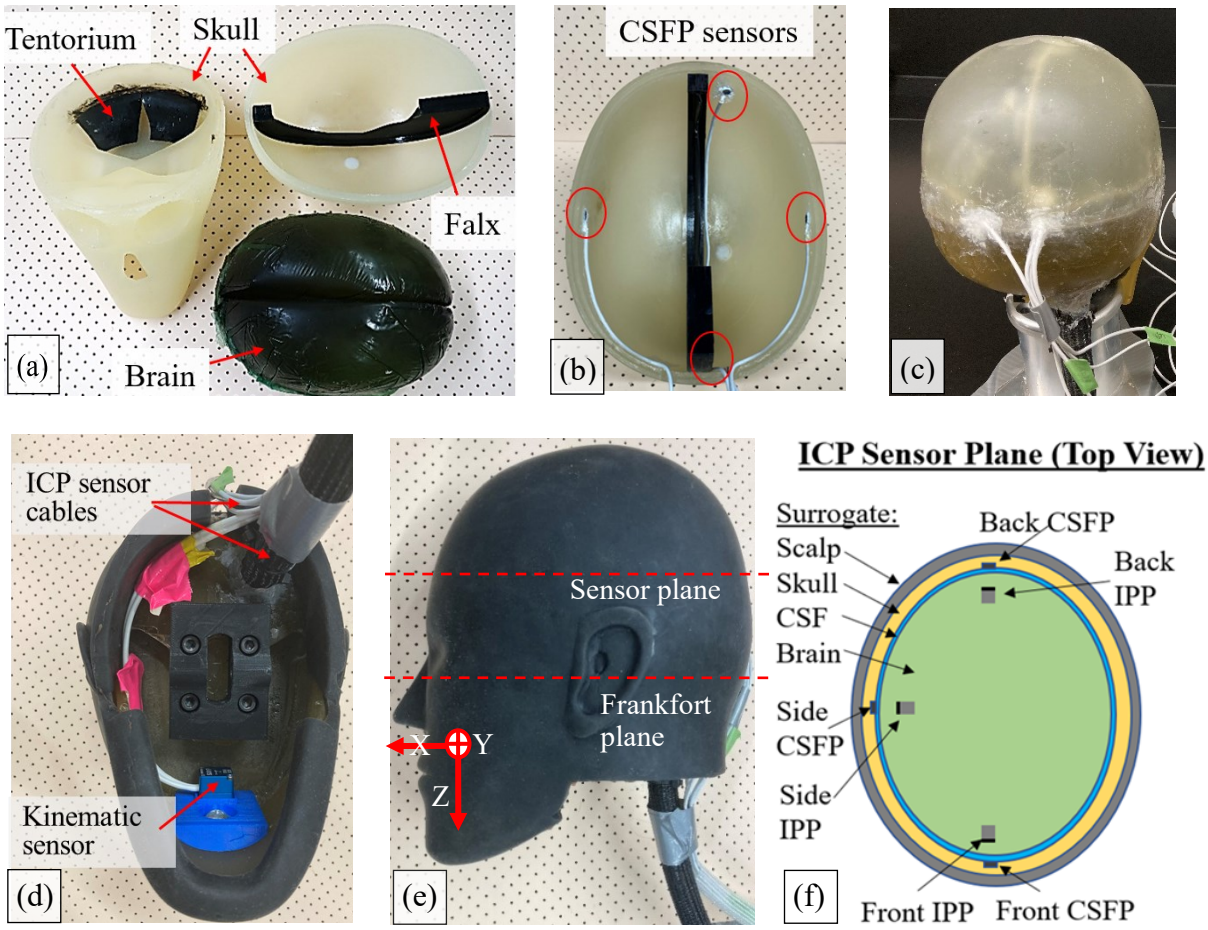

Figure 4.1. (a) Models of the two halved skulls, brain, tentorium, and falx membranes; (b) CSFP sensors installed on the inner skull surface; (c) back view of the assembled skull and brain including the CSFP sensor cables; (d) bottom view of the BIPED showing the kinematic sensor attached to the inner surface of the jaw region with a fixture; (e) side view of the BIPED showing the external features and the location of the sensor plane as well as the kinematic sensor coordinates; (f) schematic of the ICP sensor plane from the top view showing the main components of the BIPED and the CSFP and IPP sensor locations. Abbreviations are defined in the text.

4.2.2 Impact experiment

To compare with Nahum et al.'s cadaver CSFP, the experimental setup was designed to replicate Nahum's experiment as closely as possible [108]. As shown in Figure 4.2(a), The impact rig consists of a rack and pendulum arm with an impactor at the bottom end. The impactor had a 5-inch diameter impact surface, with an effective mass of 5.6 kg, which is close to that used in Nahum's study (5.59 and 5.23 kg) [108]. The BIPED was connected to a male 50th percentile Hybrid III neck with the center area of the forehead contacting the impact surface when the impactor swung to its lowest point. As shown in Figure 4.2(b), the neck was 45° to the horizontal plane such that the Frankfort plane of the head was 135° to the horizontal plane, similar to the setup in Nahum's study [108]. After being positioned, the neck was fixed to a stand assembly that could move along a pair of linear rails on a flat platform.

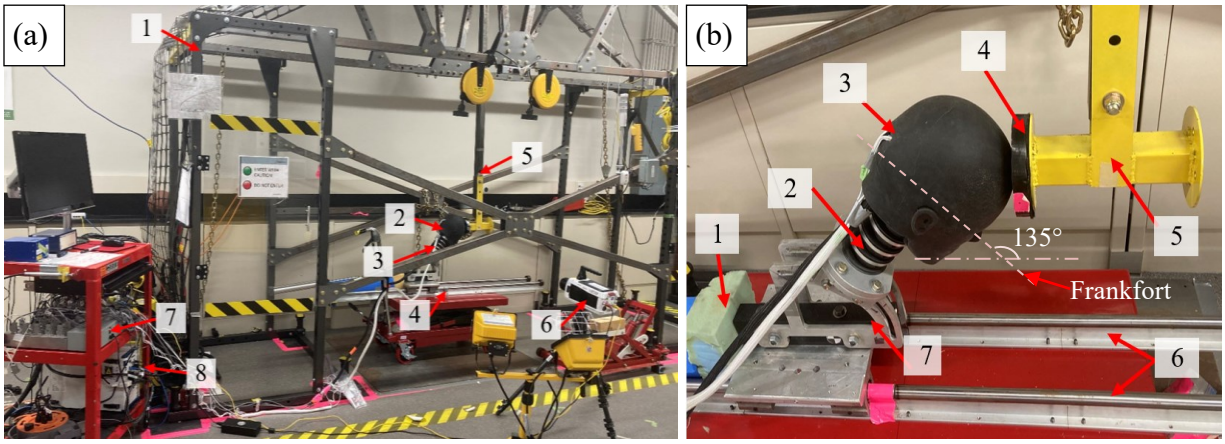

Figure 4.2. (a) Experimental setup showing the rack (1), pendulum arm with an impactor (5), BIPED (2) attached to the Hybrid III neck (3), linear rail (4), high-speed camera (6), amplifier (7) and data acquisition system (8); (b) Detailed view of the BIPED and impactor setup upon impact (1. buffer foam, 2. Hybrid III neck, 3. BIPED, 4. impactor surface, 5. impactor, 6. linear rails, 7. stand assembly).

Using a polyurethane foam between the stand assemble and the end part of the rail, the movement of the stand along the rail was restricted to a limited distance (<10 cm) to simulate the neck movement caused by the movement of the seated cadaver's torso during the impact tests [108]. However, our preliminary tests found that omitting the buffer would not affect the head impact responses, since the impact response occurred more rapidly than the movement of the stand. Nevertheless, the buffer functioned to decelerate and stop the moving stand assembly.

Nahum's study used various impact surfaces but did not report on their nature. Therefore, we evaluated three impact surfaces from soft to hard to cover the possible blunt impact surfaces in civilian life and the military: vinyl nitrile 600 foam (VN600), PMC746, and steel. The VN600 (Shore A 20) and PMC746 urethane pad (Shore A 60), attached to the impactor surface, had thicknesses of 4.5 and 2 cm, respectively. For each impact surface, six impact speeds were evaluated (0.5, 1, 2, 3, 4, and 5 m/s). The steel surface (HV 200) was also evaluated by directly impacting the steel impactor surface at a lower velocity range (0.5, 1, 1.5, 2, 2.5, and 3 m/s) to avoid excessive impact forces and vibrations. The tests for each combination of velocity and impact surface were repeated four times with approximately three minutes between consecutive impacts, allowing for saving the data, checking for CSF leakage as a sign of headform damage, and resetting the position of the pendulum and the headform.

Before the tests, the releasing height of the pendulum impactor for each impact velocity was determined by a calibration experiment with a Phantom v611 high-speed camera (Vision Research, NJ, United States) to measure the impact velocity. The calibration experiment released the pendulum impactor from varied heights, obtaining the relation between the releasing height and the impact velocity.

During the experiments, the pendulum impactor was raised to the predetermined height and was released using a magnetic control system. All measurements, including the three linear accelerations and three angular rates, three CSFPs, and three IPPs, were collected simultaneously using a National Instruments (NI) data acquisition system (NI, TX United States) at a rate of 25 kHz [154]. Before sampling, the analog voltages were amplified and filtered for anti-aliasing using a hardware filter with a cut-off frequency of 4 kHz based on the Society of Automotive Engineers (SAE) Standard J211-1 document [154]. To record the tests and verify the impact velocity, the Phantom v611 high-speed camera was used to capture the impacts at a rate of 3 kHz.

4.2.3 Data Analysis

The kinematics and pressure signals were processed using MATLAB R2020a (MathWorks, MA United States). All the measurements were filtered using a 4^{th} order Butterworth low pass filter with a cut-off frequency of 1650 Hz based on the specifications described in SAE Standard J211-1 [154]. The cut-off frequency based on the SAE standard was lower than the 2400 Hz used in the cadaver study [108], but the difference between the peaks using the two cut-off frequencies was found to be negligible as the measurement frequency contents were well below the cut-off frequency. The COV was used to evaluate the repeatability of the peak linear accelerations, angular rates, and ICPs. COV was calculated as the standard deviation divided by the average of the repeated measurements. Based on the ISO 15830-1 specification, a COV of less than 10% is considered acceptable, a COV between 3–7% is considered good, and a COV of less than 3% is considered excellent repeatability [155]. The COVs of the repeated tests for each impact scenario were evaluated.

The biofidelity evaluation investigated CSFP peaks and time histories. Before the biofidelity evaluation, the kinematic signals were transformed to the mass center of the head based on rigid body motions. Since Nahum's study provided a collective of CSFP data from cadaveric tests, we mainly compared the CSFP with Nahum's study [108]. Nahum et al. provided time histories of CSFP and linear accelerations for test #37 (T.37), as well as CSFP time histories and acceleration peaks for tests #48 (T.48), #49 (T.49), #51 (T.51), and #52 (T.52) [108]. We chose the BIPED tests with impact surfaces resulting in the pulse durations closest to the cadaver tests for comparison, as the close durations indicated similar contact compliance. Consequently, there were two groups for comparison with the cadaver: BIPED impacts with the PMC746 surface at the velocity of 5 m/s were compared to cadaver T.37 and T.48; and BIPED impacts with the steel surface at the velocity of 2 m/s were compared to cadaver T.49, T.51, and T.52 [108].

The selected cadaver tests used impact velocities up to 8–9 m/s [108] whereas the present study used lower impact velocities due to laboratory safety restrictions. Therefore, the accelerations and CSFP for most of the cadaveric tests were greater than in the BIPED experiments. For comparison, the cadaveric CSFP time histories from T.37, T.48, T.49, T.51, and T.52 were scaled equivalently to the BIPED accelerations, based on the linear relationship between the cadaveric ICP and acceleration from Nahum et al.[108]. We assumed that the intercepts of the acceleration-ICP linear equations were zeros since the ICP would be zero when there were no head accelerations in Nahum's experiments. With this assumption and the linear relationship, multiplying the ICP and acceleration with the same ratio would resolve the scaled ICP corresponding to the scaled acceleration regardless of the slopes of the linear equations. The scale method multiplied the CSFP time histories by the ratio of the compared

BIPED and cadaver acceleration peaks, assuming that the intercepts of the cadaver acceleration-CSFP linear relations were zero. This method means that we compared the BIPED CSFP with the scaled cadaveric CSFP on the condition of matching the resultant linear acceleration peaks for the two types of heads. The scaling method is described using the formula below.

$$\boldsymbol{CSFP_{scaled} = CSFP_{cadaver} \times \frac{Acc_{BIPED}}{Acc_{cadaver}}} \qquad \textbf{Equation 4.1}$$

where $CSFP_{scaled}$ is the time histories of cadaver scaled CSFP, $CSFP_{cadaver}$ is the cadaveric CSFP time histories from Nahum et al., and Acc_{BIPED} and $Acc_{cadaver}$ are the resultant linear acceleration peaks for the BIPED and the cadaver tests. We compared the relative difference ($Diff.$) between BIPED pressure peaks and Nahum et al.'s scaled pressure peaks using the formula below.

$$\boldsymbol{Diff.} = \frac{\textbf{BIPED CSFP peak} - \textbf{scaled cadaveric CSFP peak}}{\textbf{scaled cadaveric CSFP peak}} \times \mathbf{100\%} \qquad \textbf{Equation 4.2}$$

The CSFP-acceleration relationship of the BIPED was also assessed in this study using linear regression analysis and was compared to Nahum et al.'s cadaveric study [108]. The article from Nahum et al. provides an image (Fig. 7 in the article) showing the data points of the peak CSFP versus peak linear accelerations for CSFP at the front, parietal, occipital, and posterior fossa locations [108]. They used units of mmHg and m/sec^2 for the pressure and acceleration while we used kPa and g. To be consistent, we extracted the data from their image and converted the cadaveric data to the equivalent measurements of the units in our measurements. Then, we conducted linear regressions of the cadaver front, side, and back CSFP against the accelerations. Note that these cadaveric data were not scaled as the comparison focused on the CSFP-acceleration linear relationship that did not change with the

linear scale. The cadaveric CSFP and acceleration peaks were from the impact of various surfaces and velocities. Thus, the linear regression was performed on the BIPED CSFPs against resultant accelerations for each impact surface as well as pooled data from the three impactor surfaces. Coefficients of determination (R^2) from the regression analysis explained the goodness of linear fit. For each site of CSFP, the student's *t*-test was used to compare the regression slopes between the BIPED pooled data from three impactor surfaces and the unscaled cadaveric data.

The CORrelation and Analysis (CORA) method was used to compare the average CSFP time histories from the BIPED repeated tests with the scaled cadaver CSFP time histories in the two groups of comparisons, namely a comparison of the BIPED test with cadaver T.37 and T.48 and a comparison of the BIPED test with cadaver T.49, T.51, and T.52. In each comparison group, the BIPED CSFP time histories from the four repeated tests were aligned at 0.1% of the peaks (i.e., the assumed starting point of the pulse), and then four CSFPs at each time point were averaged to obtain the average time histories for the CORA analysis. The CSFP time histories CORA evaluated the degree of agreement between time series based on two methods, the cross-correlation of the data sets and the corridor method [100]. The cross-correlation method evaluated the shape, size, and phase shift between the compared time histories, while the corridor method evaluated the distance between the compared profiles relative to the default corridor width. The agreement of each aspect (i.e., the shape, size, phase, and corridor) was quantified mathematically with a rating from "0" to "1", indicating a poor match to a perfect match. The cross-correlation (CC) rating was defined as the weighted sum of the shape (50%), size (25%), and phase (25%) [100]. The total rating was defined as the weighted sum of the corridor rating (50%) and the CC rating (50%).

CORAplus 4.04 (pdh, Gaimersheim, Germany) was used to perform the CORA analysis and all calculations and parameters were set as default. The CORA rating method has been used by several studies to evaluate the biofidelity of physical and numerical head models [127], [156], [157]. There is no agreement on the interpretation of the ratings between "0" and "1". Based on the previous rating of a dummy head, a total rating of 0.7 and higher has been assumed to be an indicator of good biofidelity by some researchers [101].

4.3 Results

4.3.1 Repeatability

Figure 4.3 displays the sample average time series with standard deviation corridors (green color) for the head kinematics including linear accelerations and angular rates in three axes and ICP measurements including CSFP and IPP at the front, right, and back of the BIPED. The nearly invisible area of deviations (in green color) demonstrated the low variance of the repeated measurements. Table 4.1 as well as Table A1 and Table A2 in Appendix provide the average, standard deviation, and COV for the peak kinematics and ICP for tests with the PMC746, VN600, and steel surface, respectively. 82.9% of the COVs for the head kinematics and ICP peaks were below 10%. 72.6% of the COVs were below 7% and 53.2% of the COVs were below the excellent repeatability threshold of 3%. Moreover, the COVs greater than 10% were mostly kinematics and ICP of low magnitudes for which the mean peaks (COV denominator) approached zero (Table 4.1). In these specific cases, the COV should not be directly interpreted as a robust measure of repeatability. Overall, based on ISO 15830-1, the BIPED kinematic and ICP measures generally acceptable repeatability in translational impacts.

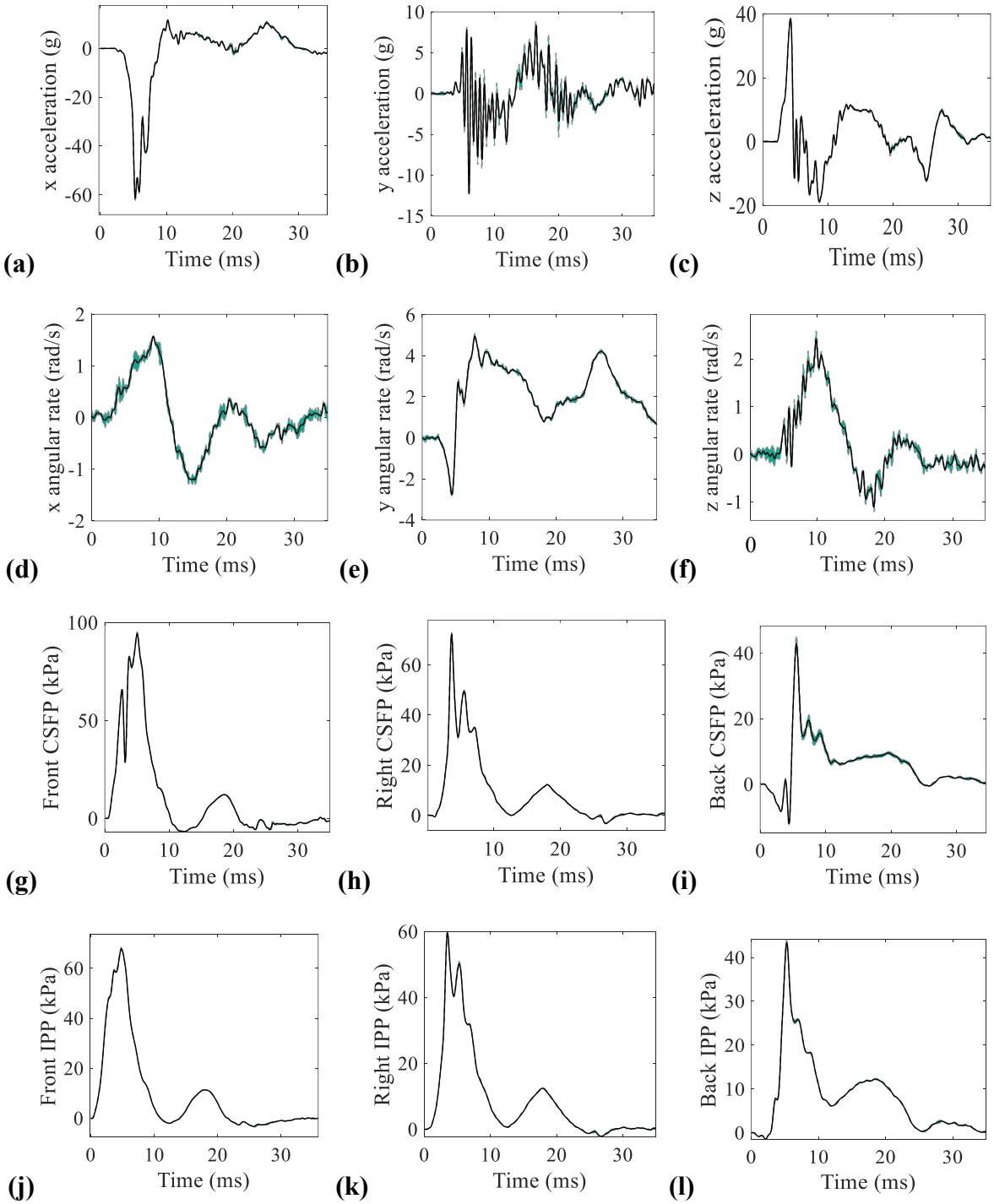

Figure 4.3. Sample repeatability plots from impacts with the PMC746 surface and at the impact velocity of 3 m/s. Plots show the average measurements of repeated tests with one standard deviation for the linear accelerations and angular rates for three axes, as well as CSFP and IPP at the front, right, and back of the BIPED.

Table 4.1. Average (Ave.), standard deviation (Std.), and COV of the measurement peaks including the linear accelerations and angular rates in the XYZ directions, and CSFP and IPP at the front, side, and back of the head. F., S., and B. represent ICP measured at the front, right side, and back. X Acc. and X AnR. means the linear acceleration and angular rate on X-axis. Tabulated are measurements from the impactor surface of the PMC746 pad at an impact velocity V.

V Ave. (Std.) (m/s)		X Acc. (g)	Y Acc. (g)	Z Acc. (g)	X AnR. (rad/s)	Y AnR. (rad/s)	Z AnR. (rad/s)	F. CSFP (kPa)	S. CSFP (kPa)	B. CSFP Max (kPa)	B. CSFP Min (kPa)	F. IPP (kPa)	S. IPP (kPa)	B. IPP Max (kPa)	B. IPP Min (kPa)
0.51 (0.04)	**Ave.**	-2.5	-0.1	1.1	0.3	1.1	-0.2	6.6	3.8	2.7	-0.3	5.2	3.8	2.9	-0.1
	Std.	0.1	0.3	0.1	0.0	0.1	0.3	0.3	0.2	0.1	0.0	0.2	0.1	0.1	0.0
	COV	5.5%	223.3%	8.0%	8.1%	7.5%	198.9%	3.8%	4.2%	2.7%	3.2%	3.6%	3.1%	3.4%	34.8%
0.98 (0.02)	**Ave.**	-6.2	0.0	-2.5	0.0	1.9	0.4	13.1	8.0	4.4	-0.7	10.4	7.9	5.0	-0.2
	Std.	0.1	0.7	0.0	0.4	0.0	0.1	0.1	0.1	0.0	0.0	0.1	0.1	0.1	0.0
	COV	1.2%	5519.0%	1.6%	3555.4%	0.7%	16.6%	0.8%	0.7%	0.9%	3.5%	0.9%	0.8%	1.5%	11.4%
2.08 (0.07)	**Ave.**	-38.3	2.4	18.0	0.9	3.9	1.3	53.6	40.0	23.4	-6.7	39.0	34.4	20.7	-1.2
	Std.	1.2	5.4	0.3	0.1	0.1	0.0	1.3	0.5	0.6	0.1	0.8	0.2	0.4	0.0
	COV	3.0%	226.8%	1.5%	14.8%	3.0%	3.0%	2.3%	1.2%	2.7%	0.8%	2.1%	0.7%	1.8%	2.7%
3.06 (0.06)	**Ave.**	-61.4	-12.3	38.5	1.6	4.9	2.4	93.7	72.0	41.8	-12.4	67.5	59.4	43.1	-1.5
	Std.	0.7	0.2	0.3	0.0	0.1	0.2	1.6	0.8	3.0	0.6	0.9	0.6	0.9	0.0
	COV	1.1%	1.3%	0.8%	2.1%	2.4%	7.2%	1.7%	1.1%	7.2%	4.9%	1.3%	1.0%	2.1%	2.4%
3.97 (0.08)	**Ave.**	-86.3	-16.0	60.7	1.9	6.9	2.7	130.3	101.7	58.5	-27.8	94.0	84.9	54.7	-3.8
	Std.	1.1	1.2	0.4	0.1	0.1	0.2	1.3	0.2	14.9	1.9	0.8	0.3	0.8	0.2
	COV	1.3%	7.4%	0.6%	5.0%	1.2%	7.1%	1.0%	0.2%	25.5%	6.9%	0.9%	0.3%	1.4%	4.9%
5.08 (0.05)	**Ave.**	-119.8	-20.7	86.7	2.9	7.3	4.3	171.5	132.9	72.8	-31.3	124.6	110.7	71.7	-3.1
	Std.	1.5	0.9	1.2	0.1	0.1	0.3	1.1	1.1	2.8	2.5	0.4	0.9	0.6	0.1
	COV	1.3%	4.5%	1.4%	3.8%	0.7%	6.6%	0.6%	0.8%	3.8%	7.9%	0.3%	0.8%	0.8%	2.8%

4.3.2 Biofidelity

Figure 4.4 displays the scaled acceleration profile from Nahum et al.'s T.37 and the averaged acceleration of the selected BIPED test. The scaled acceleration profile for T.37 was obtained by multiplying the cadaver acceleration time histories with the ratio of BIPED and

T.37 acceleration peaks, the same as the scaling method of the CSFP time histories. Figure 4.5 shows the averaged BIPED CSFP across repeated tests and the scaled CSFP from the cadaveric tests for the two groups of comparison. Figure 4.5 (a), (c), and (e) show the average time histories of the BIPED front, side, and back CSFP from repeated tests with PMC746 surface at the impact velocity of 5 m/s compared to the scaled time histories from Nahum's T.37 and T.48. Figure 4.5 (b), (d), and (f) show the average time histories of the BIPED CSFP from repeated tests with steel surface at the impact velocity of 2 m/s compared to the scaled time histories from Nahum's T.49, T.51, and T.52. Table 4.2 and Table 4.3 provide the peaks and relative CSFP differences between the BIPED and cadaver tests. The back ICP decreased to negative and then increased to positive pressure; thus, both the minimum and maximum CSFP are reported in the tables.

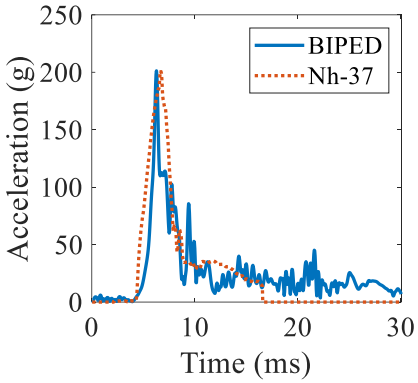

Figure 4.4. Averaged accelerations of the BIPED repeated tests compared with the scaled acceleration from Nahum et al.'s T.37 [108].

The BIPED front CSFP peak and back negative peak were within the range of the scaled cadaver (between the minimum and maximum values), indicating that the variation between the BIPED and cadaver data can be lower than the variation within the cadaver data. However, side CSFPs were 28.7–92.1% greater than all the cadaver side pressure (Table 4.2

and Table 4.3). The relative differences in the average front CSFP peaks between the BIPED repeated tests and cadaver tests in the two comparisons were 7.7% (Table 4.2) and -6.5% (Table 4.3). The BIPED side CSFP was up to 81.0% greater than the average cadaveric CSFP. The BIPED negative back CSFP peaks were 11.6% lower than the average back CSFP of T.37 and T.48 but 84.8% greater for comparison with T.49, T.51, and T.52, likely due to the large variance of the cadaver back CSFP. Notably, the maximum back CSFP was up to 18 times greater than the cadaveric data (Table 4.2).

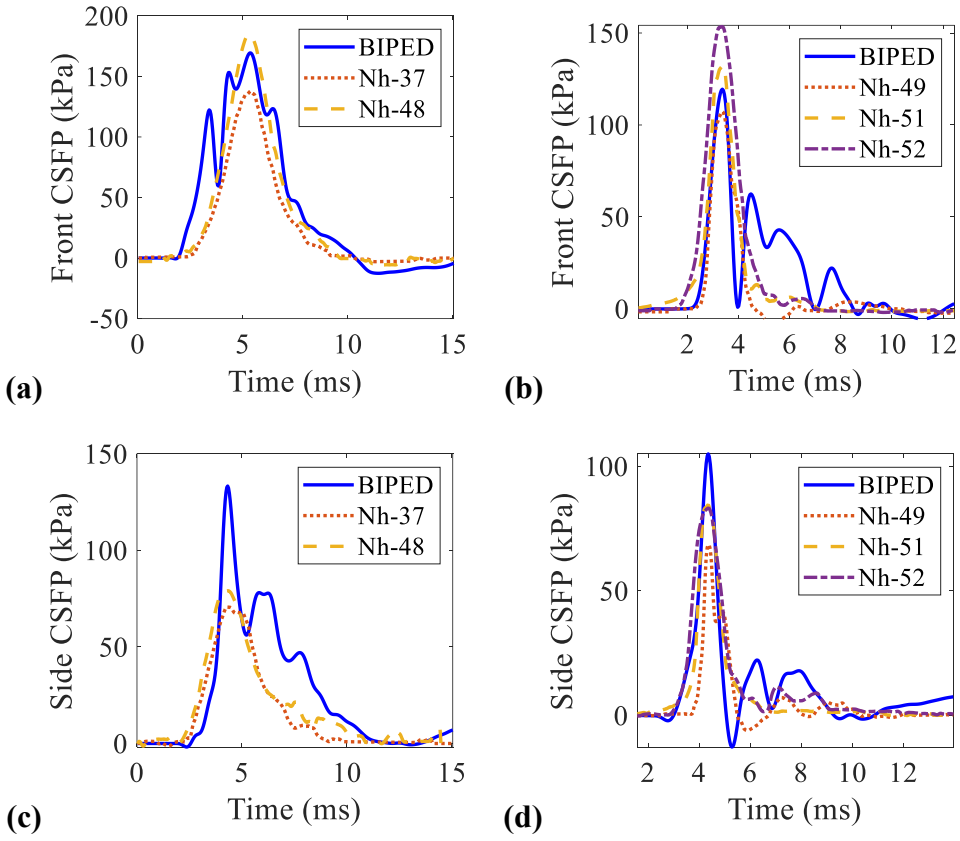

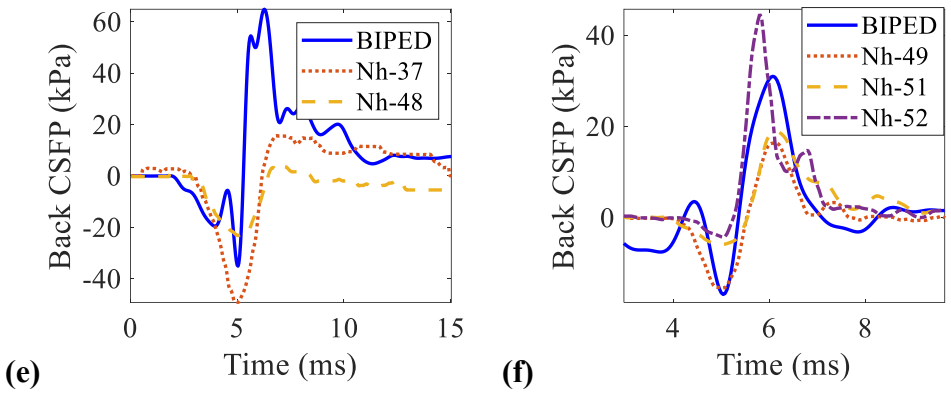

Figure 4.5. BIPED CSFP compared with scaled cadaveric CSFP from Nahum et al.'s study [108]. (a), (c), and (e) show the average time histories of the BIPED front, side, and back CSFP from repeated tests with the PMC746 surface at the impact velocity of 5 m/s compared to the scaled time histories from Nahum's T.37 and T.48. (b), (d), and (f) show the average time histories of the BIPED CSFP from repeated tests with the steel surface at the impact velocity of 2 m/s compared to the scaled time histories from Nahum's T.49, T.51, and T.52.

Table 4.2. CSFPs and accelerations for BIPED tests with PMC746 surface from the impact velocity of 5 m/s compared to Nahum's results from T.37 and T.48 [108]. The table lists BIPED measurement peaks, cadaveric original peaks and scaled peaks, and the percent difference between BIPED and cadaveric scaled peaks.

CSFP& Acc.	BIPED	T.37	Scaled T.37	% Diff.	T.48	Scaled T.48	% Diff.	Scaled Ave.	% Diff
Front (kPa)	171.5	142.3	135.0	27.0	121.4	183.4	-6.5	159.2	7.7
Side (kPa)	132.9	72.9	69.2	92.1	51.5	77.7	71.0	73.5	81.0
Back Max (kPa)	72.8	16.1	15.3	375.5	2.6	3.9	1790.7	9.6	659.9
Back Min (kPa)	-31.3	-50.9	-48.3	-35.3	-14.9	-22.4	39.3	-35.4	-11.6
Acc. (g)	197.2	207.9	197.2	0.0	130.6	197.2	0.0	197.2	0.0

Table 4.3. CSFP and accelerations for BIPED tests with steel surface from the impact velocity of 2 m/s compared to Nahum's results from T.49, T.51, and T.52 [108]. The table lists the BIPED measurement peaks, cadaveric original peaks and scaled peaks, and the percent difference between BIPED and cadaveric scaled peaks.

CSFP& Acc.	BIPED	T.49	Scaled T.49	% Diff.	T.51	Scaled T.51	% Diff.	T.52	Scaled T.51	% Diff.	Scaled Ave.	% Diff
Front (kPa)	119.4	258.6	105.2	13.5	498.1	128.6	-7.1	460.5	149.4	-20.0	127.7	-6.5
Side (kPa)	105.0	162.9	66.3	58.4	316.0	81.6	28.7	247.2	80.2	30.9	76.0	38.1
Back Max (kPa)	31.0	39.3	16.0	93.4	66.0	17.0	81.8	127.9	41.5	-25.4	24.8	24.6
Back Min (kPa)	-16.9	-36.2	-14.7	14.5	-26.7	-6.9	145.0	-17.8	-5.8	192.5	-9.1	84.8
Acc. (g)	142.0	348.9	142.0	0.0	550.0	142.0	0.0	437.8	142.0	0.0	142.0	0.0

The CSFP was linearly associated with the resultant linear accelerations with coefficients of determination R^2 ranging from 0.96–1.00, and the linear trendline for the front CSFP had no statistical difference from that found in the cadaver study [108]. Figure 4.6 provides the average of the front (Figure 4.6(a) and (b)), side (Figure 4.6(c) and (d)), and back positive peak CSFP (Figure 4.6(e) and (f)) plotted against the resultant accelerations of three axes and corresponding regression trendlines. For the front impact, the cadaveric CSFP-acceleration trendline was between the regression lines of the BIPED impacts on PMC746 and VN600 surfaces (Figure 4.6(a)). The cadaveric data points in Figure 4.6 were from tests of the cadaver when varying the impact surface and velocity. When pooling the BIPED data from different impact surfaces, the trendline for the front CSFP aligned with that for the cadaver tests, as shown in Figure 4.6(b). The slope (0.91) of the regressions for the BIPED pooled data had no significant difference from that of the cadaveric data (0.94) with a p-value of 0.74. The

slope of regression lines for the back pressure also had no significant differences (p=0.65), but the intercept for the BIPED (2.88) was notably higher than for the cadaver (-16.60), shown in Figure 4.6(f). For the side pressure, the BIPED trendline slope was significantly greater (p<0.001) than the cadaver trendline, shown in Figure 4.6(d).

CORA ratings for the front CSFP (0.68 and 0.72) suggest a good match of the time histories of the front pressure (Table 4.4). The total ratings for the side CSFP (0.44 and 0.70) were lower than the front CSFP. Among CSFP at the three locations, the back CSFP ratings were the lowest, with total ratings being 0.27 and 0.66.

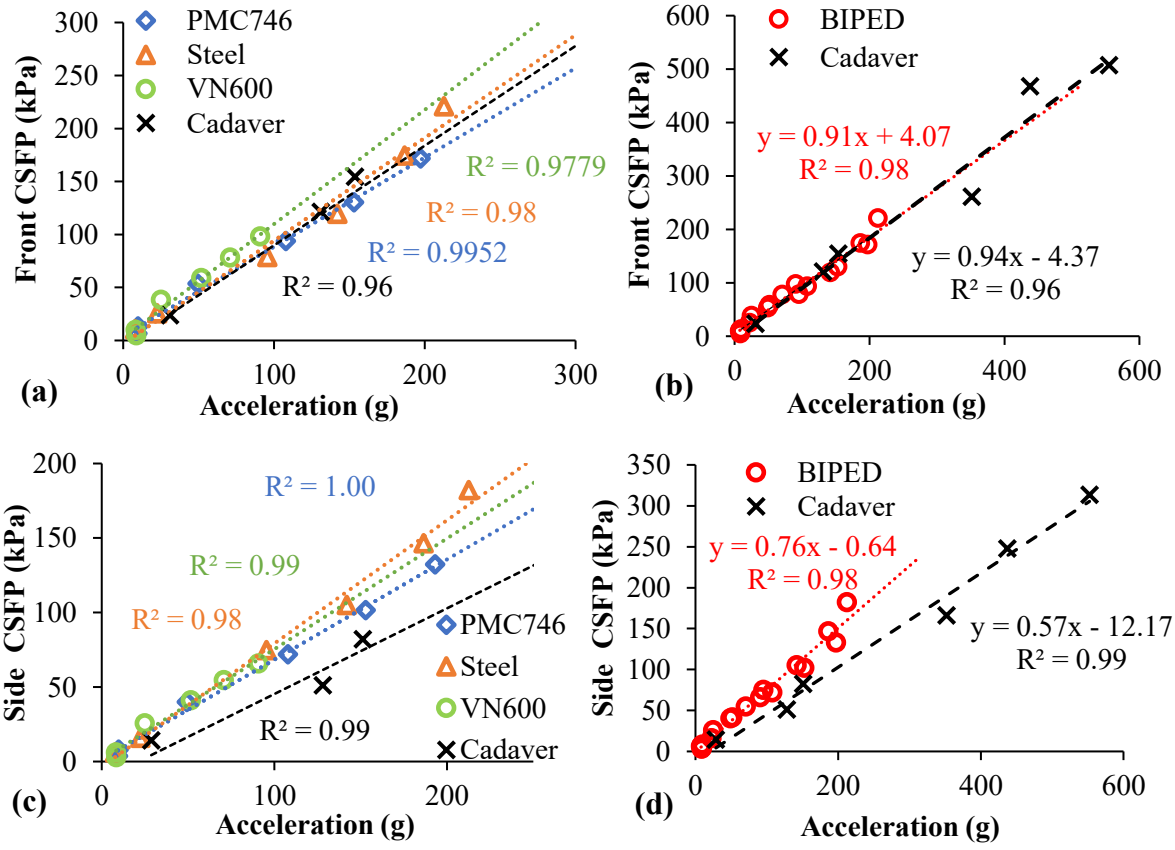

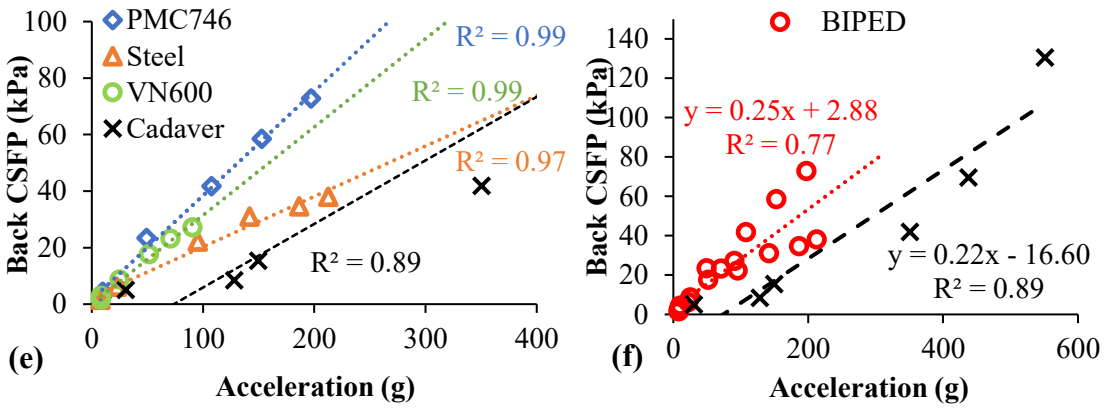

Figure 4.6. Comparison of CSFP peaks varying with accelerations between BIPED and Nahum et al.'s cadaver tests. (a), (c), (e) shows the regression analysis of BIPED CSFP and accelerations for each impact surface compared to cadaveric data. (b), (d), (f) show the regression analysis regardless of the impact surface compared with the cadaveric data. Not all the cadaveric data points are shown in (a), (c), and (e), but the same cadaveric data are all shown in (b), (d), and (f).

Table 4.4. CORA sub ratings and total ratings of the BIPED CSFP from impact with PMC746 and steel surface compared with Nahum's cadaveric data [108]. Cross-correlation rating (CC) is a sum of 50% shape, 25% size, and 25% phase ratings. The total rating is a sum of 50% CC and 50% corridor rating.

CSFP	Comparison	Shape	Size	Phase	CC	Corridor	Total
Front	BIPED-PMC	0.83	0.69	0.70	0.76	0.59	0.68
	BIPED-Steel	0.82	0.61	0.94	0.80	0.64	0.72
Side	BIPED-PMC	0.76	0.49	0.23	0.56	0.33	0.44
	BIPED-Steel	0.84	0.72	0.77	0.79	0.61	0.70
Back	BIPED-PMC	0.08	0.33	0.16	0.16	0.39	0.27
	BIPED-Steel	0.66	0.46	1.00	0.69	0.63	0.66

4.4 Discussion

This study sought to characterize the ICP biofidelity and the kinematics and ICP repeatability of the BIPED when subjected to translational blunt impact. The commonly used headforms are limited to replicating head kinematics. To obtain key intracranial responses such as ICP and brain strains, researchers commonly use numerical models probably due to the lack of appropriate physical head models [91]. On the one hand, numerical models using kinematics as input may be inappropriate to replicate intracranial responses when skull deformations caused by the impact contribute to the intracranial responses, since local skull deflections have been found to affect brain pressures while maintaining the head linear accelerations [143]. On the other hand, simulating all objects involved in an impact incident, such as the head, headgear, and impactor is complicated and particularly challenging when the constitutive models and contact characteristics of novel safety gear are not fully understood. Compared to numerical models, physical models have the notable advantage of being easy to manipulate and allowing direct interaction with the surrounding environment. Sophisticated headforms that can accurately provide ICP measurements in addition to kinematics can potentially extend the understanding of head injuries and improve the assessment of protective headgear.

The BIPED kinematics and ICP including the CSFP and IPP generally demonstrated acceptable repeatability during the pendulum impacts. Except for some kinematics and back ICPs with a mean of approximate zero, the measures for all the impact scenarios generally had COVs lower than the upper threshold of good repeatability (7%) and more than half of the measures had COVs below the excellent repeatability threshold of 3%. The extremely large COVs for the linear accelerations in the Y direction and angular rates in the X and Z directions were attributed to the low means as the COV was the standard deviation divided by the mean

of the measures. The relatively large COVs of the back ICP can be attributed to combined factors of the contrecoup pressure measured at the opposite side of the impact site. The pressure wave induced by impacts propagates from the impact site of the head throughout the front CSF and the brain to the back side of the cranium, resulting in back ICP. Due to the relatively far location from the impact site, the back ICP peaks were close to zero for low impact velocities, resulting in large COVs. Moreover, the head accelerations, CSF distribution, brain motions, and the sensors and cables in the brain can all affect the initiated pressure magnitudes and pressure propagation, contributing to the variance of back ICP. Despite the few large COVs, the low COVs of most measures indicated that the BIPED was repeatable considering both global head kinematics and ICPs for frontal impacts. Moreover, the low COVs also demonstrated that the described method of equipping the BIPED with kinematic and ICP sensors was suitable.

Based on the comparison with the available cadaver tests, the BIPED front CSFP demonstrated good biofidelity considering both the peaks and time histories. The BIPED front CSFP peaks were only slightly different (<10%) from the average of cadaver peaks. The ISO Technical Reports TR9790-1 for a dummy requires that the difference of head acceleration peaks with cadaveric data should be within ±15% [96]. No requirements have been defined for ICP, but the requirement for the accelerations can be applied to ICP since studies found the ICP was proportional to accelerations in blunt impact [108]. Therefore, the peaks of the front CSFP meet the biofidelity requirement referring to the ISO TR9790-1 standards. Moreover, the linear trendline of the BIPED front CSFPs against accelerations aligned well with that of the cadaveric data, confirming that the BIPED front CSFP peaks are comparable with the cadaveric data regardless of the acceleration peaks. On the other hand, the time histories of the

BIPED front CSFP also demonstrated good global biofidelity as CORA ratings (0.68–0.72) are close to the threshold of good biofidelity of 0.7. The high cross-correlation ratings indicating the closeness in the shape and size of the front CSFP profiles contributed to the good global biofidelity. The corridor ratings were relatively low compared to the cross-correlation ratings due to the vibrations of the CSFP signals proved by the spikes of the signals shown in Figure 4.5(a) and (b).

The shape of the BIPED side CSFP profiles matched with cadaveric CSFP, but the peaks were over 20% greater for comparison with all the cadaver tests. Although the total CORA ratings (0.44 and 0.70) of the side CSFP were notably different for the two comparisons, the shape sub-ratings were both greater than 0.7. It is reasonable that the shape of the time series matched well since the comparison tests were selected based on similarity in pulse durations, the factor that partially determines the shape. The discrepancy of peaks was possible due to the larger volume (1491 cm^3) of the BIPED brain than the average cadaver brain (1274 cm^3). The brain is constrained by the rigid skull. During the front impact, the skull moves toward the brain. Thus, the front region of the brain compresses, and the side region dilates due to the incompressibility of the brain surrogate. A larger volume of the BIPED brain may lead to more compaction at the side of the head, thus resulting in a higher side CSFP. A study using a numerical model also found that peak ICP was proportional to brain size [143]. Another reason may be that the BIPED had no meninges to maintain the shape and location of the brain. Therefore, the BIPED brain may experience more dilation at the side region than the cadaver brain. The saline water served as CSF was less viscous than the CSF in the human head, which may also affect the CSFP. However, further research is required to examine these factors in order to improve the ICP biofidelity of the BIPED.

Both the positive and negative peaks of the BIPED back CSFP were in the range of cadaveric data but had a large difference with the cadaveric data, indicating that further comparison with more cadaveric data is warranted to draw a conclusion. The large difference may be partially due to the influence of the IPP sensors and cables in the BIPED brain that may alter the pressure propagation. Moreover, the BIPED back CSFP sensor was likely not placed at the same location as in some cadaver tests, which may result in a larger pressure difference. In the cadaver experiment, pressure sensors at the back were placed adjacent to each other to examine if the sensors would yield similar results [108]. The remarkable variation of percent difference (-35.3–1790.7%) is possibly due to the large variation in cadaver measurements caused by the sensor locations. As seen in Figure 4.5 (e), the back CSFP for the Nahum's T.37 and T.47 only exhibited negative impulses, whereas the cadaver time histories in Figure 4.5(f) exhibit both negative and positive impulses. As a result, in the comparison with T.37 and T.47, the maximum back CSFP for the BIPED was up to 18 times greater than for the cadaver, and the total CORA rating for the back CSFP was approximately 50% lower than other total ratings. However, in the comparison with cadaveric T.49, T.51, T.52, the total CORA rating (0.66) approached the good biofidelity of 0.7 based on Gehre et al. [101]. Therefore, comparison with more cadaveric back CSFP data measured at the same regions is warranted to conclude the back CSFP biofidelity.

The BIPED CSFP measured at each side was linearly related to the accelerations, in agreement with the cadaveric CSFP-acceleration trend. The slopes of the BIPED front and back CSFP-acceleration relations were not significantly different from a cadaver, whereas the side CSFP presented significantly different slopes. It is not surprising that the trendlines for front CSFP-acceleration relations overlapped (Figure 4.6(b)) as the result is in agreement with

previous comparisons between the CSFP peaks (Table 4.2 and Table 4.3). In previous comparisons, the cadaveric CSFP and linear accelerations were scaled by multiplying a ratio to match the cadaver and BIPED accelerations. The BIPED front CSFP peaks were found in the range of cadaveric data for the same acceleration peaks. The current comparison of the trendlines did not scale the cadaveric data as its linear trendline is independent of the linear scale process. Note that the BIPED and cadaver back CSFP-acceleration trendlines were parallel but the cadaver trendline was lower (Figure 4.6(f)). This is because the cadaver trendline had a notable intercept (-16.60), due to the small sample size (n=6) of the cadaver test and the large variance of the back pressure.

Compared to the limited cadaver IPP, the BIPED IPP responses were in line with the reported ICP measured in brain parenchyma. To our knowledge, only Hardy et al. inserted pressure sensors into the brain parenchyma of cadavers to measure IPP in blunt impact [134]. An average peak coup pressure of 68 ± 48 kPa (i.e., the pressure under the impact site), contrecoup pressure of -26 ± 51 kPa, and a mean acceleration of 124 ± 38 g were reported when stopping cadaver head subjects that moved horizontally with an acrylic block. For a similar impact surface (i.e., the PMC746 surface) and the same acceleration of 124 g, the BIPED coup and contrecoup IPP were 99.6 and -3.5 kPa interpolated from the IPP-acceleration linear relationship. Although up to 46% higher than the mean, the IPP was within one standard deviation of the mean in Hardy's study.

This study has several limitations. The BIPED was only compared to limited cadaveric ICP measurements. A limited number of studies have measured ICP in the human head, since installing the necessary sensors into the CSF and brain without damaging the brain constitution is challenging, and obtaining cadaver specimens can be difficult and possesses ethical

concerns. There was a lack of cadaveric ICP data for other head impact locations such as the side and back impacts. Thus, this study limited its comparison of BIPED ICP to a few cadaver tests with frontal impacts [108], [134]. Nevertheless, most current numerical and physical models validate their brain and head models based on the same cadaveric data that we used in the current study [21], [151]. In addition, we assumed zero intercepts when scaling cadaveric ICP, while the ICP-acceleration equations shown in Nahum's study had nonzero intercepts [108]. Thus, the scaled ICP was slightly different from what would be calculated using the equations in Nahum's. However, it is reasonable to assume zero intercepts based on the mechanisms of ICP and accelerations. Since the cadaveric experiments had no constraints or shield on the head, the ICP and acceleration would generate together in response to an impact and therefore a zero acceleration would indicate a zero ICP change.

Moreover, as mentioned before, the possible difference in pressure and acceleration sensor locations as well as measurement methods compared to cadaveric experiments may cause bias in the data in comparison. Since Nahum's cadaveric study did not provide the coordinates of the sensors used, the present experiment matched the cadaveric study as possible as we could. Nahum et al. obtained resultant linear accelerations from biaxial accelerations in the midsagittal plane, while our study used resultant linear accelerations based on triaxial accelerations [108]. However, we found that the difference in resultant linear accelerations from the biaxial and triaxial measurements was negligible since the BIPED impact direction was within the midsagittal plane while the head linear movement perpendicular to the midsagittal plane was negligible.

To compare the ICP with cadaveric data, we matched the linear accelerations instead of the impact conditions such as the impact surface and velocity with the cadaver study. A

primary reason is due to the unknown impact surface used in Nahum et al.'s cadaveric study and our pendulum setup was not meant to operate at the high impact velocities (5–8 m/s) that were used in the cadaver study [108]. Since the Hybrid III neck is stiffer than the human neck [158], even the same impact conditions would likely result in different head kinematics. Therefore, this study compared the ICP based on the match of linear accelerations since the mechanism of ICP has long been correlated to linear accelerations [18], [71]. As a result, characteristics of BIPED ICP biofidelity in our study are limited to informing future improvement of the head internal structures which do not affect head acceleration biofidelity. Our previous study found that the BIPED acceleration peaks have no statistically significant difference with cadaveric data, but BIPED pulse durations are longer [120]. Since ICP is dependent on the accelerations, future biofidelity improvement based on the acceleration pulse durations will improve the ICP biofidelity as well. Another limitation associated with the comparison is that we did not mass scale the acceleration and ICP as the mass of the cadaver head is unknown. Since head mass affects head linear accelerations but has no effect on ICP based on Panzer et al.[136], the head mass can affect the relationship between ICP and head linear accelerations and thus should be taken into consideration when possible.

4.5 Conclusion

This study characterized the ICP biofidelity and kinematic and ICP repeatability of the BIPED subjected to translational impacts. Our evaluation suggests that the BIPED can provide biofidelic coup ICP and highly repeatable kinematics and ICP measurements for frontal impacts. The side CSFP peaks were substantially different from previous cadaveric data, which highlighted the need to improve the biofidelity of the head's internal components. This study provides important insights into the biofidelity and repeatability characteristics of a

comprehensive headform that might be a new useful tool for application to studying head injuries in blunt impacts. The findings inform the future work of improving the ICP biofidelity, toward a biofidelic and repeatable headform capable of replicating both global head kinematics and intracranial responses.

Chapter 5 Improving the BIPED Biofidelity by Refining the Surrogate Scalp

Based on the results of the studies in Chapters 3 and 4, the BIPED exhibits repeatable kinematic and ICP responses and shows promising biofidelity, though the biofidelity could be further improved. One of the major limitations related to the BIPED biofidelity was that its acceleration pulse duration was approximately 50% greater than cadaveric data. The long pulse duration negatively impacted the overall biofidelity level of both the acceleration and ICP responses since ICP is correlated to linear accelerations. The longer pulse duration was likely associated with the lower stiffness of the BIPED headform compared to cadaver heads. Therefore, improving the head stiffness to reduce the pulse duration was the focus of the refinement.

As an external layer of the head, the scalp plays an important role in head stiffness and impact responses, but how to refine the thickness and material of the scalp to improve the biofidelity is unknown. To provide guides on improving the biofidelity of the BIPED, the study presented in this chapter aimed to evaluate the influence of surrogate scalp material and thickness on head accelerations and ICP. The content below has been submitted to the Journal of the Mechanical Behavior of Biomedical Materials as an original research article.

5.1 Introduction

Head injuries commonly occur in falls, sports, motor vehicle crashes, and military settings, and are a major worldwide health concern [10], [159]. In the United States alone, 2.8 million cases of head injury occur annually, with associated costs of $76.5 billion [160]. 2%

of such injuries result in death [160]. Globally, an estimated 69 million individuals suffer from traumatic brain injuries (a major subset of head injuries) each year [10].

The headforms of Anthropometric Testing Devices (ATD) are typical physical head surrogates that are commonly used in biomechanical research and the assessment of protective devices designed to reduce the risk of head injury. These head surrogates are generally designed to replicate human head responses under comparable loading conditions. Human cadavers offer anatomical representations of live humans and can provide valuable data for biomechanical research [11]. However, using human cadavers involves drawbacks such as limited specimen availability, storage technique challenges, experimental complications, low reusability, and ethical restrictions. In comparison to cadaver heads and human volunteers, headforms have the advantages of being easy to use and store, durable, reusable, and pose no ethical concerns [11].

Although the structures and mechanical properties of surrogate head components can be significantly different from those of the human head, several headforms are available that can replicate the global kinematics of the human head. Head kinematics including linear acceleration, angular acceleration, and angular velocity are correlated with the mechanisms and risk of head injuries [63], [124]. To simulate the human head's linear and rotation kinematics, the common headforms are generally designed to mimic the mass, shape, moment of inertia, and global stiffness of the human head. Standardized headforms such as the ISO/DIS 6220 and EN960 consist of a headlike shell of urethane or metal without internal anatomical components [104]. The commonly used Hybrid III headform consists of a hollow aluminum shell and a vinyl scalp [161]. The scalp is less stiff than the human scalp to offset the large stiffness of the aluminum skull [161]. A sport-standard headform developed by the National

Operating Committee on Standards for Athletic Equipment (NOCSAE) comprises a polyethylene skull filled with a glycerin brain simulant [149]. However, the NOCSEAE headform has no other intracranial structures, and the physical characteristics related to brain responses were not considered in its development [105]. Therefore, these headforms measuring pure global kinematics generally lack the simulation of anatomical details which may require considerations for advanced headforms measuring both the kinematics and intracranial mechanics.

Intracranial mechanics such as intracranial pressure (ICP) in the cerebrospinal fluid and brain parenchyma, brain stress, and brain strain have been associated with TBIs; however, to our knowledge, there is currently no commercially available headform that can replicate these mechanics [162], [163]. An impact to the head can generate stress waves that propagate in the skull and brain, resulting in an increased ICP near the impact side, a decreased ICP at the opposite side, and pressure gradients throughout the brain [18], [164]. These pressure changes cause compression, tension, and shear stresses of the brain tissue, and thus the ICP has been proposed as an injury mechanism and is associated with the risk of brain injuries [75], [90]. Some numerical simulation studies suggest using injury risk models based on ICP, brain stresses, and strains as these mechanics are more closely related to brain responses than global head kinematics [162], [165]. However, studies of such intracranial mechanics are limited to numerical studies due to the lack of adequate physical head surrogates, which may be problematic in the context of helmet assessment where a physical head is needed to exhibit realistic head-helmet interaction. To replicate intracranial mechanics, headforms require a complex design of anatomical details including the structure, geometry, and materials of the internal and external head components.

Few studies have attempted to develop physical head models with internal components such as a brain to simulate intracranial mechanics in addition to kinematics [102], [22]. Freitas et al. developed a human head surrogate that contained surrogate tissue such as the brain and dura for studying the ICP and acceleration responses resulting from non-perforating ballistic impact [17]. As the skull was a refreshed human cranium, this head surrogate was prone to fracture under severe impact conditions and thus was not a robust device for repetitive use. A recent study used a hollow polycarbonate spherical shell filled with water to study the head dynamic responses including ICP and accelerations induced by pendulum impact [166]. This simple head model is likely not biofidelic as its structures, dimensions, and materials were greatly different from those of the human head. Another head surrogate for impact tests simulated the external geometry and anatomic components of the human head, targeting providing biofidelic ICP responses [21]. However, the kinematics of this head surrogate has not been validated against cadaveric data from published work. Although originally developed to measure the ICP in blasts [22], the Blast Injury Protection Evaluation Device (BIPED) is one of the few head surrogates that contain the main anatomic details of the human head and has demonstrated potential for use in blunt impacts. The details of the head design are introduced in section 5.2.1. A recent study evaluating this headform found that the acceleration peaks were not statistically significantly different from cadaveric data but the pulse durations were 49% greater [120]. The impact stiffness of the BIPED was up to 53% lower than that of cadaver heads. It was suggested that the biofidelity of the headform can be improved by refining the scalp and skull to tune the stiffness of the surrogate head [120]. Considering the relative biofidelic structure of the BIPED and its potential of providing biofidelic and

repeatable kinematics and intracranial mechanics, this study was based on experiments using the BIPED.

The scalp plays an important role in head impact responses during blunt impact loading conditions. Using the EN960 headform for drop impacts, Trotta et al. found that adding a porcine skin to the headform surface resulted in a decrease in peak accelerations of up to 25% and a decrease in impact energy of up to 69% [167]. The scalp significantly influences head kinematics since it affects head mechanical properties and sliding interactions [167]. A study impacted a deformable skull on the Hybrid III scalp padding and another stiffer padding individually. The resulted accelerations for the Hybrid III scalp padding were half of that for the stiffer padding, likely due to the lower stiffness of the Hybrid III scalp [168]. However, how altering the material and thickness of the scalp can change the global and intracranial responses of a headform is unclear when refining the head design.

Based on the above considerations, this study aimed to investigate the influence of material and thickness of surrogate scalps on the impact response of the head-brain model BIPED, in an attempt to refine the design to improve its biofidelity for use in blunt impact. The specific objective was to use the BIPED headform and scalp pads of different moduli and thicknesses to evaluate the influence of these parameters on the impact accelerations and intraparenchymal pressures and to identify an optimal choice of the scalp that could effectively improve the BIPED biofidelity.

5.2 Materials and Methods

5.2.1 Head surrogate

The BIPED consists of a surrogate scalp, two halved skulls, a brain surrogate, a saline water layer serving as the cerebrospinal fluid, and tentorium and falx membranes. Figure 5.1 shows the models of the BIPED skull and brain components (Figure 5.1(a)) and the BIPED assembly with pressure sensors in the brain (Figure 5.1(b). Details on the head geometry, materials, and instrumentation can be found in previously published literature by Ouellet et al. [22] and Li et al. [120]. Briefly, the dimension and geometry of the head simulated the average male. The skull, CSF, and brain are modeled with the TC-854 A/B Polyurethane (BJB Enterprise Inc., CA United States), saline water, and Sylgard 527 silicone gel (Dow Corning Corporation, MI United States), respectively.

The scalp is made from urethane rubber Vytaflex20 (Smooth-On Inc., PA United States) and has an average thickness of 6 mm. The skull thickness (6.35 mm) and the compression elastic modulus (2.275 GPa) are within the reported human head data [40], [169]. Filling the skull cavity, the surrogate brain has a density (907 kg/m3) and bulk modulus (1.065 GPa) close to the human brain (1081 kg/ m^3 and 2.1 GPa) [170], [171]. Moreover, the Sylgard 527 silicone gel is nearly incompressible with a Poisson's ratio approaching 0.5 [115], similar to that of the human brain tissue (0.49–0.5) [60]. While brain tissue exhibits non-linear viscoelastic behavior with shear softening above 5% strain [116], the Sylgard 527 behaves as a linear viscoelastic solid for strain up to 50%. The shear storage and loss modulus of the Sylgard 527 are on the same order of kPa as the human brain tissue or porcine brain tissue for oscillation frequencies up to 200 Hz [60], [172], [173]. Thus, the Sylgard 527 is agreed to be

an adequate surrogate brain material for low shear strains and low loading frequencies [22]. Although the Sylgard 527 silicone brain may not exactly replicate human brain responses for high strains and strain rates, it can be used in trend and relative comparison studies [116]. Since the bulk modulus of the Sylgard 527 has a magnitude in the order of 1 GPa while the shear modulus magnitude is in the order of 1 kPa [117], [118], the brain pressure measured with a pressure sensor depends mainly on the bulk property of the material. As a result, the effect of non-linear shear behavior on intracranial pressure is negligible since shear softening properties only apply to deviatoric behavior. The original BIPED mark 1 (mk1) was used in this study. A BIPED mk2 version based on mk1 is currently under development for use in blunt impact scenarios. For this study, the original BIPED scalp was removed and replaced with pads that simulated the scalp at the impact region.

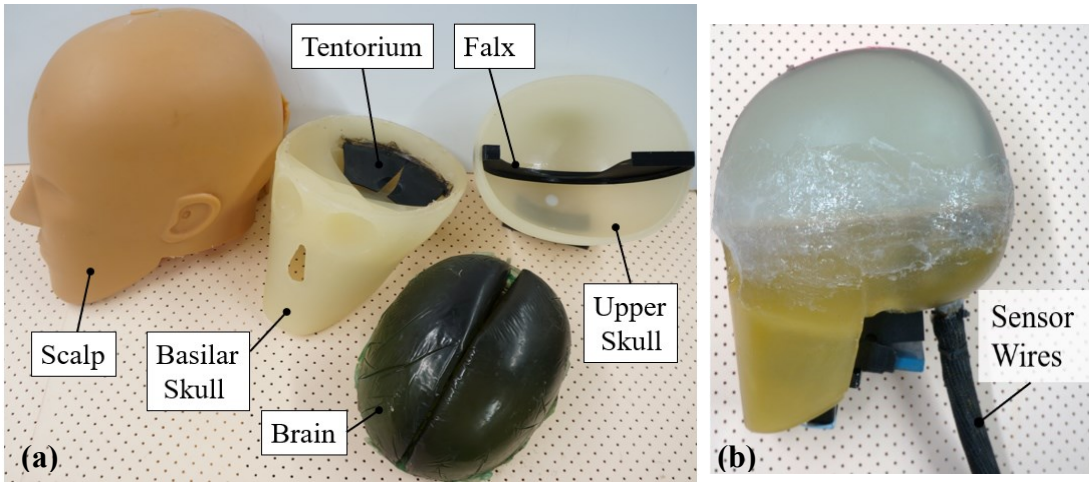

Figure 5.1. (a) models of the BIPED components including the brain, basilar skull, upper skull cap, tentorium, and falx membrane, (b) BIPED assembly without the scalp

5.2.2 Surrogate scalp pads

To study the effect of surrogate scalp material and thickness on head impact responses, four urethane rubber materials including Vytaflex20, Vytaflex40, Vytaflex50, and PMC746 (Smooth-On Inc., PA United States) were each molded into four pads with thicknesses of 2, 4, 6, and 8 mm. Urethane rubbers are resistant to abrasion and tearing, ensuring the durability of the scalp under repetitive head impacts. Additionally, urethane rubbers are flexible, making the installation and removal of the scalp easy. The densities of these materials (1000–1030 kg/m3) are similar to the density of the human scalp (1000 kg/m3) [29]. The Vytaflex series and the PMC746 material were selected based on the range of their shore hardness (Shore A 20 to 60) which is similar to the reported hardness of human skin (shore A 20 to 75) [174], [175]. The thicknesses were chosen based on the reported thicknesses of the human scalp (1–9 mm) [27]. The pad area (9 cm by 9 cm) was selected to fully cover the impact region (~3 to 5 cm diameter) on the skull.

As stiffness is positively correlated to Young's elastic modulus [176], the modulus was used to distinguish between the selected surrogate scalp materials in this study. The compression modulus of each material was determined by compressing the samples of each pad material at a rate of 0.1 mm/s (0.013/s) using a customized material testing system that has a maximum loading capacity of 25 lb. For each material, a 5 by 5 mm square was cut from the 8 mm thickness pads to serve as the testing sample. Due to the low loading range, a small cross-section area was chosen for the samples to generate sufficiently high stress and strain values. Before the test, the testing sample was placed freely on a steel position plate under the center of the compression loading head which has a load cell to capture the loading force. A preload of 1 N was used to initiate the compression of the sample. Then the sample was

compressed to reach the maximum loading capacity of the system, resulting in 50%–65% strain of the testing samples. Each test was repeated three times. The stresses were obtained by dividing the force by the cross-section area of the sample, and the strains were calculated by dividing the measured displacements of the loading head by the sample's thickness. The secant modulus for each material was calculated based on the slope of the line between the zero point and the point at the 50% strain on the stress-strain curves. The measured modulus and the hardness of the materials are presented in Table 5.1.

Table 5.1. The Shore A hardness and estimated modulus of the pad materials

Properties	VytaFlex20	VtaFlex40	VytaFlex50	PMC746
Shore A Hardness	20	40	50	60
Modulus (MPa)	1.868	3.337	4.309	5.573

5.2.3 Experimental Setup and Method

The experimental setup consisted of a monorail drop tower, a drop release actuator, a gimbal assembly, an aluminum impact plate, a load cell positioned under the impact plate, a steel anvil, and data acquisition hardware and software (Figure 5.2(a)). During the experiments, the scalp pad was kept in place on the BIPED skull surface using a stretchable nylon net from a thin stock that tightly covered the head without changing the impact stiffness (Figure 5.2(b)).

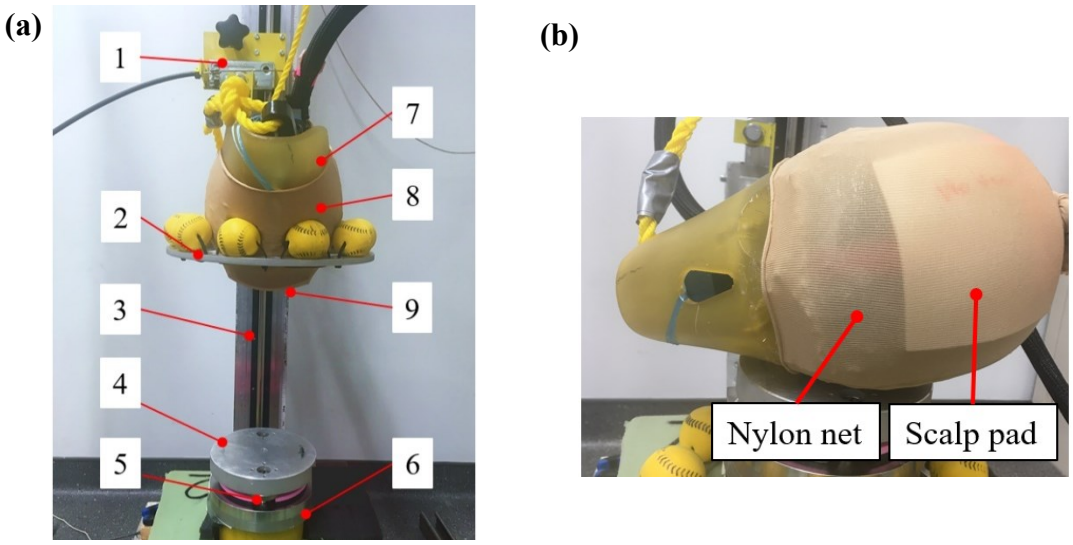

Figure 5.2. (a) Experimental setup showing the drop release actuator (1), gimbal (2), monorail (3), impact plate (4), load cell (5), anvil (6), and BIPED (7) with a scalp pad (9) attached using a nylon net (8). (b) An example of the BIPED skull-brain model with a scalp pad attached to the forehead.

The load cell (PCB 208C05, PCB Piezotronics Inc., NY United States) was installed between the impact plate and the anvil to measure the impact force of the headform (Figure 5.2(a)). Linear head accelerations were estimated by applying Newton's second law, impact force divided by the mass of the head. We used this method to obtain the linear acceleration along the vertical drop direction, which was the same as the method used in Loyd's cadaveric study [133]. Loyd et al. dropped cadaver heads to a rigid plate and measured the impact force for calculating linear accelerations [133] Our setup replicated Loyd's setup such that the BIPED accelerations can be compared to the cadaver data from Loyd et al. Three pressure sensors (XCL-072, Kulite Semiconductor Products, NJ United States) were installed in the front, right, and back of the surrogate brain parenchyma. As mentioned before, the stress wave propagating in the brain results in pressure changes. The pressure sensors capture the brain

stresses normal to the sensor diaphragm, which is mainly governed by the volumetric stress since the bulk modulus of the brain material is far greater than its shear modulus. Details regarding the force and pressure instrumentation can be found in previous literature [120]. Due to the replacement of the full scalp with the pads, the impact mass was less than that of the BIPED with the full scalp. To address the reduction in mass, a weight of 0.65 kg was added to the neck mounting surface, resulting in an impact mass of 3.65 kg, close to the original BIPED weight of 3.85 kg.

Before impact, the headform was held in place by the gimbal, with the impact location facing downwards toward the impact plate. Once released, the head fell with the gimbal impacting the metal plate. Impact force and brain pressure at the impact site were recorded at a rate of 25 kHz using the load cell, the embedded pressure sensors, hardware PXI 6251and LabVIEW 2020 (National Instruments, Austin, TX United States). A hardware anti-aliasing filter with a cut-off frequency of 4 kHz was used to filter the pressure analog signals.

The headform was impacted at three locations (front, right side, and back of the head) and from two drop heights (5 and 19.5 cm). Each test was repeated three times. The 5 cm drop height corresponds to an average impact velocity of 1.00 m/s and was selected to avoid damaging the skull. The 19.5 cm drop height was selected to achieve the same impact velocity (1.74 m/s) as a previous experimental study using cadavers [133]. All the drops of 5 cm were performed before the drops of 19.5 cm.

5.2.4 Data Analysis Methods

Based on SAE J211b specifications, the force and pressure signals were also filtered by a 4^{th} order low-pass Butterworth filter using MATLAB R2020a (MathWorks, MA United

States) with a cut-off of 1650 Hz [154]. To provide comparisons to data from a cadaveric study, accelerations from the present study and the cadaveric study were mass scaled to the equivalent response of the 50th percentile male (4.5 kg) based on the scaling laws below [136].

$$\frac{a_1}{a_2} = \sqrt[3]{\frac{m_2}{m_1}},\ \frac{t_1}{t_2} = \sqrt[3]{\frac{m_1}{m_2}} \qquad \textbf{Equation 5.1}$$

where a, t, and m denote the acceleration magnitude, acceleration duration, and mass of subject 1 (the 50th percentile male) and subject 2 (BIPED). The scaling law was based on the assumption of the same material stiffness ($E_1 = E_2$), mass densities ($\rho_1 = \rho_2$), and similar geometries between the two subjects [136]. This assumption is reasonable when scaling the response based on only the mass. Historically, the scaling laws were based on equal strains caused by impacts using the dimensional analysis method, since strains are causes of tissue damage [136], [177]. For instance, the scaling law for linear accelerations can be derived based on the equations below.

$$\boldsymbol{\varepsilon = \frac{\sigma}{E} = \frac{F}{A \cdot E} = \frac{m \cdot a}{A \cdot E}} \qquad \textbf{Equation 5.2}$$

$$\frac{m_1}{m_2} = \frac{\rho_1 {L_1}^3}{\rho_2 {L_2}^3} = \frac{{L_1}^3}{{L_2}^3} \qquad \textbf{Equation 5.3}$$

$$\frac{a_1}{a_2} = \frac{m_2 A_1 E_1}{m_1 A_2 E_2} = \frac{\rho_2 {L_2}^3 \cdot {L_1}^2}{\rho_1 {L_1}^3 \cdot {L_2}^2} = \frac{L_2}{L_1} = \sqrt[3]{\frac{m_2}{m_1}} \qquad \textbf{Equation 5.4}$$

where ε, σ, E, A, and L are the strain, stress, elastic modulus, impact area, and length, respectively. Peaks and durations of the acceleration and coup pressure were acquired from the measurements using MATLAB. The acceleration duration was defined as the period across 0.1% of the acceleration peak, and the pressure duration was defined as the period across 20% of the pressure peak based on the previous study [120].

Multiple linear regression (MLR) was performed for each impact height and location to evaluate the influence of the pad material and thickness on the peaks and durations of both the acceleration and brain pressure. IBM SPSS Statistics 26 software (Armonk, NY United States) was used to conduct the MLR. We chose MLR because it can evaluate the significance of each variable's influence on the dependent variable as well as compare the relative strength of the influence. The independent variables of each MLR included the material modulus and the pad thickness. The dependent variable for each model was either the peak or the duration of the acceleration or the pressure. A total of 24 MLR models were analyzed, as shown in Table 5.2. The regression equation is:

$$Y = \beta_0 + \beta_m X_m + \beta_t X_t + \varepsilon \qquad \textbf{Equation 5.5}$$

where Y is the dependent variable (i.e., peak or duration of the acceleration or pressure); X_m is the material modulus; X_t is the pad thickness; β_0 is the intercept; β_m and β_t are the slope coefficients for the modulus and thickness variables, respectively; and ε represents the residual of the model.

The standardized β coefficients, adjusted coefficient of determination (R^2), and F value are key regression outcomes that capture the regression results. The standardized β coefficients, β_m for modulus and β_t for thickness indicate the strength of the influence of these independent variables on the dependent variable. The significance of the influence is indicated by p values of the β. R^2 quantifies the quality of fit between the measured acceleration or pressure and model predictions. The adjusted R^2 compensates for biases in R^2 due to small sample sizes. Based on Cohen, Regression models with R2 greater than 0.25 are generally deemed acceptable [178]. Finally, the F value indicates the efficiency of the model when

compared to a model with zero independent variables, and its corresponding *p*-value captures the model's significance. In other words, the *p*-value of the F-test assesses if all the β coefficients of the model are equal to zero. *p*-values smaller than 0.05 are considered statistically significant as 0.05 is used by a majority of statistical studies [179]. While recent studies suggest using a more stringent threshold such as 0.005 [179], we found that using 0.05, 0.01, or 0.005 would not change the general conclusion as most of the significant p-values in our results were lower than 0.001. IBM SPSS Statistics 26 software (Armonk, NY United States) was used to conduct the MLR.

Table 5.2. Summary of the MLR models for the experiments.

Dependent variable Y	Height	Impact location	Total NO. of models
Acceleration peak Acceleration duration Pressure peak Pressure duration	5 cm 19.5 cm	Front Right side Back	4X2X3=24

To assess the biofidelity of the BIPED with each scalp pad, the CORrelation and Analysis (CORA) method was used to evaluate the accelerations from the 19.5 cm drops at the three impact locations. Several methods can quantitatively assess the biofidelity of human surrogates, such as the ISO/TR 9790 standard, the ISO/WD 15830-1 standard, the Biofidelity Ranking System (BioRank), and the CORA [96]–[98], [180]. Both the ISO/TR 9790 and ISO/WD 15830-1 standards evaluate the closeness of only the peaks between tests with the headform and cadaver heads, while other information influential to head injuries such as the measures' duration is not considered [96], [97]. The BioRank assesses the biofidelity based on the accumulative variance across the time histories, which depicts the overall closeness of the magnitudes over time but cannot depict the closeness of individual aspects such as the size and

shape of the measures [98]. This study adopted the CORA method because it evaluates several different aspects of the measures, including the corridor, size, shape, and phase.

CORA quantifies the level of similarity between the time histories of the two tests [100], i.e. the BIPED accelerations and the previous cadaveric accelerations in this study. This method calculates biofidelity ratings based on two perspectives, the corridor and the cross-correlation of the comparison data. The corridor method specifies an inner and an outer corridor along the reference data, i.e., the cadaver accelerations. The corridor rating was calculated based on the relationship between the BIPED acceleration data points and the corridors. The cross-correlation rating was calculated based on the similarity of the comparison data's size, phase, and shape, each of which has formulae to calculate a rating [100]. The defaulted cross-correlation rating is a sum of 50% of the shape rating, 25% of the size rating, and 25% of the phase rating. The total CORA rating is the sum of the weighted corridor rating (50%) and cross-correlation rating (50%), with a range from "0" to "1" representing poor to perfect matches, respectively [100]. CORAplus 4.04 (pdh, Gaimersheim, Germany) was used to perform the CORA between the BIPED average accelerations across repeated impacts and average cadaveric data obtained from impacts of the same velocity [133]. All the parameters were set the same as in a previous study of the BIPED [120].

There is yet no clear scale between the biofidelity level and the CORA ratings. Using the software default parameters, some researchers assumed good biofidelity when the total rating was no less than 0.7 [101]. This study selected the inner and outer corridor widths as a standard deviation of the cadaveric data and a standard deviation of cadaveric data plus 15% of the BIPED peak, respectively, which were lower than the software defaulted 5 and 50% of the peak and had a stronger scientific basis. The selection of the inner corridors assumed that

a perfect match inferred the BIPED data was within a standard deviation from the average cadaveric data. The selection of the outer corridors assumed that poor head surrogates with responses outside of the outer corridors would fail to distinguish the head injury risk of 40% from 60% [120]. Thus, the outer corridor widths approximated the difference between injury risk of 40% and 60% in acceleration injury models proposed by [139]. Other parameters such as weights of each sub-ratings for calculating the total ratings used the software defaults, as these defaults have been empirically accepted in numerous studies. The other parameters used were the software defaults. Therefore, CORA ratings equal to or higher than 0.7 can be conservatively assumed as good biofidelity in this study. Nevertheless, the CORA ratings provide relative comparisons between different scalp models.

5.3 Results

The scalp pad thickness significantly influenced the peaks and durations of the accelerations and pressures for all impact scenarios ($p < 0.05$; all 24 β_t coefficients in Table 5.3 and Table 5.4). The material modulus significantly influenced the dependent variables for the 5 cm drop height ($p < 0.05$; 10 of 12 β_m coefficients in Table 5.3) but was not influential for the 19.5 cm drop height ($p > 0.05$; all 12 β_m coefficients in Table 5.4). The F values (4.70–352.31) were significant for all the models ($p < 0.05$; all 24 F values in Table 5.3 and 5.4), indicating that the regression models are all significant. Finally, the adjusted R^2 values were mostly between 0.5 and 0.93 (20 of 24 adjusted R^2 values demonstrating the goodness of fit for most of the models [178]. The peaks and durations of the acceleration and coup pressure measurements were summarized in Appendix Table A3.

The regression results demonstrate that the scalp thickness had a stronger influence on the dependent variables than the selected scalp materials. β_t in absolute value (0.34–0.93) was larger than absolute β_m (0.01–0.35) for all 24 models (Table 5.3 and Table 5.4). Additionally, β_t was negative for the peaks and positive for the durations in all the models, whereas β_m had the opposite relationship for the models where this coefficient was significant (10 of 12 β_m in Table 5.3). Thus, the thickness was negatively associated with the acceleration and pressure peaks and positively associated with their durations. In contrast, scalp modulus was positively associated with acceleration and pressure peaks and negatively associated with their durations. These results further confirm the trends exhibited in Figure 5.3 and Figure 5.4.

Table 5.3. Multiple linear regression results for the 5 cm drop height BIPED impacts. Shown are the standardized slope coefficient β_m: for material modulus; β_t: for material thickness), adjusted R^2, and F values for each model and impact location. $p < 0.05$ indicates statistical significance.

Dependent Variable		Front		Right Side		Back	
		Value	*p*	Value	*p*	Value	*p*
Acceleration Peak (g)	β_m	0.20	(.008)	0.20	(.006)	0.35	(.000)
	β_t	-0.83	(.000[a])	-0.83	(.000)	-0.80	(.000)
	R^2	0.74		0.76		0.77	
	F	71.62	(.000)	77.85	(.000)	88.11	(.000)
Acceleration duration (ms)	β_m	-0.17	(.012)	-0.35	(.000)	-0.22	(.000)
	β_t	0.87	(.000)	0.81	(.000)	0.90	(.000)
	R^2	0.80		0.82		0.86	
	F	97.50	(.000)	115.77	(.000)	161.23	(.000)
Pressure peak (kPa)	β_m	0.04	(**.669**)	-0.03	(**.730**)	0.34	(.000)
	β_t	-0.79	(.000)	-0.82	(.000)	-0.85	(.000)
	R^2	0.61		0.66		0.86	
	F	38.57	(.000)	49.44	(.000)	154.27	(.000)
Pressure duration (ms)	β_m	-0.18	(.002)	-0.20	(.000)	-0.30	(.000)
	β_t	0.90	(.000)	0.93	(.000)	0.89	(.000)
	R^2	0.85		0.93		0.89	
	F	144.19	(.000)	352.31	(.000)	209.65	(.000)

a. 0.000 indicates $p < 0.001$.

Table 5.4. Multiple linear regression results for the 19.5 cm drop height BIPED impact tests. Shown are the Standardized slope coefficient β_m: for material modulus; β_t: for material thickness), adjusted R^2, and F values for each model and impact location. p < 0.05 indicates statistical significance.

Dependent Variable		Front		Right Side		Back	
		Value	*p*	Value	*p*	Value	*p*
Acceleration Peak (g)	β_m	-0.11	(**0.283**)	-0.24	(**0.059**)	-0.065	(**0.616**)
	β_t	-0.74	(0.000[a])	-0.47	(0.000)	-0.477	(0.001)
	R^2	0.54		0.25		0.20	
	F	29.53	(0.000)	8.93	(0.001)	7.14	(0.002)
Acceleration duration (ms)	β_m	0.012	(**0.884**)	0.07	(**0.432**)	-0.04	(**0.578**)
	β_t	0.834	(0.000)	0.80	(0.000)	0.88	(0.000)
	R^2	0.68		0.62		0.77	
	F	53.61	(0.000)	40.34	(0.000)	83.06	(0.000)
Pressure peak (kPa)	β_m	-0.11	(**0.287**)	-0.23	(**0.093**)	0.09	(**0.440**)
	β_t	-0.72	(0.000)	-0.34	(0.014)	-0.65	(0.000)
	R^2	0.50		0.13		0.41	
	F	25.90	(0.000)	4.70	(0.014)	17.87	(0.000)
Pressure duration (ms)	β_m	-0.08	(**0.143**)	-0.10	(**0.204**)	-0.139	(**0.062**)
	β_t	0.93	(0.000)	0.84	(0.000)	0.857	(0.000)
	R^2	0.87		0.70		0.74	
	F	158.62	(0.000)	55.64	(0.000)	70.13	(0.000)

a. 0.000 indicates p < 0.001.

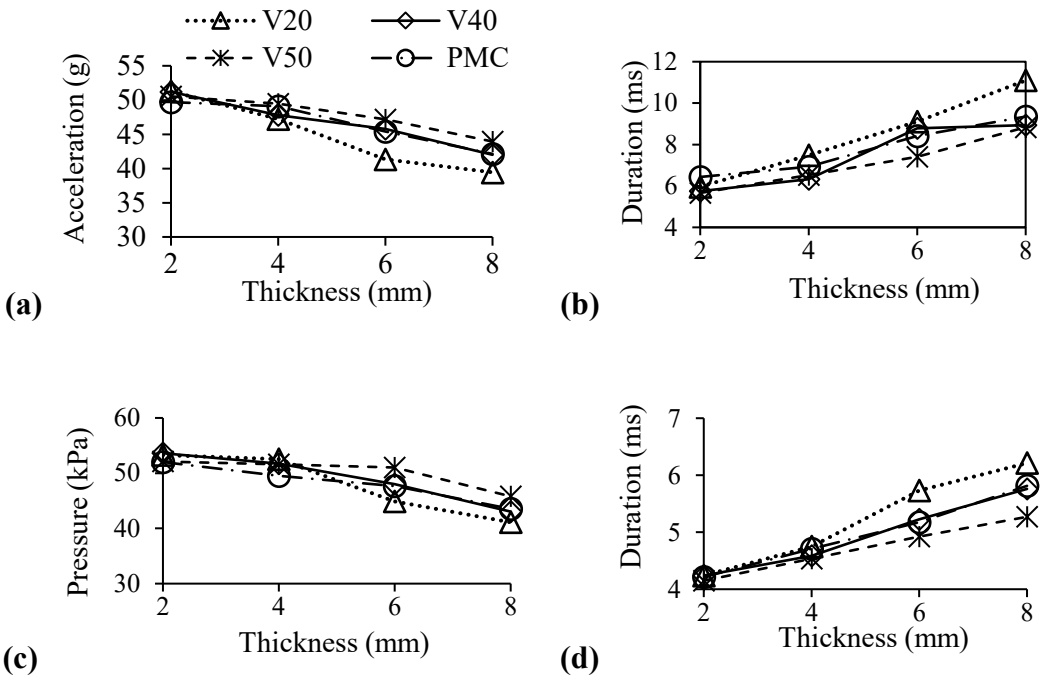

Figure 5.3. Peak and duration mean values for the acceleration (a & b) and pressure (c & d) in the BIPED front impacts from the 5 cm drop height. Shown are the values varying with the pad thickness for the BIPED with each material of scalp pads. "V20", "V40", "V50", and "PMC" represent impacts with pad materials of Vytaflex20, Vytaflex40, Vytaflex50, and PMC746, respectively.

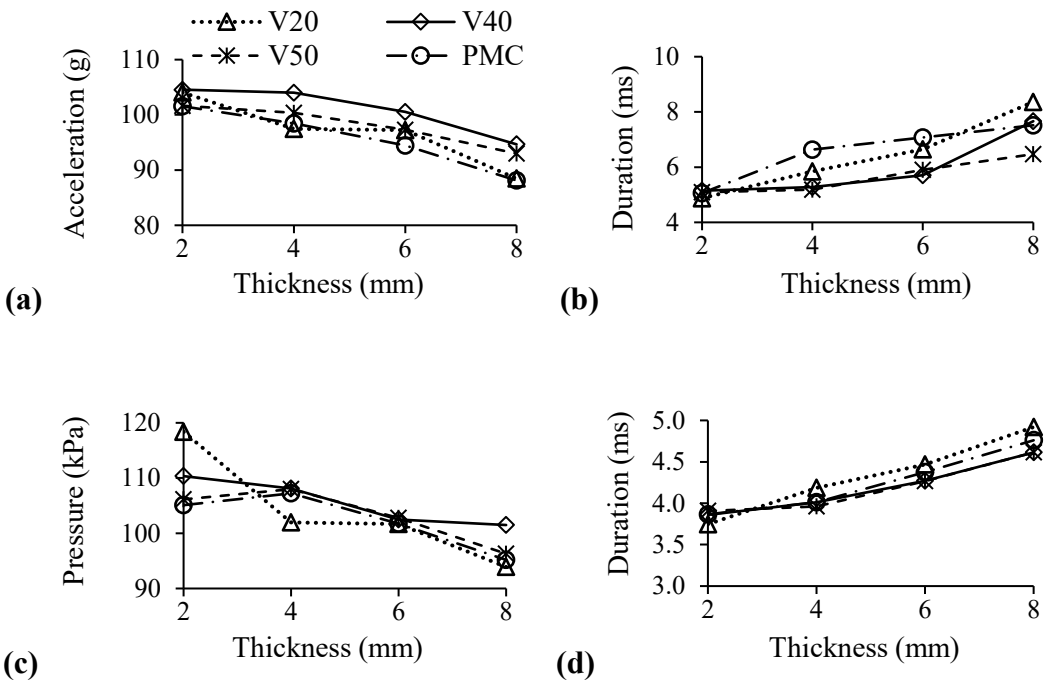

Figure 5.4. Peak and duration mean values for the acceleration (a & b) and coup pressure (c & d) in the 19.5 cm drop height BIPED front impacts. Shown are the values varying with the pad thickness for the BIPED with each material of scalp pads. "V20", "V40", "V50", and "PMC" represent impacts with pad materials of Vytaflex20, Vytaflex40, Vytaflex50, and PMC746, respectively.

Table 5.5. Total CORA ratings of the BIPED accelerations from the 19.5 cm drop height for each impact location (Front, Side, and Back) and the average ratings (Ave.) across the three impact locations. The presented data are results for each scalp pad with varying thicknesses and materials.

Thickness (mm)	Material	Front	Side	Back	Ave.	Material	Front	Side	Back	Ave.
2	Vytflex20	0.67	0.74	0.61	0.67	Vytflex40	0.70	0.78	0.58	0.69
4	Vytflex20	0.58	0.67	0.61	0.62	Vytflex40	0.67	0.74	0.57	0.66
6	Vytflex20	0.49	0.52	0.56	0.52	Vytflex40	0.57	0.64	0.54	0.58
8	Vytflex20	0.39	0.38	0.49	0.42	Vytflex40	0.48	0.45	0.53	0.49
2	Vytflex50	0.67	0.78	0.60	0.68	PMC746	0.69	0.69	0.61	0.66
4	Vytflex50	0.69	0.79	0.57	0.68	PMC746	0.53	0.64	0.56	0.58
6	Vytflex50	0.54	0.66	0.55	0.58	PMC746	0.54	0.58	0.55	0.55
8	Vytflex50	0.50	0.48	0.54	0.51	PMC746	0.47	0.47	0.51	0.48

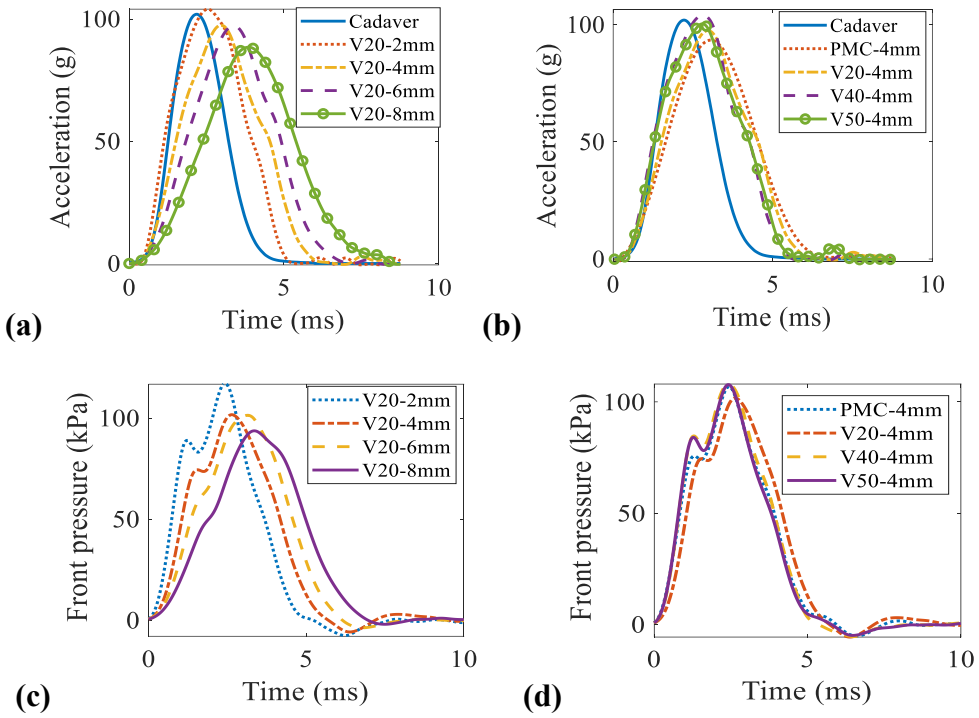

Figure 5.5. Mean acceleration and front pressure profiles for the BIPED frontal impacts from the 19.5 cm height: (a) accelerations for Vytaflex20 pads of different thicknesses in comparison with the mean cadaver acceleration from tests of the same impact velocity [133], (b) accelerations for 4 mm pads made with Vytaflex20 (V20), Vytaflex40 (V40), Vytaflex50 (V50), and PMC746 (PMC), and the cadaver acceleration [133], (c) front pressures for Vytaflex20 scalp pads, (d) front pressures for 4 mm of scalp pads made from the four materials.

Acceleration and pressure profiles (Figure 5.5) also show that in this study the scalp pad thickness had a much stronger influence on the impact responses than the choice of pad material. Figure 5.5(a) depicts a comparison between the mean acceleration profiles across repeated tests with Vytaflex20 scalp pads of different thicknesses and average cadaveric data from impacts of the same velocity [133]. The results indicate that the biofidelity of a given material decreased with increasing scalp pad thickness. Figure 5.5(b) depicts a comparison

between the mean acceleration profiles for tests with 4 mm scalp pads made from different materials and cadaveric data. The plots suggest that the selected materials have a slight effect on biofidelity. Similarly, the coup pressure profiles exhibit variations with the pad thickness as the pulse durations increased with increased thickness (Figure 5.5(c)). However, in Figure 5.5(d), only the pressure profile for Vytaflex20 shows a broader duration than the other profiles while the profiles for the other three materials are visually indistinguishable. There are no cadaveric studies on the pressure with a comparable loading scenario to evaluate the influence on biofidelity of the ICP response though.

Acceleration CORA ratings also confirmed the considerable influence of the scalp pad thickness on acceleration biofidelity. Figure 5.6 presents CORA ratings plotted against scalp thickness and modulus. When keeping the pad material and impact location fixed, CORA ratings generally decreased with increased pad thickness (Figure 5.6(a)–(c)). In contrast, when keeping the pad thickness and impact location fixed there was generally no monotonic trend in the ratings across the materials (Figure 5.6(d)–(f)). These results agree with the aforementioned observations in Figure 5.5. As reported in Table 5.5, the ratings for the 2 mm of thickness across materials range from 0.67–0.70, 0.69–0.78, and 0.58–0.61, for the front, side, and back impact, respectively. When the thickness increased to 8 mm, the ratings dropped to 0.39–0.50, 0.38–0.48, and 0.49–0.54, for the three locations, respectively.

Furthermore, data obtained using scalp pads made with Vytaflex40 and Vytaflex50 resulted in similar average CORA ratings with an absolute difference of no more than 0.02 for the four thicknesses. These average ratings were greater than that of the other two materials by up to 0.1. Interestingly, for the Vytaflex40 and Vytaflex50 scalp pads, ratings for the thickness of 2 mm were close to for the 4 mm pad, with an average of 0.66–0.69 across three impact

locations. Overall, scalp pads made from Vytaflex40 and Vytaflex50 with thicknesses of 2 mm and 4 mm exhibited better biofidelity than the other scalp pads.

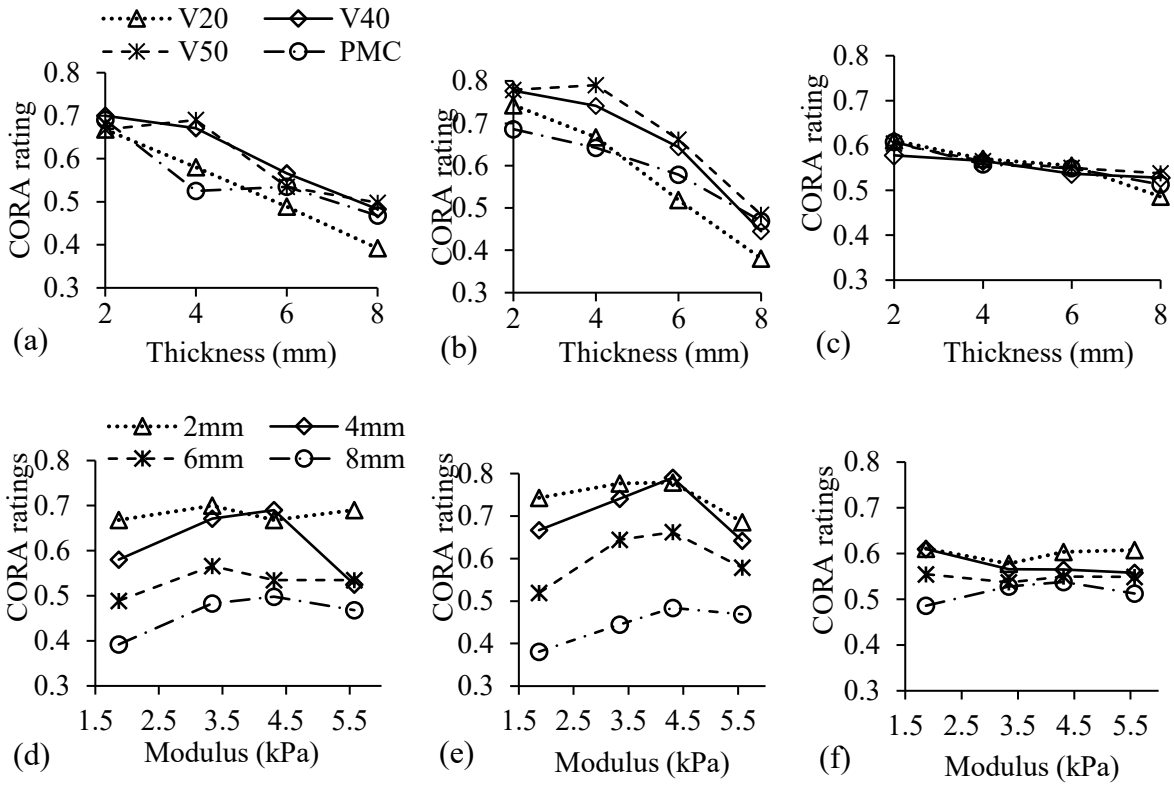

Figure 5.6. CORA ratings of the BIPED accelerations from the 19.5 cm drop impacts. Shown are the ratings for each scalp pad plotted against the scalp thickness and modulus for the front (a & d), side (b & e), and back impact location (c & f).

5.4 Discussion

This study evaluated the influence of surrogate scalp modulus and thickness on head impact responses including acceleration and intraparenchymal pressure, using a surrogate head-brain model. The results indicated that scalp thickness had a major influence on the acceleration and pressure for all the impact scenarios, whereas the scalp modulus for the

materials selected in this study was only influential for the 5 cm drop height impacts. An optimal scalp pad thickness and material could be identified based on the influence.

According to impact dynamics theory, impact responses are governed by the mass, stiffness, and damping of the system being impacted [181]. In particular, increasing the stiffness of a system increases the peak and decreases the duration of the impact response [181]. Based on classic elasticity theory, the stiffness of a pad increases with increased modulus and decreased thickness [182]. Therefore, the observed relationship between the impact response and the scalp modulus and thickness for the 5 cm drop height impacts agrees with the principles of impact dynamics. The thickness of the pads exhibited a significant influence on the impact responses of the headform since thickness determines the deformation potential of the pad and the amount of energy it can absorb.

The scalp modulus did not affect the impact responses for the 19.5 cm drops. This may be explained by the nonlinearity and rate dependency of the scalp material properties. Figure 5.7(a) and Figure 5.7(d) present the stress-strain and modulus-strain curves of the surrogate scalp materials chosen for this study. The modulus at each strain was calculated by inserting the strains into the first derivative with respect to the strain of the polynomial regression function of the stress-strain data. We chose the 4th order polynomial regression of the stress-strain data because the mean squared error (MSE, MSE= $\frac{1}{n}\sum_i^n(Y_i - \hat{Y}_i)^2$) between the measured stress Y_i and model predicted stress $\hat{Y}_i$ has negligible change after the 4th order for all the materials. Figure 5.7(b) and Figure 5.7(c) display examples of the 4th order polynomial and the MSE versus the order of the polynomial regressions for stress-strain data of the Vytaflex50 sample. The modulus of the selected materials increases with strain (Figure 5.7(d)).

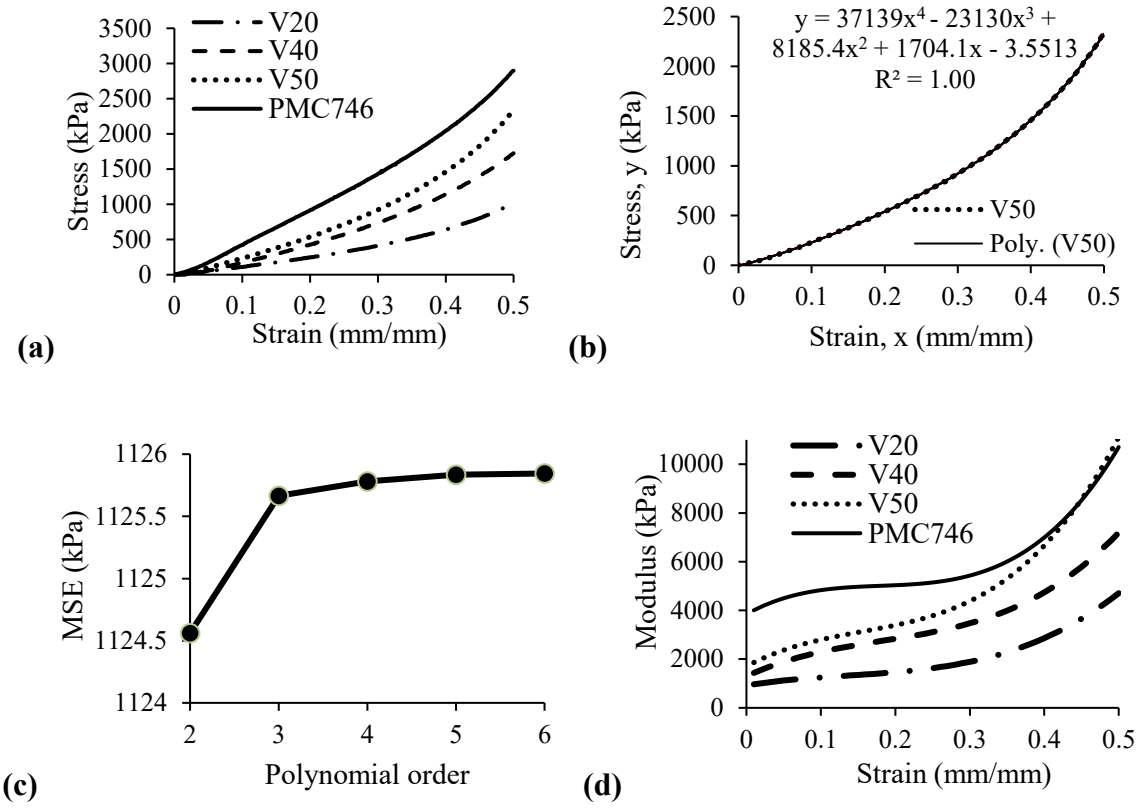

Figure 5.7. (a)The stress plotted against the strain for the pad material samples under the compression load at a strain rate of 0.013/s. (b) An example showing the 4th order polynomial regression model of the Vytaflex50 stress-strain data. (c) The MSE versus polynomial order for the Vytaflex50 stress-strain data. (d) The modulus plotted against the strain for the pad material samples.

The mechanical behavior of rubber is also dependent on the strain rate [183]. Drops from the 19.5 cm height resulted in larger scalp deformations and a larger strain rate than the 5 cm drops. The selected scalp materials may stiffen up to a similar effective stiffness during the 19.5 cm height drops due to the combined effect of the strain and strain rate. Furthermore, PMC746 may not experience similar strain and rate effects as the Vytaflex series. As seen in Figure 5.7(b), although PMC746 is the stiffest material at the initial strain, it becomes less stiff

than Vytaflex50 at a strain of 0.5. Thus, the modulus used for the MLR analysis may not be indicative of the effective stiffness for the high-height drops. Furthermore, while the selected materials had a large hardness range (Shore A 20 to 60), the modulus range was relatively small (1.87–5.57 MPa), as the tested materials were all urethane rubbers.

The head linear acceleration results obtained in this study have some similarities as well as differences with previous studies. Dropping a magnesium headform covered with and without a porcine scalp onto a polyurethane rubber anvil at an impact velocity of 5 m/s, Trotta et al. found that adding a scalp reduced the peak linear acceleration by 17–26% and increased the impact duration by 11–17% [167]. This trend of change agrees with the present study for peak acceleration decreasing and duration increasing with increased pad thickness. The extent of the change is incomparable due to the different impact conditions between the two studies. Another previous study dropped a deformable skull and brain structure from a drop height of 20 cm onto a padded steel anvil. Two different paddings were tested: the Hybrid III scalp and a stiffer rubber padding [168]. The peak acceleration (120 g) obtained for the stiffer rubber material was double that of the Hybrid III scalp (60 g) [168]. In the present study, the peak accelerations (53–89 g) overlap with the aforementioned study for similar impact conditions, but the acceleration differences between pad materials for the same pad thickness were smaller (<30%) [168]. One possible reason for this discrepancy is that the stiffness difference between the Hybrid III scalp and the stiffer pad was greater than the stiffness difference between the pads in our study. Another reason may be that the thickness of the scalp pads in the reported study (12 mm) is greater than the scalp thicknesses in our study (2 to 8 mm).

The influence of the scalp modulus on impact responses tends to decrease with reduced thickness. This is demonstrated in Figure 5.3(a) and Figure 5.4(a) where the maximal

difference of peak accelerations across materials is generally lower for lower scalp thicknesses. This phenomenon is likely because of the nonlinearity of the rubber scalp materials. Compared to thicker scalps, the thinner scalps would have a greater strain and a greater impact stiffness for the same loading force. Changing the scalp modulus may have less effect on the head impact stiffness for thinner scalp pads, thus the influence of scalp materials on head acceleration peaks is also lower for the thinner scalp.

Trends in CORA ratings can be used to inform improvements in the biofidelity of the BIPED. The variation of CORA ratings with scalp material and thickness were similar for the front (Figure 5.6(a) and (d)) and side impacts (Figure 5.6(b) and (e)), but not for the back impact (Figure 5.6(c) and (f)). The data from back impacts exhibited an abnormal trend that may be caused by inconsistencies in positioning the BIPED skull on the gimbal. For back impacts, the BIPED tended to slide and sink, contributing to the uncertainty of drop heights. For the front and side impacts, the ratings decreased with the pad thickness but tended to plateau at lower thickness. Specifically, the ratings obtained for the Vytaflex40 and Vytaflex50 plateaued at a thickness below 4 mm. This phenomenon indicates that scalp thickness has a negligible effect on the head responses when the scalp is substantially thin. This phenomenon can be attributed to the nonlinearity of the scalp pad as discussed in the previous paragraph.

Based on the above considerations, selecting Vytaflex40 or Vytaflex50 at thicknesses between 2 and 4 mm may best improve the biofidelity of the current BIPED. The original BIPED scalp was made with Vytaflex20 with a nominal thickness of 6 mm. Decreasing the scalp thickness of the BIPED to 2–4 mm and changing the Vytaflex 20 to Vytaflex 40 or Vytaflex 50 can decrease the impact pulse durations by 18% on average and increase the CORA ratings by 30%. The improved CORA ratings (0.66–0.69) were approaching the

reported rating threshold (0.7) for a good biofidelity level. Given that Vytaflex 40 is more flexible for installing and removing the scalp and a thicker scalp is likely more durable, a favorable suggestion for modifying the BIPED scalp is using Vytaflex 40 and decreasing the thickness to 4 mm based on the outcomes of this study.

This study has several primary limitations. The evaluated scalp surrogates were all made of urethane rubbers due to their durability and flexibility for use. For a more comprehensive study, other materials used to model the scalp such as silicone rubbers [19], should also be considered. The mechanical properties of viscoelastic rubbers are dependent on strain magnitude and rate [183]. Consequently, the modulus used in the MLR may not be an accurate representation of the material properties at impact. Nevertheless, the modulus measured under uniform conditions provides a relative comparison of the selected materials. Another limitation is that impact heights in this study were not as high as that might cause head injuries. A study of free-fall dropping cadaver heads onto a rigid plate reported skull fractures for the drop height of 33 cm [184]. The heights in our study allowed a comparison with a previous cadaver study while guaranteeing the integrity of the head for future use. Comparing the results for the two drop heights used in our study, the magnitudes of the standardized beta coefficients decreased with increasing height, whereas the signs of the significant beta coefficients were the same. Thus, the influence of the scalp for higher drops would be expected to be similar but less significant compared to results in the present study. Moreover, we used scalp pads instead of whole scalps and added a mass to compensate for the scalp mass. The added mass would possibly affect the realism of the moment of inertia and the kinematic responses, but the resulted discrepancy would likely not affect the relative comparison between scalp pads. Additionally, the linear accelerations in the current study were obtained from the

impact force, which may be slightly different from the accelerations at the head's center of mass, due to the non-rigidity of the headform. However, the accelerations obtained from the force allow for relative comparisons of the scalp pads' influence with the intention of achieving biofidelic responses. Lastly, our findings are based on impact tests with the specific BIPED skull and brain. As described earlier, head stiffness is a crucial factor in head impact responses and depends predominantly on the stiffness of the skull and scalp. The BIPED used in this study had skull modulus and thickness similar to those of cadaver heads. Our results can therefore be applied to the scalp selection for skull surrogates that have similar stiffness as the BIPED or the human skull.

5.5 Conclusion

This study evaluated the effect of the surrogate scalp material and thickness on the impact responses of a head-brain model to improve its biofidelity. Based on the selected materials and thicknesses, the results suggested that the scalp thickness had a major influence while the modulus showed a minor to insignificant effect. Furthermore, it was found that decreasing the scalp thickness of the BIPED to 2–4 mm and changing the Vytaflex 20 to Vytaflex 40 or Vytaflex 50 can increase the kinematic CORA ratings by 30% to approach the threshold for good biofidelity. With further improvement, the BIPED may be a powerful tool to extend the understanding of head injury mechanisms and to improve the assessment method of protective headgear. The study also has important implications for selecting appropriate surrogate scalps in the future design of physical and numerical head models.

Chapter 6 Conclusions and Future Work

This chapter summarizes the key findings in relation to the research aims and discusses the value and contributions of this research. It also suggests future work worthy of investigation.

6.1 Conclusions

This thesis aimed to characterize the impact responses and refine the design of the BIPED head model to contribute to the development of a biofidelic and repeatable headform capable of replicating both global head kinematics and ICP in blunt impact. Headforms are crucial tools used in the research of head injury mechanisms and for the assessment of head protective gear. Today's commercially available headforms are limited to replicating only head kinematics or mechanics measurable on the outer surface of the skull. Intracranial responses are closely related to TBIs, but there is a lack of validated headforms containing intracranial simulants to realistically replicate intracranial mechanics. This thesis provided insights into the characteristics of the impact responses and design factors of the BIPED which has intracranial simulants. This thesis also provided a refining method that can improve the kinematic biofidelity of the BIPED to approach a good level for blunt impact. The thesis consists of three studies which are summarized below.

(1) Characterization of the Kinematic Biofidelity and Inter-test Repeatability of Acceleration and Intraparenchymal Pressure of the BIPED

This study presented in Chapter 3 evaluated the acceleration biofidelity and repeatability of the acceleration and IPP from drop experiments. The CORA ratings of the acceleration time

histories for the BIPED were slightly lower than for the Hybrid III head. The repeatability of acceleration and IPP was acceptable with COVs below the acceptable threshold of 10%. A major limitation of the BIPED was that its acceleration pulse durations were approximately 50% longer than those from cadaveric data. Based on the analysis of head impact stiffness, the study suggested that the longer pulse durations of the BIPED can be associated with its lower stiffness. This study was an important step in understanding the response characteristics and associated design factors of a comprehensive headform. The results have implications for further refinements of the skull or scalp structure toward a biofidelic and repeatable headform. This study is also the first that rigorously validated the biofidelity and repeatability considering multiple features of head kinematics including peaks, durations, and time histories, which can be a reference for the future validation of human surrogates.

(2) Characterization of the ICP Biofidelity and Kinematic and ICP Inter-test Repeatability of the BIPED

The study presented in Chapter 4 conducted pendulum impacts on the BIPED, aiming to further characterize its ICP biofidelity as well as the repeatability of measurements including linear accelerations and angular rates along three axes, IPP, and CSFP. The front ICP peaks were within the range of cadaveric data. CORA ratings of the front CSFP time histories (0.68–0.72) demonstrated good biofidelity. Moreover, the front and back CSFP versus linear accelerations had similar linear trends to cadaveric data. However, the side CSFP peaks were 28.7–92.1% greater than cadaveric data, which warrants further investigation. The kinematics and ICP demonstrated acceptable repeatability with COVs generally being less than 10%. Considering the similarities of the coup ICP to the cadaveric data, the BIPED can be considered acceptable for the study of coup pressure in frontal impacts. This study demonstrated the great

potential of using the BIPED in blunt impact considering its repeatability and its promise in ICP biofidelity. The findings also inform the future work of refining the intracranial components to improve the ICP biofidelity.

(3) Improving the BIPED Biofidelity by Refining the Surrogate Scalp

Since one of the major limitations of the BIPED was related to its long acceleration pulse durations, the refinement of the BIPED focused on increasing the scalp stiffness to reduce the pulse durations and improve the overall biofidelity. The study verified that the surrogate scalp significantly affects impact responses. While the selected materials exhibited a relatively minor effect on head acceleration and IPP responses, scalp thickness was shown to have a major effect. This study identified a refinement method of the BIPED scalp that can increase the overall biofidelity ratings (0.66–0.69) of the accelerations by 30% to approach the good biofidelity threshold (0.7). This refinement can also improve the ICP biofidelity as the scalp has a similar effect on ICP durations.

Overall, this thesis work characterized both the kinematics and ICP responses of a physical head-brain model and provided a refining method to effectively improve its biofidelity. With ongoing improvement, this head model can be a valuable tool for head injury research and safety gear assessment by extending the traditional methods of measuring only kinematics to both kinematics and intracranial mechanics. Testing with this new tool may shed new light on understanding head injuries and advance the assessment method of safety gear. Furthermore, this thesis provided insight into the characterization method of headforms, highlighting the need for considering time histories rather than pure peaks. Finally, the thesis

found the statistically significant influence of the scalp on head impact responses, which can inform the future development of physical and numerical head models.

6.2 Future work

The research presented in this thesis is a crucial step toward a biofidelic and repeatable comprehensive headform for use in head injury research and safety gear assessment. Further work that can be done as a continuation of the present work is listed as follows:

(1) The design factors on the intracranial responses require further studies to improve the BIPED ICP biofidelity. While the BIPED front ICP peaks were close to cadaveric data, the BIPED side ICP peaks were greater. This study has discussed the possible causes of this phenomenon, but further work is required to identify the causes and explore modifications to improve the ICP biofidelity without reducing the kinematic biofidelity.

(2) The biofidelity and repeatability of the BIPED in other impact scenarios can be further studied. The characterization of the BIPED biofidelity was limited to two typical impact paradigms (i.e., the drop and the pendulum impacts), and the impacts were limited to typical impact angles and locations for each paradigm. It should be noted that head impact responses vary with the impact angles, locations on the head, and head positions in different impact paradigms. Therefore, the results found in one impact scenario may not be valid for other scenarios. Particularly, we only evaluated translational impacts on the forehead of the BIPED for the characterization of the ICP biofidelity due to the lack of cadaveric data. Thus, whether the ICP would be biofidelic for side translational impacts or drop impacts is unknown. Future work can characterize the biofidelity of the BIPED for impact scenarios beyond this thesis if cadaveric data are available for comparison.

(3) Whether refining skull materials can improve the biofidelity of the BIPED could be studied. This study found that the effect of the scalp on the BIPED biofidelity is limited when the scalp thickness is as low as 2 mm. Since the BIPED skull modulus and thickness belong to the low region in the range of reported cadaver skull data, further work to refine the skull may improve the biofidelity to replicate human responses more accurately.

(4) Future studies should evaluate the potential capability of using the BIPED in helmet tests. The headform can be a valuable tool in the design and assessment of safety devices. Headforms measuring ICP in addition to the kinematics measured by traditional headforms may advance the method of assessing helmets' protective performance against TBIs. Thus, future work could evaluate the repeatability of the BIPED when donned with a helmet and explore advancing the helmet assessment with this new testing equipment once validated.

Bibliography

[1] J. R. Crandall, K. Bhalla, and N. Madeley, 'Designing road vehicles for pedestrian protection', *BMJ*, vol. 324, no. 7346, pp. 1145–1148, May 2002, doi: 10.1136/bmj.324.7346.1145.

[2] C. S. Sahler and B. D. Greenwald, 'Traumatic Brain Injury in Sports: A Review', *Rehabil. Res. Pract.*, vol. 2012, pp. 1–10, 2012, doi: 10.1155/2012/659652.

[3] Canadian Institute for Health Information, 'Head Injuries in Canada: A Decade of Change (1994-1995 to 2003-2004)', 2006.

[4] Public Health Agency of Canada, 'Injury in review, 2020 edition: Spotlight on traumatic brain injuries across the life course', Nov. 19, 2020. https://www.canada.ca/en/public-health/services/injury-prevention/canadian-hospitals-injury-reporting-prevention-program/injury-reports/2020-spotlight-traumatic-brain-injuries-life-course.html (accessed Sep. 02, 2022).

[5] G. Ilie *et al.*, 'Associations between self-reported lifetime history of traumatic brain injuries and current disability assessment in a population sample of Canadian adults', *PLOS ONE*, vol. 13, no. 1, p. e0188908, Jan. 2018, doi: 10.1371/journal.pone.0188908.

[6] C. A. Taylor, J. M. Bell, M. J. Breiding, and L. Xu, 'Traumatic Brain Injury–Related Emergency Department Visits, Hospitalizations, and Deaths — United States, 2007 and 2013', *MMWR Surveill. Summ.*, vol. 66, no. 9, pp. 1–16, Mar. 2017, doi: 10.15585/mmwr.ss6609a1.

[7] J. Daugherty, D. Waltzman, K. Sarmiento, and L. Xu, 'Traumatic Brain Injury–Related Deaths by Race/Ethnicity, Sex, Intent, and Mechanism of Injury — United States, 2000–2017', *Morb. Mortal. Wkly. Rep.*, vol. 68, no. 46, pp. 1050–1056, Nov. 2019, doi: 10.15585/mmwr.mm6846a2.

[8] CDC Injury Center, 'Traumatic Brain Injury', Mar. 21, 2022. http://www.cdc.gov/traumaticbraininjury/data/index.html (accessed Sep. 02, 2022).

[9] E. Finkelstein, P. S. Corso, and T. R. Miller, 'The Incidence and Economic Burden of Injuries in the United States', *J. Epidemiol. Community Health*, vol. 61, no. 10, p. 926, Oct. 2007, doi: 10.1136/jech.2007.059717.

[10] M. C. Dewan *et al.*, 'Estimating the global incidence of traumatic brain injury', *J. Neurosurg.*, vol. 130, no. 4, pp. 1080–1097, Apr. 2018, doi: 10.3171/2017.10.JNS17352.

[11] J. R. Crandall *et al.*, 'Human surrogates for injury biomechanics research', *Clin. Anat.*, vol. 24, no. 3, pp. 362–371, 2011, doi: 10.1002/ca.21152.

[12] B. R. Cobb, A. M. Zadnik, and S. Rowson, 'Comparative analysis of helmeted impact response of Hybrid III and National Operating Committee on Standards for Athletic Equipment headforms', *Proc. Inst. Mech. Eng. Part P J. Sports Eng. Technol.*, vol. 230, no. 1, pp. 50–60, Mar. 2016, doi: 10.1177/1754337115599133.

[13] S. Ji *et al.*, 'Parametric Comparisons of Intracranial Mechanical Responses from Three Validated Finite Element Models of the Human Head', *Ann. Biomed. Eng.*, vol. 42, no. 1, pp. 11–24, Jan. 2014, doi: 10.1007/s10439-013-0907-2.

[14] E. G. Takhounts, R. H. Eppinger, J. Q. Campbell, R. E. Tannous, E. D. Power, and L. S. Shook, 'On the Development of the SIMon Finite Element Head Model', presented at the 47th Stapp Car Crash Conference (2003), San Diego, California, United States, Oct. 2003, pp. 2003-22–0007. doi: 10.4271/2003-22-0007.

[15] B. Knowles, 'A Laboratory Study on the Ability of Head Kinematics to Predict Brain Strains in Helmeted Head Impacts', Ph.D., University of Alberta, Edmonton, Alberta, Canada, 2018. doi: 10.7939/R3D795S6P.

[16] S. Ouellet and M. Philippens, 'The multi-modal responses of a physical head model subjected to various blast exposure conditions', *Shock Waves*, vol. 28, no. 1, pp. 19–36, Jan. 2018, doi: 10.1007/s00193-017-0771-3.

[17] C. J. Freitas, J. T. Mathis, N. Scott, R. P. Bigger, and J. MacKiewicz, 'Dynamic Response Due to Behind Helmet Blunt Trauma Measured with a Human Head Surrogate', *Int. J. Med. Sci.*, vol. 11, no. 5, pp. 409–425, 2014, doi: 10.7150/ijms.8079.

[18] S. Fujiwara, Y. Yanagida, and Y. Mizoi, 'Impact-induced intracranial pressure caused by an accelerated motion of the head or by skull deformation; an experimental study using physical models of the head and neck, and ones of the skull', *Forensic Sci. Int.*, vol. 43, no. 2, pp. 159–169, Oct. 1989, doi: 10.1016/0379-0738(89)90132-1.

[19] N. Petrone, G. Carraro, S. D. Castello, L. Broggio, A. Koptyug, and M. Bäckström, 'A Novel Instrumented Human Head Surrogate for the Impact Evaluation of Helmets', *Multidiscip. Digit. Publ. Inst. Proc.*, vol. 2, no. 6, p. 269, 2018, doi: 10.3390/proceedings2060269.

[20] S. Fujiwara, Y. Yanagida, and Y. Mizoi, 'Impact-induced intracranial pressure caused by an accelerated motion of the head or by skull deformation; an experimental study using physical models of the head and neck, and ones of the skull', *Forensic Sci. Int.*, vol. 43, no. 2, pp. 159–169, 1989.

[21] N. Petrone *et al.*, 'Feasibility of using a novel instrumented human head surrogate to measure helmet, head and brain kinematics and intracranial pressure during multidirectional impact tests', *J. Sci. Med. Sport*, pp. S78–S84, May 2019, doi: 10.1016/j.jsams.2019.05.015.

[22] S. Ouellet, A. Bouamoul, R. Gauvin, J. S. Binette, K. V. Williams, and L. Martineau, 'Development of a biofidelic head surrogate for blast-induced traumatic brain injury assessment', in *Proceedings of the Personal Armor System Symposium*, Neuremberg, Germany, Sep. 2012, pp. 1–11.

[23] K. Miller, Ed., *Biomechanics of the Brain*. in Biological and Medical Physics, Biomedical Engineering. New York: Springer-Verlag, 2011. doi: 10.1007/978-1-4419-9997-9.

[24] B. Medical, 'Medical gallery of Blausen Medical 2014', *WikiJournal Med.*, vol. 1, no. 2, 2014, doi: 10.15347/wjm/2014.010.

[25] Parviz Janfaza M.D, *Surgical Anatomy of the Head and Neck*, vol. First Harvard University Press edition. Cambridge, Mass: Harvard University Press, 2011. [Online]. Available: https://login.ezproxy.library.ualberta.ca/login?url=https://search.ebscohost.com/login.aspx?direct=true&db=e000xna&AN=713932&site=ehost-live&scope=site

[26] P. Oltulu, B. Ince, N. Kokbudak, S. Findik, and F. Kilinc, 'Measurement of epidermis, dermis, and total skin thicknesses from six different body regions with a new ethical histometric technique', *Turk. J. Plast. Surg.*, vol. 26, no. 2, p. 56, Apr. 2018, doi: 10.4103/tjps.TJPS_2_17.

[27] A. J. Lupin and R. J. Gardiner, 'Scalp thickness in the temporal region: its relevance to the development of cochlear implants', *Cochlear Implants Int.*, vol. 2, no. 1, pp. 30–38, Mar. 2001, doi: 10.1179/cim.2001.2.1.30.

[28] K. Chopra *et al.*, 'A Comprehensive Examination of Topographic Thickness of Skin in the Human Face', *Aesthet. Surg. J.*, vol. 35, no. 8, pp. 1007–1013, Nov. 2015, doi: 10.1093/asj/sjv079.

[29] S. i. Alekseev, A. a. Radzievsky, M. k. Logani, and M. c. Ziskin, 'Millimeter wave dosimetry of human skin', *Bioelectromagnetics*, vol. 29, no. 1, pp. 65–70, 2008, doi: 10.1002/bem.20363.

[30] J. W. Melvin, J. H. McElhaney, and V. L. Roberts, 'Development of a Mechanical Model of the Human Head — Determination of Tissue Properties and Synthetic Substitute Materials', *SAE Trans.*, vol. 79, pp. 2685–2694, 1970, Accessed: Feb. 22, 2022. [Online]. Available: https://www.jstor.org/stable/44723768

[31] L. Falland-Cheung *et al.*, 'Mechanical properties of the human scalp in tension', *J. Mech. Behav. Biomed. Mater.*, vol. 84, pp. 188–197, Aug. 2018, doi: 10.1016/j.jmbbm.2018.05.024.

[32] J. E. Galford and J. H. McElhaney, 'A viscoelastic study of scalp, brain, and dura', *J. Biomech.*, vol. 3, no. 2, pp. 211–221, Mar. 1970, doi: 10.1016/0021-9290(70)90007-2.

[33] A. Ní Annaidh, K. Bruyère, M. Destrade, M. D. Gilchrist, and M. Otténio, 'Characterization of the anisotropic mechanical properties of excised human skin', *J. Mech. Behav. Biomed. Mater.*, vol. 5, no. 1, pp. 139–148, Jan. 2012, doi: 10.1016/j.jmbbm.2011.08.016.

[34] A. Trotta and A. Ní Annaidh, 'Mechanical characterisation of human and porcine scalp tissue at dynamic strain rates', *J. Mech. Behav. Biomed. Mater.*, vol. 100, p. 103381, Dec. 2019, doi: 10.1016/j.jmbbm.2019.103381.

[35] D. Sahoo, C. Deck, and R. Willinger, 'Development and validation of an advanced anisotropic visco-hyperelastic human brain FE model', *J. Mech. Behav. Biomed. Mater.*, vol. 33, pp. 24–42, May 2014, doi: 10.1016/j.jmbbm.2013.08.022.

[36] S. Kleiven and H. von Holst, 'Consequences of head size following trauma to the human head', *J. Biomech.*, vol. 35, no. 2, pp. 153–160, Feb. 2002, doi: 10.1016/S0021-9290(01)00202-0.

[37] D. De Kegel, ‘Tissue-Level Tolerance Criteria for Crash-Related Head Injuries: A Combined Experimental and Numerical Approach’, Nov. 2018, Accessed: Feb. 23, 2022. [Online]. Available: https://lirias.kuleuven.be/2302462

[38] C. Jacquemoud, K. Bruyere-Garnier, and M. Coret, ‘Methodology to determine failure characteristics of planar soft tissues using a dynamic tensile test’, *J. Biomech.*, vol. 40, no. 2, pp. 468–475, Jan. 2007, doi: 10.1016/j.jbiomech.2005.12.010.

[39] J. Ruan and P. Prasad, ‘The Effects of Skull Thickness Variations on Human Head Dynamic Impact Responses’, SAE International, Warrendale, PA, SAE Technical Paper 2001-22–0018, Nov. 2001. doi: 10.4271/2001-22-0018.

[40] J. H. McElhaney, J. L. Fogle, J. W. Melvin, R. R. Haynes, V. L. Roberts, and N. M. Alem, ‘Mechanical properties of cranial bone’, *J. Biomech.*, vol. 3, no. 5, pp. 495–511, Oct. 1970, doi: 10.1016/0021-9290(70)90059-X.

[41] J. A. Motherway, P. Verschueren, G. Van der Perre, J. Vander Sloten, and M. D. Gilchrist, ‘The Mechanical Properties of Cranial Bone’, in *6th World Congress of Biomechanics (WCB 2010). August 1-6, 2010 Singapore*, C. T. Lim and J. C. H. Goh, Eds., in IFMBE Proceedings. Berlin, Heidelberg: Springer, 2010, pp. 776–779. doi: 10.1007/978-3-642-14515-5_197.

[42] P. Verschueren *et al.*, ‘Analysis of fracture characteristics of cranial bone for FE modelling’, in *IRCOBI Conference on the Biommechanics of Impacts*, Madrid, Spain, Sep. 2006, p. 4.

[43] J. Rahmoun, A. Auperrin, R. Delille, H. Naceur, and P. Drazetic, ‘Characterization and micromechanical modeling of the human cranial bone elastic properties’, *Mech. Res. Commun.*, vol. 60, pp. 7–14, Sep. 2014, doi: 10.1016/j.mechrescom.2014.04.001.

[44] D. R. Walsh, Z. Zhou, X. Li, J. Kearns, D. T. Newport, and J. J. E. Mulvihill, ‘Mechanical Properties of the Cranial Meninges: A Systematic Review’, *J. Neurotrauma*, vol. 38, no. 13, pp. 1748–1761, Jul. 2021, doi: 10.1089/neu.2020.7288.

[45] J. Ho, Z. Zhou, X. Li, and S. Kleiven, ‘The peculiar properties of the falx and tentorium in brain injury biomechanics’, *J. Biomech.*, vol. 60, pp. 243–247, Jul. 2017, doi: 10.1016/j.jbiomech.2017.06.023.

[46] R. van Noort, M. M. Black, T. R. P. Martin, and S. Meanley, ‘A study of the uniaxial mechanical properties of human dura mater preserved in glycerol’, *Biomaterials*, vol. 2, no. 1, pp. 41–45, Jan. 1981, doi: 10.1016/0142-9612(81)90086-7.

[47] M. G. Richardson and R. N. Wissler, ‘Density of Lumbar Cerebrospinal Fluid in Pregnant and Nonpregnant Humans’, *Anesthesiology*, vol. 85, no. 2, pp. 326–330, Aug. 1996, doi: 10.1097/00000542-199608000-00014.

[48] L. Sakka, G. Coll, and J. Chazal, ‘Anatomy and physiology of cerebrospinal fluid’, *Eur. Ann. Otorhinolaryngol. Head Neck Dis.*, vol. 128, no. 6, pp. 309–316, Dec. 2011, doi: 10.1016/j.anorl.2011.03.002.

[49] I. G. Bloomfield, I. H. Johnston, and L. E. Bilston, ‘Effects of Proteins, Blood Cells and Glucose on the Viscosity of Cerebrospinal Fluid’, *Pediatr. Neurosurg.*, vol. 28, no. 5, pp. 246–251, 1998, doi: 10.1159/000028659.

[50] Y. Luo, Z. Li, and H. Chen, 'Finite-element study of cerebrospinal fluid in mitigating closed head injuries', *Proc. Inst. Mech. Eng. [H]*, vol. 226, no. 7, pp. 499–509, Jul. 2012, doi: 10.1177/0954411912445729.

[51] A. Rycman, S. McLachlin, and D. S. Cronin, 'Comparison of numerical methods for cerebrospinal fluid representation and fluid–structure interaction during transverse impact of a finite element spinal cord model', *Int. J. Numer. Methods Biomed. Eng.*, vol. n/a, no. n/a, p. e3570, doi: 10.1002/cnm.3570.

[52] Y. Luo, Z. Li, and H. Chen, 'Finite-element study of cerebrospinal fluid in mitigating closed head injuries', *Proc. Inst. Mech. Eng. [H]*, vol. 226, no. 7, pp. 499–509, Jul. 2012, doi: 10.1177/0954411912445729.

[53] A. Madhukar, Y. Chen, and M. Ostoja-Starzewski, 'Effect of cerebrospinal fluid modeling on spherically convergent shear waves during blunt head trauma', *Int. J. Numer. Methods Biomed. Eng.*, vol. 33, no. 12, 2017, doi: 10.1002/cnm.2881.

[54] D. D. Blatter *et al.*, 'Quantitative volumetric analysis of brain MR: normative database spanning 5 decades of life.', *Am. J. Neuroradiol.*, vol. 16, no. 2, pp. 241–251, Feb. 1995, Accessed: Feb. 26, 2022. [Online]. Available: http://www.ajnr.org/content/16/2/241

[55] L. Bilston, 'The Skull and Brain : Mechanical Properties of the Brain under Impact', *Military Injury Biomechanics*, Jun. 12, 2017. https://www.taylorfrancis.com/ (accessed Apr. 13, 2020).

[56] K. Miller and K. Chinzei, 'Constitutive modelling of brain tissue: Experiment and theory', *J. Biomech.*, vol. 30, no. 11, pp. 1115–1121, Nov. 1997, doi: 10.1016/S0021-9290(97)00092-4.

[57] G. Franceschini, D. Bigoni, P. Regitnig, and G. A. Holzapfel, 'Brain tissue deforms similarly to filled elastomers and follows consolidation theory', *J. Mech. Phys. Solids*, vol. 54, no. 12, pp. 2592–2620, Dec. 2006, doi: 10.1016/j.jmps.2006.05.004.

[58] S.-C. Lin, S.-J. Shieh, and M. J. Grimm, 'Ultrasonic measurements of brain tissue properties', in *Proc. Of the Symposium of the Centers for Disease Control and Prevention*, 1997, pp. 27–31.

[59] A. Etoh, S. Mitaku, J. Yamamoto, and K. Okano, 'Ultrasonic Absorption Anomaly of Brain Tissue', *Jpn. J. Appl. Phys.*, vol. 33, no. 5S, p. 2874, May 1994, doi: 10.1143/JJAP.33.2874.

[60] L. E. Bilston, 'Brain Tissue Mechanical Properties', in *Biomechanics of the Brain*, K. Miller, Ed., in Biological and Medical Physics, Biomedical Engineering. New York, NY: Springer, 2011, pp. 69–89. doi: 10.1007/978-1-4419-9997-9_4.

[61] M. T. Prange and S. S. Margulies, 'Regional, Directional, and Age-Dependent Properties of the Brain Undergoing Large Deformation', *J. Biomech. Eng.*, vol. 124, no. 2, pp. 244–252, Mar. 2002, doi: 10.1115/1.1449907.

[62] K.-U. Schmitt, P. Niederer, M. Muser, and F. Walz, *Trauma biomechanics*. New York, NY: Springer Berlin Heidelberg, 2010.

[63] L. A. Young, G. T. Rule, R. T. Bocchieri, and J. M. Burns, ‘Biophysical Mechanisms of Traumatic Brain Injuries’, *Semin. Neurol.*, vol. 35, no. 1, pp. 5–11, Feb. 2015, doi: 10.1055/s-0035-1544242.

[64] E. S. Gurdjian, ‘Movements of the brain and brain stem from impact induced linear and angular acceleration.’, *Trans. Am. Neurol. Assoc.*, vol. 95, pp. 248–249, 1970, Accessed: Sep. 04, 2019. [Online]. Available: http://europepmc.org/abstract/med/4998762

[65] L. F. Gabler, J. R. Crandall, and M. B. Panzer, ‘Assessment of Kinematic Brain Injury Metrics for Predicting Strain Responses in Diverse Automotive Impact Conditions’, *Ann. Biomed. Eng.*, vol. 44, no. 12, pp. 3705–3718, Dec. 2016, doi: 10.1007/s10439-016-1697-0.

[66] A. H. S. Holbourn, ‘Mechanics of head injuries’, *The Lancet*, vol. 242, no. 6267, pp. 438–441, Oct. 1943, doi: 10.1016/S0140-6736(00)87453-X.

[67] S. Rowson *et al.*, ‘Rotational Head Kinematics in Football Impacts: An Injury Risk Function for Concussion’, *Ann. Biomed. Eng.*, vol. 40, no. 1, pp. 1–13, Jan. 2012, doi: 10.1007/s10439-011-0392-4.

[68] K. Ono, A. Kikuchi, M. Nakamura, H. Kobayashi, and N. Nakamura, ‘Human head tolerance to sagittal impact reliable estimation deduced from experimental head injury using sub-human primates and human cadaver skulls’, in *24th Strapp Car Crash Conference*, Warrendale, PA, Oct. 1980, p. SAE 801303.

[69] T. Nishimoto and S. Murakami, ‘Relation Between Diffuse Axonal Injury and Internal Head Structures on Blunt Impact’, *J. Biomech. Eng.*, vol. 120, no. 1, pp. 140–147, Feb. 1998, doi: 10.1115/1.2834294.

[70] R. W. G. Anderson, C. J. Brown, P. C. Blumbergs, A. J. McLean, and N. R. Jones, ‘Impact Mechanics and Axonal Injury in a Sheep Model’, *J. Neurotrauma*, vol. 20, no. 10, pp. 961–974, Oct. 2003, doi: 10.1089/089771503770195812.

[71] E. S. Gurdjian, H. R. Lissner, F. G. Evans, L. M. Patrick, and W. G. Hardy, ‘Intracranial pressure and acceleration accompanying head impacts in human cadavers’, *Surg. Gynecol. Obstet.*, vol. 113, pp. 185–190, Aug. 1961.

[72] E. S. Gurdjian and H. R. Lissner, ‘Photoelastic Confirmation of the Presence of Shear Strains at the Craniospinal Junction in Closed Head Injury’, *Collections*, vol. 116, no. 6, pp. 58–60, May 2009, doi: 10.3171/jns.1961.18.1.0058@col.2012.116.issue-6.

[73] A. I. King, ‘Basics of the Biomechanics of Brain Injury’, in *The Biomechanics of Impact Injury: Biomechanical Response, Mechanisms of Injury, Human Tolerance and Simulation*, A. I. King, Ed., Cham: Springer International Publishing, 2018, pp. 35–76. doi: 10.1007/978-3-319-49792-1_2.

[74] E. S. Gurdjian, H. R. Lissner, J. E. Webster, F. R. Latimer, and B. F. Haddad, ‘Studies on experimental concussion: relation of physiologic effect to time duration of intracranial pressure increase at impact’, *Neurology*, vol. 4, no. 9, pp. 674–674, 1954.

[75] P. G. Young and C. l. Morfey, ‘Intracranial pressure transients caused by head impacts’, *Proc. Int. Res. Counc. Biomech. Inj. Conf.*, vol. 26, pp. 391–403, 1998, Accessed: Jul. 31, 2019. [Online]. Available:

https://www.safetylit.org/citations/index.php?fuseaction=citations.viewdetails&citationIds[]=citjournalarticle_247637_38

[76] E. S. Gurdjian, V. L. Roberts, and L. M. Thomas, 'Tolerance curves of acceleration and intracranial pressure and protective index in experimental head injury', *J. Trauma Acute Care Surg.*, vol. 6, no. 5, p. 600, Sep. 1966, [Online]. Available: https://journals.lww.com/jtrauma/Citation/1966/09000/Tolerance_Curves_of_Acceleration_and_Intracranial.5.aspx

[77] C. W. Gadd, 'Use of a Weighted-Impulse Criterion for Estimating Injury Hazard', SAE International, Warrendale, PA, SAE Technical Paper 660793, Feb. 1966. doi: 10.4271/660793.

[78] M. Kleinberger, E. Sun, R. Eppinger, S. Kuppa, and R. Saul, 'Development of improved injury criteria for the assessment of advanced automotive restraint systems', *Natl. Highw. Traffic Saf. Adm.*, vol. 4405, no. 9, pp. 12–17, Sep. 1998.

[79] H. Kimpara and M. Iwamoto, 'Mild Traumatic Brain Injury Predictors Based on Angular Accelerations During Impacts', *Ann. Biomed. Eng.*, vol. 40, no. 1, pp. 114–126, Jan. 2012, doi: 10.1007/s10439-011-0414-2.

[80] E. G. Takhounts, M. J. Craig, K. Moorhouse, J. McFadden, and V. Hasija, 'Development of Brain Injury Criteria (BrIC)', *Stapp Car Crash J.*, vol. 57, pp. 243–266, 2013.

[81] E. G. Takhounts, V. Hasija, S. A. Ridella, S. Rowson, and S. M. Duma, 'Kinematic Rotational Brain Injury Criterion (BRIC)', in *Proceedings of the 22nd International Technical Conference on the Enhanced Safety of Vehicles (ESV)*, Washington, DC, Jun. 2011, pp. 11–0263.

[82] J. A. Newman, 'A Generalized Model for Brain Injury Threshold (GAMBIT)', in *IRCOBI Conference Proceedings*, Zurich, Switzerland, Sep. 1986.

[83] J. A. Newman, N. Shewchenko, and E. Welbourne, 'A proposed New Biomechanical head injury assessment function - the maximum power index', *Stapp Car Crash J.*, vol. 44, pp. 215–47, 2000.

[84] S. Rowson and S. M. Duma, 'Brain Injury Prediction: Assessing the Combined Probability of Concussion Using Linear and Rotational Head Acceleration', *Ann. Biomed. Eng.*, vol. 41, no. 5, pp. 873–882, May 2013, doi: 10.1007/s10439-012-0731-0.

[85] S. Haddadin, A. Albu-Schaffer, and G. Hirzinger, 'The role of the robot mass and velocity in physical human-robot interaction - Part I: Non-constrained blunt impacts', in *2008 IEEE International Conference on Robotics and Automation*, May 2008, pp. 1331–1338. doi: 10.1109/ROBOT.2008.4543388.

[86] S. Haddadin, A. Albu-Schaffer, M. Frommberger, and G. Hirzinger, 'The role of the robot mass and velocity in physical human-robot interaction - Part II: Constrained blunt impacts', in *2008 IEEE International Conference on Robotics and Automation*, Pasadena, CA, USA, May 2008, p. 10014732. doi: 10.1109/ROBOT.2008.4543389.

[87] J. Newman, *Criteria for head injury and helmet standards*. 2005.

[88] L. Zhang, K. H. Yang, and A. I. King, 'A Proposed Injury Threshold for Mild Traumatic Brain Injury', *J. Biomech. Eng.*, vol. 126, no. 2, p. 226, 2004, doi: 10.1115/1.1691446.

[89] A. I. King, K. H. Yang, L. Zhang, W. Hardy, and D. C. Viano, 'Is Head Injury Caused by Linear or Angular Acceleration?', p. 12, 2003.

[90] C. Ward, M. Chan, and A. Nahum, 'Intracranial Pressure — A Brain Injury Criterion', *SAE Trans.*, vol. 89, pp. 3867–3880, 1980, Accessed: Apr. 21, 2019. [Online]. Available: https://www.jstor.org/stable/44632636

[91] S. Kleiven, 'Evaluation of head injury criteria using a finite element model validated against experiments on localized brain motion, intracerebral acceleration, and intracranial pressure', *Int. J. Crashworthiness*, vol. 11, no. 1, pp. 65–79, Jan. 2006, doi: 10.1533/ijcr.2005.0384.

[92] S. Kleiven, 'Predictors for Traumatic Brain Injuries Evaluated through Accident Reconstructions', SAE International, Warrendale, PA, SAE Technical Paper 2007-22–0003, Oct. 2007. doi: 10.4271/2007-22-0003.

[93] D. I. Shreiber, A. C. Bain, and D. F. Meaney, 'In vivo thresholds for mechanical injury to the blood-brain barrier', *SAE Trans.*, pp. 3792–3806, 1997.

[94] D. Marjoux, D. Baumgartner, C. Deck, and R. Willinger, 'Head injury prediction capability of the HIC, HIP, SIMon and ULP criteria', *Accid. Anal. Prev.*, vol. 40, no. 3, pp. 1135–1148, May 2008, doi: 10.1016/j.aap.2007.12.006.

[95] T. Whyte *et al.*, 'A Review of Impact Testing Methods for Headgear in Sports: Considerations for Improved Prevention of Head Injury Through Research and Standards', *J. Biomech. Eng.*, vol. 141, no. 7, May 2019, doi: 10.1115/1.4043140.

[96] International Organization for Standardization, 'ISO/TR 9790:1999(en), Road vehicles — Anthropomorphic side impact dummy — Lateral impact response requirements to assess the biofidelity of the dummy'. https://www.iso.org/obp/ui/#iso:std:iso:tr:9790:ed-1:v1:en

[97] International Organization for Standardization, 'ISO 15830-1:2013, Road vehicles — Design and performance specifications for the WorldSID 50th percentile male side-impact dummy-Part 1: Terminology and rationale', ISO Standard 2, 2013.

[98] H. H. Rhule, M. R. Maltese, B. R. Donnelly, R. H. Eppinger, J. K. Brunner, and J. H. Bolte, 'Development of a New Biofidelity Ranking System for Anthropomorphic Test Devices', in *46th Stapp Car Crash Conference (2002)*, Florida, United States, Nov. 2002, pp. 2002-22–0024. doi: 10.4271/2002-22-0024.

[99] D. Parent, M. Craig, and K. Moorhouse, 'Biofidelity Evaluation of the THOR and Hybrid III 50th Percentile Male Frontal Impact Anthropomorphic Test Devices', *Stapp Car Crash J.*, vol. 61, pp. 227–276, Nov. 2017, Accessed: Aug. 21, 2022. [Online]. Available: https://www.proquest.com/docview/1994594786/abstract/65C7FAA746624EADPQ/1

[100] C. Thunert, 'CORA Release 3.6 User's Manual'. GNS mbH, 2012.

[101] C. Gehre and S. Stahlschmidt, 'Assessment of dummy models by using objective rating methods', in *22nd International Technical Conference on the Enhanced Safety of Vehicles Conference (ESV)*, Washington, D.C., United States, Jun. 2011.

[102] H. J. Mertz, 'Biofidelity of the Hybrid III Head', *SAE Trans.*, vol. 94, pp. 97–105, 1985, Accessed: Apr. 19, 2020. [Online]. Available: https://www.jstor.org/stable/44724008

[103] A. MacAlister, 'Surrogate Head Forms for the Evaluation of Head Injury Risk', in *Brain Injuries and Biomechanics Symposium*, Washington DC, United States, Apr. 2013. Accessed: May 30, 2019. [Online]. Available: https://vtechworks.lib.vt.edu/handle/10919/23818

[104] CADEX Inc., 'Headforms: EN960 Half Headform Magnesium K1A'. http://www.cadexinc.com/en960_half_magnesium_k1a_headform.php (accessed Nov. 12, 2021).

[105] V. R. Hodgson, 'Head Model for Impact Tolerance', in *Human Impact Response: Measurement and Simulation*, W. F. King and H. J. Mertz, Eds., Boston, MA: Springer US, 1973, pp. 113–128. doi: 10.1007/978-1-4757-1502-6_6.

[106] NOCSAE, 'Standard performance specification for newly manufactured football helmets', *National Operating Committee on Standards for Athletic Equipment*. Nov. 01, 2018.

[107] A. C. Merkle, I. D. Wing, R. A. Armiger, B. G. Carkhuff, and J. C. Roberts, 'Development of a Human Head Physical Surrogate Model for Investigating Blast Injury', in *ASME 2009 International Mechanical Engineering Congress and Exposition*, Lake Buena Vista, Florida, USA: American Society of Mechanical Engineers Digital Collection, Jul. 2010, pp. 91–93. doi: 10.1115/IMECE2009-11807.

[108] A. M. Nahum, R. Smith, and C. C. Ward, 'Intracranial Pressure Dynamics During Head Impact', in *21st Stapp Car Crash Conference*, Warrendale, PA, Feb. 1977, p. 770922. doi: 10.4271/770922.

[109] 21st Century Solutions Ltd, 'Anatomium: Digital Human 3D Body Anatomy', 2002. https://www.anatomium.com/ (accessed Sep. 02, 2019).

[110] Standards Council of Canada, 'Specifications for Facially Featured Headforms CAN/CSA-Z262.6-02 (R2008)', 2002. https://www.scc.ca/en/standardsdb/standards/7663 (accessed Mar. 20, 2020).

[111] A. D. Azar, K. B. Bhagavathula, J. Hogan, S. Ouellet, S. Satapathy, and C. R. Dennison, 'Protective Headgear Attenuates Forces on the Inner Table and Pressure in the Brain Parenchyma During Blast and Impact: An Experimental Study Using a Simulant-Based Surrogate Model of the Human Head', *J. Biomech. Eng.*, vol. 142, no. 4, Apr. 2020, doi: 10.1115/1.4044926.

[112] A. Auperrin, R. Delille, D. Lesueur, K. Bruyère, C. Masson, and P. Drazétic, 'Geometrical and material parameters to assess the macroscopic mechanical behaviour of fresh cranial bone samples', *J. Biomech.*, vol. 47, no. 5, pp. 1180–1185, Mar. 2014, doi: 10.1016/j.jbiomech.2013.10.060.

[113] J. H. McElhaney, J. W. Melvin, V. L. Roberts, and H. D. Portnoy, 'Dynamic Characteristics of the Tissues of the Head', in *Perspectives in Biomedical Engineering: Proceedings of a Symposium organised in association with the Biological Engineering Society and held in the University of Strathclyde, Glasgow, June 1972*, R. M. Kenedi, Ed., London: Palgrave Macmillan UK, 1973, pp. 215–222. doi: 10.1007/978-1-349-01604-4_34.

[114] S. Ganpule, N. P. Daphalapurkar, M. P. Cetingul, and K. T. Ramesh, 'Effect of bulk modulus on deformation of the brain under rotational accelerations', *Shock Waves*, vol. 28, no. 1, pp. 127–139, Jan. 2018, Accessed: Sep. 19, 2020. [Online]. Available: https://www.ncbi.nlm.nih.gov/pmc/articles/PMC5898454/

[115] H. van Hoorn, N. A. Kurniawan, G. H. Koenderink, and D. Iannuzzi, 'Local dynamic mechanical analysis for heterogeneous soft matter using ferrule-top indentation', *Soft Matter*, vol. 12, no. 12, pp. 3066–3073, 2016.

[116] D. W. A. Brands, 'The Large Shear Strain Dynamic Behavior of In-Vitro Porcine Brain Tissue and a Silicone Gel Model Material', SAE International, Warrendale, PA, SAE Technical Paper 2000-01-SC17, Nov. 2000. doi: 10.4271/2000-01-SC17.

[117] D. W. A. Brands, P. H. M. Bovendeerd, and J. S. H. M. Wismans, 'On the Potential Importance of Non-Linear Viscoelastic Material Modelling for Numerical Prediction of Brain Tissue Response: Test and Application', presented at the 46th Stapp Car Crash Conference (2002), Nov. 2002, pp. 2002-22–0006. doi: 10.4271/2002-22-0006.

[118] A. Wittek *et al.*, 'Meshless Method for Simulation of Needle Insertion into Soft Tissues: Preliminary Results', in *Computational Biomechanics for Medicine*, M. P. Nash, P. M. F. Nielsen, A. Wittek, K. Miller, and G. R. Joldes, Eds., Cham: Springer International Publishing, 2020, pp. 73–86. doi: 10.1007/978-3-030-15923-8_6.

[119] A. M. Loyd *et al.*, 'The response of the adult and ATD heads to impacts onto a rigid surface', *Accid. Anal. Prev.*, vol. 72, pp. 219–229, Nov. 2014, doi: 10.1016/j.aap.2014.06.022.

[120] Y. Li, S. Ouellet, A. Vette, D. W. Raboud, A. Martin, and C. Dennison, 'Evaluation of the Kinematic Biofidelity and Inter-Test Repeatability of Global Accelerations and Brain Parenchyma Pressure for a Head-Brain Physical Model', *J. Biomech. Eng.*, vol. 143, no. 9, p. 091006, Apr. 2021, doi: 10.1115/1.4050752.

[121] Northern Brain Injury Association, 'Brain Injury Statistics'. http://nbia.ca/brain-injury-statistics/

[122] W. N. Hardy, T. B. Khalil, and A. I. King, 'Literature review of head injury biomechanics', *Int. J. Impact Eng.*, vol. 15, no. 4, pp. 561–586, Aug. 1994, doi: 10.1016/0734-743X(94)80034-7.

[123] E. S. Gurdjian and J. E. Webster, 'Linear acceleration causing shear in the brain stem in trauma of the central nervous system', *Ment. Adv. Dis.*, vol. 24, p. 28, 1945.

[124] D. Marjoux, D. Baumgartner, C. Deck, and R. Willinger, 'Head injury prediction capability of the HIC, HIP, SIMon and ULP criteria', *Accid. Anal. Prev.*, vol. 40, no. 3, pp. 1135–1148, May 2008, doi: 10.1016/j.aap.2007.12.006.

[125] C. Ward, M. Chan, and A. Nahum, 'Intracranial Pressure — A Brain Injury Criterion', *SAE Trans.*, vol. 89, pp. 3867–3880, 1980, Accessed: Dec. 23, 2020. [Online]. Available: https://www.jstor.org/stable/44632636

[126] H. Rhule, K. Moorhouse, B. Donnelly, and J. Stricklin, 'Comparison of WorldSID and ES-2re Biofidelity Using an Updated Biofidelity Ranking System', *Proc. Int. Tech. Conf. Enhanc. Saf. Veh.*, vol. 2009, 2009, Accessed: Jun. 09, 2019. [Online]. Available:

https://www.safetylit.org/citations/index.php?fuseaction=citations.viewdetails&citationIds[]=citjournalarticle_244915_38

[127] N. Atsumi, Y. Nakahira, and M. Iwamoto, 'Development and validation of a head/brain FE model and investigation of influential factor on the brain response during head impact', *Int. J. Veh. Saf.*, vol. 9, no. 1, pp. 1–23, Jan. 2016, doi: 10.1504/IJVS.2016.077145.

[128] N. Atsumi, Y. Nakahira, E. Tanaka, and M. Iwamoto, 'Human Brain Modeling with Its Anatomical Structure and Realistic Material Properties for Brain Injury Prediction', *Ann. Biomed. Eng.*, vol. 46, no. 5, pp. 736–748, May 2018, doi: 10.1007/s10439-018-1988-8.

[129] G. P. Siegmund, K. M. Guskiewicz, S. W. Marshall, A. L. DeMarco, and S. J. Bonin, 'A Headform for Testing Helmet and Mouthguard Sensors that Measure Head Impact Severity in Football Players', *Ann. Biomed. Eng.*, vol. 42, no. 9, pp. 1834–1845, Sep. 2014, doi: 10.1007/s10439-014-1052-2.

[130] H. J. Mertz, 'Biofidelity of the Hybrid III Head', *SAE Trans.*, vol. 94, pp. 97–105, 1985, Accessed: Sep. 18, 2019. [Online]. Available: https://www.jstor.org/stable/44724008

[131] S. Ouellet, C. Bir, and A. Bouamoul, 'Direct Comparison of the Primary Blast Response of a Physical Head Model with Post-mortem Human Subjects', *Defence Research and Development Canada-Valcartier Research Center Quebec, QC Canada.*, p. 10, 2014.

[132] Society of Automotive Engineers, 'Instrumentation for Impact Test—Part 1—Electronic Instrumentation', *Tech. Rep. SAE J2111*, 2007.

[133] A. M. Loyd, 'Studies of the human head from neonate to adult: an inertial, geometrical and structural analysis with comparisons to the ATD head', Doctoral dissertation, Duke University, Durham, NC., 2011.

[134] W. N. Hardy *et al.*, 'A Study of the Response of the Human Cadaver Head to Impact', *Stapp Car Crash J.*, vol. 51, pp. 17–80, Oct. 2007, Accessed: Jun. 03, 2019. [Online]. Available: https://www.ncbi.nlm.nih.gov/pmc/articles/PMC2474809/

[135] R. Eppinger, S. Emily, K. Michael, S. Kuppa, and R. Saul, 'Development of improved injury criteria for the assessment of advanced automotive restraint systems', 1998. https://rosap.ntl.bts.gov/view/dot/14737

[136] M. B. Panzer, G. W. Wood, and C. R. Bass, 'Scaling in neurotrauma: How do we apply animal experiments to people?', *Exp. Neurol.*, vol. 261, pp. 120–126, Nov. 2014, doi: 10.1016/j.expneurol.2014.07.002.

[137] Laerd Statistics, 'Independent-samples t-test in Stata | Laerd Statistics Premium', 2016. https://statistics.laerd.com/ (accessed Apr. 19, 2020).

[138] Laerd Statistics, 'One-way ANCOVA in SPSS Statistics | Laerd Statistics Premium', 2017. https://statistics.laerd.com/premium/spss/a/one-way-ancova-in-spss-21.php

[139] E. J. Pellman, D. C. Viano, A. M. Tucker, I. R. Casson, and J. F. Waeckerle, 'Concussion in Professional Football: Reconstruction of Game Impacts and Injuries', *Neurosurgery*, vol. 53, no. 4, pp. 799–814, Sep. 2003, doi: 10.1093/neurosurgery/53.3.799.

[140] J. A. Motherway, P. Verschueren, G. Van der Perre, J. Vander Sloten, and M. D. Gilchrist, 'The mechanical properties of cranial bone: The effect of loading rate and cranial sampling position', *J. Biomech.*, vol. 42, no. 13, pp. 2129–2135, Sep. 2009, doi: 10.1016/j.jbiomech.2009.05.030.

[141] M. S. Jazi, A. Rezaei, G. Karami, F. Azarmi, and M. Ziejewski, 'A computational study of influence of helmet padding materials on the human brain under ballistic impacts', *Comput. Methods Biomech. Biomed. Engin.*, vol. 17, no. 12, pp. 1368–1382, Sep. 2014, doi: 10.1080/10255842.2012.748755.

[142] R. Delille, D. Lesueur, P. Potier, P. Drazetic, and E. Markiewicz, 'Experimental study of the bone behaviour of the human skull bone for the development of a physical head model', *Int. J. Crashworthiness*, vol. 12, no. 2, pp. 101–108, Aug. 2007, doi: 10.1080/13588260701433081.

[143] W. Zhao, S. Ruan, and S. Ji, 'Brain pressure responses in translational head impact: a dimensional analysis and a further computational study', *Biomech. Model. Mechanobiol.*, vol. 14, no. 4, pp. 753–766, Aug. 2015, doi: 10.1007/s10237-014-0634-0.

[144] C. W. Pearce and P. G. Young, 'On the Pressure Response in the Brain due to Short Duration Blunt Impacts', *PLOS ONE*, vol. 9, no. 12, p. e114292, Dec. 2014, doi: 10.1371/journal.pone.0114292.

[145] T. Payne, S. Mitchell, and R. Bibb, 'Design of Human Surrogates for the Study of Biomechanical Injury: A Review', *Crit. Rev. Biomed. Eng.*, vol. 41, no. 1, 2013, doi: 10.1615/CritRevBiomedEng.2013006847.

[146] R. P. Hubbard and D. G. McLeod, 'Definition and Development of A Crash Dummy Head', *SAE Trans.*, vol. 83, pp. 3836–3851, 1974, Accessed: Jan. 26, 2020. [Online]. Available: https://www.jstor.org/stable/44723992

[147] B. M. Knowles and C. R. Dennison, 'Predicting Cumulative and Maximum Brain Strain Measures From HybridIII Head Kinematics: A Combined Laboratory Study and Post-Hoc Regression Analysis', *Ann. Biomed. Eng.*, vol. 45, no. 9, pp. 2146–2158, Sep. 2017, doi: 10.1007/s10439-017-1848-y.

[148] C. Deck and R. Willinger, 'Improved head injury criteria based on head FE model', *Int. J. Crashworthiness*, vol. 13, no. 6, pp. 667–678, Dec. 2008, doi: 10.1080/13588260802411523.

[149] V. R. Hodgson, 'National Operating Committee on Standards for Athletic Equipment football helmet certification program', *Med. Sci. Sports*, vol. 7, no. 3, pp. 225–232, Jan. 1975.

[150] A. Boaks, D. Siwek, and F. Mortazavi, 'The temporal degradation of bone collagen: A histochemical approach', *Forensic Sci. Int.*, vol. 240, pp. 104–110, Jul. 2014, doi: 10.1016/j.forsciint.2014.04.008.

[151] L. Shi, Y. Han, H. Huang, J. Davidsson, and R. Thomson, 'Evaluation of injury thresholds for predicting severe head injuries in vulnerable road users resulting from ground impact via detailed accident reconstructions', *Biomech. Model. Mechanobiol.*, Mar. 2020, doi: 10.1007/s10237-020-01312-9.

[152] C. Karton, T. B. Hoshizaki, and M. D. Gilchrist, 'The Influence of Impact Angle on the Dynamic Response of a Hybrid III Headform and Brain Tissue Deformation', 2014. doi: 10.1520/STP155220120160.

[153] R. A. Oeur, M. D. Gilchrist, and T. B. Hoshizaki, 'Parametric study of impact parameters on peak head acceleration and strain for collision impacts in sport', *Int. J. Crashworthiness*, vol. 0, no. 0, pp. 1–10, Jun. 2019, doi: 10.1080/13588265.2019.1634336.

[154] S. SAE, *SAE J211-1 (1995): Instrumentation for Impact Test, Part 1, Electronic Instrumentation*. 2007. [Online]. Available: https://law.resource.org/pub/us/cfr/ibr/005/sae.j211-1.1995.pdf

[155] International Organization for Standardization, 'ISO 15830-1:2013(en), Road vehicles — Design and performance specifications for the WorldSID 50th percentile male side-impact dummy — Part 1: Terminology and rationale'. https://www.iso.org/obp/ui/#iso:std:iso:15830:-1:ed-2:v1:en (accessed Jan. 05, 2021).

[156] M. L. Davis, B. Koya, J. M. Schap, F.-C. Hsu, and F. S. Gayzik, 'Comparison of Objective Rating Techniques vs. Expert Opinion in the Validation of Human Body Surrogates', in *Proc. 25th International Technical Conference on the Enhanced Safety of Vehicles (ESV) National Highway Traffic Safety Administration*, Detroit, Michigan USA, 2017.

[157] C. Gehre, H. Gades, and P. Wernicke, 'Objective Rating of Signals Using Test and Simulation Responses', *Proc. Int. Tech. Conf. Enhanc. Saf. Veh.*, vol. 2009, 2009, Accessed: Sep. 24, 2019. [Online]. Available: https://www.safetylit.org/citations/index.php?fuseaction=citations.viewdetails&citationIds[]=citjournalarticle_245656_38

[158] A. Sances Jr, 'Dynamic comparison of the hybrid III and human neck', *Front. Head Neck Trauma Ed. N Yoganandan IOS Press*, pp. 147–150, 1998.

[159] P. Reilly and R. Bullock, *Head Injury 2Ed: Pathophysiology & Management*. CRC Press, 2005. doi: 10.1201/b13492.

[160] D. J. Thurman, C. Alverson, K. A. Dunn, J. Guerrero, and J. E. Sniezek, 'Traumatic Brain Injury in the United States: A Public Health Perspective', *J. Head Trauma Rehabil.*, vol. 14, no. 6, pp. 602–615, Dec. 1999.

[161] D. Kallieris, A. Rizzetti, and R. Mattern, 'The biofidelity of hybrid III dummies', presented at the International Research Council on Biomechanics of Injury (IRCOBI) Conference., Bruunen, Switzerland, Sep. 1995, pp. 135–154.

[162] J. Afshari, M. Haghpanahi, and R. Kalantarinejad, 'Developing new brain injury criteria for predicting the intracranial response by calculating von Mises stress, coup pressure and contrecoup pressure', *J. Braz. Soc. Mech. Sci. Eng.*, vol. 39, no. 10, pp. 3729–3741, Oct. 2017, doi: 10.1007/s40430-017-0830-9.

[163] E. J. Sanchez *et al.*, 'Evaluation of Head and Brain Injury Risk Functions Using Sub-Injurious Human Volunteer Data', *J. Neurotrauma*, vol. 34, no. 16, pp. 2410–2424, Aug. 2017, doi: 10.1089/neu.2016.4681.

[164] K.-U. Schmitt, P. F. Niederer, D. S. Cronin, B. Morrison III, M. H. Muser, and F. Walz, 'Head injuries', in *Trauma Biomechanics*, Springer, 2019, pp. 87–115.

[165] C. Giordano and S. Kleiven, 'Evaluation of Axonal Strain as a Predictor for Mild Traumatic Brain Injuries Using Finite Element Modeling', *Stapp Car Crash J.*, vol. 58, pp. 29–62, Nov. 2014.

[166] A. Singh, R. Rajan, and S. Ganpule, 'An experimental investigation of impact of pendulum with the surrogate head', *Int. J. Adv. Eng. Sci. Appl. Math.*, vol. 12, no. 3, pp. 94–100, Dec. 2020, doi: 10.1007/s12572-020-00273-7.

[167] A. Trotta, D. Zouzias, G. De Bruyne, and A. Ní Annaidh, 'The Importance of the Scalp in Head Impact Kinematics', *Ann. Biomed. Eng.*, vol. 46, no. 6, pp. 831–840, Jun. 2018, doi: 10.1007/s10439-018-2003-0.

[168] V. D. H. L.A. Bosch, M. W. B. M. Leensen, N. H. M. Klomp, A. a. H. J. Sauren, and J. S. H. M. Wismans, 'Development of an improved dummy head for use in helmet certification tests', *Proc. WAM2000 ASME Symp. Crashworthiness Occupant Prot. Biomech. Transp. Syst.*, pp. 189–205, 2000, Accessed: Jul. 21, 2020. [Online]. Available: https://research.tue.nl/en/publications/development-of-an-improved-dummy-head-for-use-in-helmet-certifica

[169] K. Adanty *et al.*, 'Cortical and trabecular morphometric properties of the human calvarium', *Bone*, vol. 148, p. 115931, Jul. 2021, doi: 10.1016/j.bone.2021.115931.

[170] T. W. Barber, J. A. Brockway, and L. S. Higgins, 'The density of tissues in and about the head', *Acta Neurol. Scand.*, vol. 46, no. 1, pp. 85–92, 1970.

[171] S. A. Lippert, E. M. Rang, and M. J. Grimm, 'The high frequency properties of brain tissue', *Biorheology*, vol. 41, no. 6, pp. 681–691, Jan. 2004, Accessed: Feb. 12, 2023. [Online]. Available: https://content.iospress.com/articles/biorheology/bir345

[172] E. L. Madsen *et al.*, 'Instrument for determining the complex shear modulus of soft-tissue-like materials from 10 to 300 Hz', *Phys. Med. Biol.*, vol. 53, no. 19, p. 5313, 2008.

[173] D. Singh, S. Boakye-Yiadom, and D. S. Cronin, 'Comparison of porcine brain mechanical properties to potential tissue simulant materials in quasi-static and sinusoidal compression', *J. Biomech.*, vol. 92, pp. 84–91, Jul. 2019, doi: 10.1016/j.jbiomech.2019.05.033.

[174] Y. Jammes, M. Viala, W. Dutto, J. P. Weber, and R. Guieu, 'Skin hardness and epidermal thickness affect the vibration sensitivity of the foot sole', *Clin Res Foot Ankle*, vol. 5, no. 3, pp. 1–5, 2017.

[175] R. Periyasamy, S. Anand, and A. C. Ammini, 'The effect of aging on the hardness of foot sole skin: A preliminary study', *The Foot*, vol. 22, no. 2, pp. 95–99, Jun. 2012, doi: 10.1016/j.foot.2012.01.003.

[176] P. B. Lindley, 'Load-compression relationships of rubber units', *J. Strain Anal.*, vol. 1, no. 3, pp. 190–195, Apr. 1966, doi: 10.1243/03093247V013190.

[177] A. K. Ommaya, P. Yarnell, A. E. Hirsch, and E. H. Harris, 'Scaling of Experimental Data on Cerebral Concussion in Sub-Human Primates to Concussion Threshold for Man',

presented at the 11th Stapp Car Crash Conference (1967), Feb. 1967, p. 670906. doi: 10.4271/670906.

[178] J. Cohen, *Statistical power analysis for the behavioral sciences*. Academic press, 2013.

[179] J. P. A. Ioannidis, 'What Have We (Not) Learnt from Millions of Scientific Papers with P Values?', *Am. Stat.*, Mar. 2019, Accessed: Jan. 07, 2023. [Online]. Available: https://www.tandfonline.com/doi/abs/10.1080/00031305.2018.1447512

[180] Z. Zhou, X. Li, S. Kleiven, C. S. Shah, and W. N. Hardy, 'A Reanalysis of Experimental Brain Strain Data: Implication for Finite Element Head Model Validation', presented at the 62nd Stapp Car Crash Conference, Nov. 2018. doi: 10.4271/2018-22-0007.

[181] S. Abrate, *Impact Engineering of Composite Structures*. Springer Science & Business Media, 2011.

[182] E. A. Bakirzis, 'Stiffness characteristics of rubber impact absorbers', *J. Strain Anal.*, vol. 7, no. 1, pp. 33–40, 1972.

[183] J. D. Ferry, *Viscoelastic Properties of Polymers*. John Wiley & Sons, 1980.

[184] V. R. Hodgson and L. M. Thomas, 'Comparison of head acceleration injury indices in cadaver skull fracture', *SAE Trans.*, pp. 2894–2902, 1971.

Appendix

Table A 1 Average (Ave.), standard deviation (Std.), and COV of the measurement peaks including the linear accelerations and angular rates in XYZ directions, and CSFP and IPP at the front, side, and back of the head. F., S., and B. represent ICP measured at the front, right side, and back. X Acc. and X AnR. means the linear acceleration and angular rate on X-axis. Tabulated were measurements from the impactor surface of VN600 for each impact velocity V.

V Ave. (Std.) (m/s)		X Acc. (g)	Y Acc. (g)	Z Acc. (g)	X AnR. (rad/s)	Y AnR. (rad/s)	Z AnR. (rad/s)	F. CSFP (kPa)	S. CSFP (kPa)	B. CSFP Max (kPa)	B. CSFP Min (kPa)	F. IPP (kPa)	S. IPP (kPa)	B. IPP Max (kPa)	B. IPP Min (kPa)
0.52 (0.01)	Ave.	-1.8	-0.1	0.7	0.0	1.0	0.0	4.8	3.0	1.6	-0.1	3.9	3.0	2.5	-0.2
	Std.	0.1	0.3	0.1	0.4	0.0	0.3	0.3	0.2	0.1	0.0	0.3	0.2	0.1	0.0
	COV	6.9%	217.2%	10.3%	9657.5%	4.1%	4119.5%	7.2%	5.7%	9.1%	60.3%	8.2%	5.9%	2.8%	16.2%
0.99 (0.03)	Ave.	-4.0	-0.4	0.6	-0.2	1.4	0.2	9.7	6.0	2.9	-0.3	7.8	6.0	4.5	-0.1
	Std.	0.1	0.1	1.2	0.3	0.1	0.4	0.2	0.1	0.1	0.0	0.2	0.1	0.1	0.0
	COV	1.3%	14.8%	208.7%	181.3%	6.8%	189.2%	1.8%	2.0%	4.5%	11.1%	2.2%	1.6%	1.8%	13.5%
2.04 (0.04)	Ave.	-22.3	-3.2	-10.3	0.9	2.7	1.2	38.2	25.6	8.7	-2.4	28.5	22.4	14.0	-0.4
	Std.	0.3	0.2	0.2	0.1	0.1	0.1	0.3	0.2	0.5	0.5	0.3	0.2	0.1	0.1
	COV	1.5%	4.9%	2.1%	9.4%	5.3%	4.6%	0.9%	0.7%	5.6%	20.1%	1.0%	0.7%	0.7%	18.6%
3.09 (0.10)	Ave.	-36.4	10.3	17.7	1.3	4.5	1.7	58.6	41.1	17.6	-4.6	43.5	34.1	21.5	-0.9
	Std.	0.5	0.6	0.2	0.2	0.1	0.2	0.5	0.7	1.3	0.6	0.4	0.6	0.6	0.0
	COV	1.3%	5.6%	1.4%	14.4%	2.1%	11.6%	0.8%	1.8%	7.2%	12.2%	0.9%	1.7%	3.0%	5.1%
4.05 (0.11)	Ave.	-49.2	13.3	26.1	1.4	6.7	1.7	78.0	54.6	23.2	-8.2	58.0	44.4	28.3	-1.5
	Std.	0.7	1.3	0.9	0.0	0.1	0.1	0.3	0.5	1.6	1.3	0.1	0.4	0.7	0.0
	COV	1.5%	9.8%	3.3%	3.4%	1.4%	6.6%	0.4%	0.9%	6.9%	15.6%	0.1%	1.0%	2.5%	2.9%
4.98 (0.07)	Ave.	-57.6	19.2	33.4	1.5	7.2	2.0	97.8	65.9	27.2	-11.9	71.6	53.1	36.6	-2.3
	Std.	0.6	1.4	0.7	0.1	0.0	0.0	0.5	0.6	0.3	1.0	0.4	0.4	0.3	0.1
	COV	1.1%	7.4%	2.1%	8.2%	0.1%	1.1%	0.5%	0.9%	1.1%	8.6%	0.6%	0.8%	0.7%	5.8%

Table A 2 Average (Ave.), standard deviation (Std.), and COV of the measurement peaks including the linear accelerations and angular rates in XYZ directions, and CSFP and IPP at the front, side, and back of the head. F., S., and B. represent ICP measured at the front, right side, and back. X Acc. and X AnR. means the linear acceleration and angular rate on X axis. Tabulated were measurements from the impactor surface of steel for each impact velocity V.

V Ave. (Std.) (m/s)		X Acc. (g)	Y Acc. (g)	Z Acc. (g)	X AnR. (rad/s)	Y AnR. (rad/s)	Z AnR. (rad/s)	F. CSFP (kPa)	S. CSFP (kPa)	B. CSFP Max (kPa)	B. CSFP Min (kPa)	F. IPP (kPa)	S. IPP (kPa)	B. IPP Max (kPa)	B. IPP Min (kPa)
0.52 (0.02)	Ave.	-5.3	-1.2	-6.1	0.2	1.5	0.0	10.5	6.1	1.6	-0.8	7.6	5.6	3.2	-0.2
	Std.	0.3	0.2	0.5	0.3	0.1	0.4	0.7	0.4	0.2	0.1	0.4	0.3	0.2	0.0
	COV	6.2%	14.6%	8.1%	183.7%	7.5%	11896.3%	6.2%	5.8%	10.5%	15.7%	5.2%	5.7%	7.2%	11.7%
0.98 (0.04)	Ave.	-15.0	8.9	-16.2	0.6	2.7	0.0	25.4	16.0	6.2	-1.6	16.8	13.6	9.3	-0.6
	Std.	0.2	14.4	0.2	0.1	0.1	0.5	0.3	0.3	0.4	0.1	0.2	0.2	0.2	0.0
	COV	1.2%	162.1%	1.2%	12.3%	4.5%	1231.6%	1.2%	1.7%	6.6%	8.0%	1.0%	1.4%	1.8%	8.0%
1.55 (0.05)	Ave.	-57.1	-14.5	50.0	0.9	5.8	0.1	78.8	74.9	22.2	-9.7	47.0	54.6	27.4	-2.6
	Std.	0.3	0.7	0.3	0.0	0.2	1.6	0.3	0.4	0.7	0.5	0.2	0.3	0.2	0.1
	COV	0.6%	4.6%	0.7%	4.5%	3.0%	2817.9%	0.3%	0.5%	3.1%	5.3%	0.4%	0.6%	0.7%	2.0%
2.03 (0.09)	Ave.	-75.9	-8.0	84.6	1.3	7.3	-1.0	119.4	105.0	31.0	-16.9	68.0	77.7	38.9	-4.5
	Std.	1.2	22.9	0.7	0.1	0.0	1.7	0.9	1.1	3.2	1.9	0.4	0.9	0.3	0.1
	COV	1.6%	284.5%	0.9%	8.4%	0.3%	173.1%	0.8%	1.1%	10.4%	11.4%	0.6%	1.2%	0.7%	1.6%
2.51 (0.04)	Ave.	-111.7	31.0	128.6	1.8	7.4	3.7	174.2	146.5	34.7	-22.6	95.8	107.4	45.6	-6.3
	Std.	0.74	11.3	0.3	0.2	0.0	0.1	0.4	1.0	3.0	2.2	0.3	0.5	0.3	0.0
	COV	0.7%	36.4%	0.2%	8.8%	0.2%	1.9%	0.2%	0.7%	8.6%	9.9%	0.3%	0.5%	0.6%	0.4%
3.10 (0.07)	Ave.	-146.7	-36.9	173.0	2.0	7.5	4.3	221.0	182.2	38.0	-29.5	119.4	132.9	54.1	-7.9
	Std.	1.0	1.1	0.7	0.1	0.0	0.1	1.2	1.6	2.5	1.9	0.6	0.6	0.3	0.2
	COV	0.7%	3.0%	0.4%	4.1%	0.5%	2.3%	0.6%	0.9%	6.6%	6.4%	0.5%	0.5%	0.5%	2.2%

Table A 3 Average peaks and durations with standard deviations for the acceleration (i.e., Acc. & Acc. d) and coup pressure (i.e., CP & CP d) measurements for impacts at the front, right side, and back with each scalp pad.

Pad Material	Impact Location	Thickness (mm)	5cm impact				19.5 cm impact			
			Acc. (g)	Acc. d (ms)	CP (kPa)	CP d (ms)	Acc. (g)	Acc. d (ms)	CP (kPa)	CP d (ms)
Vytaflex20	Front	2	51.3 (0.0)	6.0 (0.1)	53.3 (0.6)	4.2 (0.1)	104.0 (4.3)	4.9 (0.1)	118.4 (4.0)	3.7 (0.0)
		4	47.2 (1.7)	7.5 (0.2)	52.5 (2.0)	4.7 (0.1)	97.5 (4.4)	5.8 (0.1)	102.0 (2.7)	4.2 (0.1)
		6	41.3 (0.2)	9.1 (0.4)	44.9 (1.6)	5.7 (0.1)	97.2 (3.2)	6.6 (0.3)	101.7 (5.7)	4.5 (0.1)
		8	39.4 (1.2)	11.1 (0.3)	41.1 (0.9)	6.2 (0.1)	88.5 (0.3)	8.4 (0.0)	93.9 (1.6)	4.9 (0.0)
	Right Side	2	38.4 (0.9)	5.5 (0.7)	43.1 (1.5)	3.9 (0.0)	76.6 (6.4)	5.5 (0.1)	85.0 (8.8)	3.4 (0.1)
		4	34.0 (1.7)	7.7 (0.6)	35.5 (2.1)	4.8 (0.0)	82.5 (4.9)	6.0 (0.5)	86.5 (1.0)	3.6 (0.0)
		6	29.9 (1.1)	10.7 (0.3)	33.8 (2.0)	5.5 (0.1)	78.5 (5.3)	6.5 (0.1)	88.8 (4.5)	3.9 (0.0)
		8	26.9 (0.8)	10.8 (1.0)	33.7 (1.6)	6.0 (0.1)	59.3 (1.2)	8.8 (0.3)	72.4 (3.4)	4.9 (0.0)
	Back	2	36.3 (1.6)	5.9 (0.0)	42.2 (1.5)	4.2 (0.2)	76.7 (5.1)	5.8 (0.0)	86.8 (11.0)	4.2 (0.3)
		4	32.5 (0.7)	7.8 (0.4)	35.4 (1.6)	5.1 (0.0)	79.6 (0.1)	6.1 (0.2)	92.0 (1.2)	4.1 (0.1)
		6	30.6 (0.7)	9.0 (0.2)	32.9 (0.7)	5.7 (0.1)	77.0 (3.5)	7.0 (0.3)	85.1 (3.5)	4.4 (0.1)
		8	28.6 (1.2)	11.5 (0.9)	30.8 (1.9)	6.5 (0.2)	75.6 (2.0)	8.0 (0.2)	81.6 (1.1)	4.9 (0.1)
Vytaflex40	Front	2	51.2 (0.7)	5.7 (0.3)	53.6 (1.6)	4.2 (0.1)	104.6 (6.9)	5.1 (0.1)	110.3 (8.8)	3.9 (0.1)
		4	47.8 (1.0)	6.3 (0.0)	51.7 (2.3)	4.6 (0.1)	104.0 (2.5)	5.3 (0.1)	108.1 (2.1)	4.0 (0.0)
		6	45.8 (0.8)	8.8 (1.0)	48.0 (2.2)	5.2 (0.0)	100.5 (1.3)	5.7 (0.0)	102.5 (4.2)	4.3 (0.1)
		8	42.0 (1.7)	8.9 (0.4)	43.0 (2.5)	5.8 (0.2)	94.7 (2.5)	7.7 (0.4)	101.5 (3.6)	4.6 (0.1)
	Right Side	2	39.5 (1.7)	5.3 (0.4)	44.7 (1.2)	3.9 (0.0)	82.3 (3.4)	5.4 (0.3)	97.2 (3.6)	3.4 (0.0)
		4	34.6 (2.8)	5.8 (0.3)	34.9 (4.0)	4.3 (0.0)	89.2 (3.7)	5.4 (0.7)	95.5 (4.0)	3.4 (0.0)
		6	33.4 (0.6)	8.2 (0.7)	35.1 (1.0)	4.9 (0.1)	82.0 (1.6)	6.0 (0.2)	93.1 (2.4)	3.7 (0.1)

		8	30.7 (0.9)	9.9 (0.6)	33.6 (0.3)	5.6 (0.0)	72.2 (6.3)	7.5 (0.5)	89.2 (8.5)	4.2 (0.1)
	Back	2	37.5 (1.1)	5.9 (0.3)	45.1 (0.6)	4.2 (0.1)	75.3 (4.2)	6.0 (0.1)	94.0 (4.1)	4.0 (0.1)
		4	36.7 (1.6)	6.0 (0.1)	41.7 (0.8)	4.4 (0.2)	73.3 (3.5)	6.2 (0.5)	98.4 (3.9)	4.2 (0.1)
		6	33.2 (1.4)	8.8 (0.2)	35.3 (1.8)	5.1 (0.2)	67.1 (4.1)	7.2 (0.4)	83.3 (5.8)	4.5 (0.2)
		8	31.1 (0.5)	9.3 (0.5)	32.6 (0.4)	5.8 (0.1)	72.4 (2.0)	7.7 (0.6)	85.4 (4.0)	4.8 (0.2)
Vytaflex50	Front	2	50.5 (4.4)	5.7 (0.5)	52.1 (5.8)	4.2 (0.2)	101.6 (5.5)	5.1 (0.2)	106.2 (2.9)	3.9 (0.2)
		4	49.5 (0.8)	6.5 (0.3)	51.6 (0.6)	4.5 (0.1)	100.4 (2.0)	5.2 (0.1)	108.0 (5.3)	4.0 (0.0)
		6	47.2 (2.1)	7.4 (0.3)	51.0 (3.3)	4.9 (0.1)	97.3 (5.2)	5.9 (0.5)	102.8 (2.4)	4.3 (0.2)
		8	43.9 (0.8)	8.8 (0.3)	45.8 (1.5)	5.3 (0.2)	93.0 (0.8)	6.5 (0.2)	96.3 (0.4)	4.6 (0.1)
	Right Side	2	38.9 (0.8)	5.2 (0.4)	45.1 (1.6)	3.9 (0.1)	80.3 (6.6)	5.1 (0.8)	95.8 (7.2)	3.4 (0.1)
		4	35.7 (1.6)	6.3 (1.2)	36.8 (3.2)	4.2 (0.1)	84.9 (7.7)	5.6 (0.5)	92.1 (9.1)	3.4 (0.1)
		6	35.2 (2.3)	6.5 (0.2)	33.9 (2.2)	4.7 (0.1)	77.5 (0.6)	6.1 (0.2)	88.9 (0.7)	3.6 (0.0)
		8	30.1 (0.5)	9.4 (0.2)	31.4 (1.7)	5.5 (0.0)	72.4 (5.9)	7.1 (0.3)	86.4 (6.8)	4.0 (0.2)
	Back	2	36.5 (1.2)	5.7 (0.1)	44.0 (2.0)	4.2 (0.1)	81.8 (2.2)	5.7 (0.1)	95.9 (1.5)	3.9 (0.0)
		4	34.8 (0.4)	6.6 (0.1)	39.8 (1.2)	4.4 (0.1)	77.3 (1.1)	5.7 (0.2)	96.3 (3.2)	4.0 (0.0)
		6	34.0 (0.4)	7.8 (0.2)	37.4 (0.5)	4.9 (0.0)	76.0 (1.3)	6.5 (0.3)	90.7 (0.7)	4.3 (0.0)
		8	32.8 (0.4)	9.1 (0.0)	35.2 (0.9)	5.5 (0.1)	74.6 (3.7)	7.3 (0.1)	83.7 (3.7)	4.6 (0.1)
PMC746	Front	2	49.7 (1.5)	6.4 (0.4)	52.0 (3.3)	4.2 (0.2)	101.6 (1.8)	5.1 (0.1)	105.1 (0.9)	3.9 (0.1)
		4	49.1 (1.1)	6.9 (0.6)	49.5 (1.1)	4.7 (0.1)	98.5 (2.3)	6.6 (0.2)	107.2 (2.5)	4.0 (0.1)
		6	45.4 (1.5)	8.4 (0.5)	47.6 (1.3)	5.2 (0.2)	94.5 (3.7)	7.1 (0.5)	101.7 (5.7)	4.4 (0.1)
		8	42.1 (1.1)	9.4 (0.6)	43.5 (1.8)	5.8 (0.1)	88.1 (2.3)	7.5 (0.2)	95.2 (3.3)	4.8 (0.2)
	Right Side	2	38.1 (0.7)	5.4 (0.2)	44.2 (1.4)	3.9 (0.1)	72.1 (5.2)	5.8 (0.5)	83.8 (6.2)	3.4 (0.0)
		4	34.8 (2.3)	5.8 (0.3)	36.5 (3.3)	4.5 (0.2)	68.2 (0.3)	6.6 (0.1)	71.6 (1.4)	3.6 (0.0)
		6	34.6 (4.4)	7.2 (0.2)	35.7 (2.6)	4.9 (0.1)	70.6 (5.0)	6.7 (0.2)	79.7 (7.7)	3.9 (0.2)

		8	29.5 (3.9)	8.5 (1.1)	30.5 (4.9)	5.6 (0.2)	62.4 (4.0)	8.8 (0.4)	73.0 (7.5)	4.4 (0.1)
	Back	2	37.1 (1.3)	5.7 (0.1)	43.8 (2.3)	4.2 (0.0)	79.0 (4.5)	6.0 (0.2)	93.3 (6.6)	3.9 (0.1)
		4	35.1 (0.6)	7.0 (0.4)	41.1 (0.6)	4.5 (0.2)	79.0 (0.6)	5.8 (0.1)	93.9 (3.5)	4.0 (0.0)
		6	34.3 (0.6)	8.4 (0.6)	38.2 (0.7)	5.0 (0.1)	74.5 (6.6)	7.1 (0.2)	83.7 (3.0)	4.4 (0.0)
		8	32.2 (0.3)	9.2 (0.3)	36.2 (0.8)	5.6 (0.1)	68.2 (3.1)	8.1 (0.3)	79.6 (4.3)	4.9 (0.1)